Optical spectroscopy for tissue diagnostics and treatment control

Nazila Yavari

Doctoral Thesis

Department of Physics and Technology
University of Bergen

April 2006

University of Bergen, Norway

To My Beloved Parents

Contents

Abstract

Biomedical Optics as an interdisciplinary field of science has been developed during many years and is experiencing tremendous growth, to cover a wide range of optical techniques and methods, utilized for medical therapeutic and diagnostic purposes. Biomedical optics contributes by introducing methods and creation of devices used in healthcare of various specialties, such as ophthalmology, cardiology, surgery, dermatology, oncology, radiology, etc. Each of these specialities might take advantages of different optical techniques and methods such as: laser surgery, optical thermotherapy, optical tomography and imaging, optical biopsies, photodynamic therapy, *in vitro* diffuse spectroscopy, etc[1].

Among all of the mentioned methods and techniques; photodynamic therapy, medical applications of *in vitro* diffuse spectroscopy, and optical biopsies, are the main topics covered by the projects presented in this book.

This thesis is presented in two parts. Part one, consists of seven chapters as an introduction to the scientific works that are presented in five original papers in part two. Part one, covers areas that might not have been explicitly apparent in the papers, but have formed a basis needed to interpret data, and to understand the background for the various studied phenomena.

List of papers

Paper I Jan S. Dam, Nazila Yavari, Søren Sørensen, and Stefan Andersson-Engels,

Real-time absorption and scattering characterization of slab-shaped turbid samples obtained by a combination of angular and spatially resolved measurements, *Appl. Opt.* **44** (20): 4281- 4290 (2005).

Paper II N. Yavari, J. S. Dam, J. Antonsson, K. Wårdell, S. Andersson-Engels,

In vitro measurements of optical properties of porcine brain using a novel compact device, *Med. Biol. Eng. Comput.* **43** (5): 658-666 (2005).

Paper III Jenny Svensson, Ann Johansson, Nazila Yavari, Katarina Svanberg, Stefan Andersson-Engels,

Tissue temperature monitoring during interstitial photodynamic therapy, (Manuscript in preparation, 2005).

Paper IV N. Yavari, H.R. Mobini Far, N. Gustavsson, F. Torabi, C. Anderson, B. Danielsson, P.O. Larsson, K. Svanberg and S. Andersson-Engels

Measurements of ALA-Methylester diffusivity in normal skin *in vivo*: A pilot study, IFMBE Proc. **9**: 176-177 (2005).

Paper V Nazila Yavari, Jan Sørensen Dam, Johan Antonsson, Karin Wårdell, Stefan Andersson-Engels

Measurements of optical properties of pig brain tissue in vitro using a novel compact device, SPIE Proc. **5864**, 114-124 (2005).

The contributions from the author (Nazila Yavari) to the papers:

Paper I: I conducted all the experimental work, including the setting up the system; moreover, I was partly involved in the data evaluation and writing.

Paper II: I conducted all parts of the experimental work, data evaluation and analysis; and I wrote the manuscript.

Paper III: I contributed partly to the experimental work, and I contributed significantly to the writing of the manuscript.

Paper IV: I planned the study together with H.R.M.F. and S.A.E. I aslo contributed to the experimental work, and wrote the manuscript.

Paper V: I conducted all parts of the experimental work, data evaluation and analysis; and I wrote the manuscript.

Other related works and additional materials:

Poster: Dosimetry model for photodynamic therapy,
Nazila Yavari, Jenny Svensson, Katarina Svanberg, Stefan Andersson-Engels, International Graduate School Bio-Photonics '03, Ven, Sweden, 2003.

Poster: Experimental and theoretical verification of a compact device to measure optical properties from thin turbid samples,
Jan S. Dam, Nazila Yavari, Søren Sørensen, and Stefan Andersson-Engels, Optical Society of America (OSA) Topical Meeting on Biomedical Optics, Miami, Florida, 2004.

Poster: In vitro measurements of optical properties of porcine brain using a novel compact device,
Nazila Yavari, Jan Sørensen Dam, Johan Antonsson, Karin Wårdell, Stefan Andersson-Engels, National Annual Biomedical Engineering Meeting, Södertälje, Sweden, 2005.

Oral presentation: Measurements of optical properties of pig brain tissue in vitro using a novel compact device,
Nazila Yavari, Jan Sørensen Dam, Johan Antonsson, Karin Wårdell, Stefan Andersson-Engels, European Conference on Biomedical Optics (ECBO), Munich, Germany, 2005.

Oral presentation: Measurements of ALA-Methylester diffusivity in normal skin *in vivo*: A pilot study,
N. Yavari, H.R. Mobini Far, N. Gustavsson, F. Torabi, C. Anderson, B. Danielsson, P.O. Larsson, K. Svanberg and S. Andersson-Engels, 13th Nordic Baltic Conference in Biomedical Engineering and Medical Physics (NBC), Umeå, Sweden, 2005.

Oral presentation: Measurements of optical properties of pig brain tissue in vitro using a novel compact device,
N. Yavari, J. S. Dam, J. Antonsson, K. Wårdell, S. Andersson-Engels, Nordic Network for Women in Physics (NWIP), Bergen, Norway, 2005.

Abbreviations and symbols

Abbreviations

A-D	Adding-doubling
ALA	δ-aminolevulinic acid
CCD	Charge-coupled device
CASH	Combined angular and spatially-resolved head
CV	Coefficient of variation
DHB	Di-hydroxy benzoic acid
Hb	Deoxygenated haemoglobin
HbO_2	Oxygenated haemoglobin
HPLC	High performance liquid chromatography
IAD	Inverse adding-doubling
IC	Internal conversion
IPDT	Interstitial photodynamic therapy
IR	Infrared
IS	Integrating sphere
ISC	Intersystem crossing
LC	Liquid chromatography
LIF	Laser-induced fluorescence
MC	Monte Carlo
MPR	Multiple polynomial regression
MS	Mass spectroscopy
NAD^+	Oxidized nicotinamide adenine dinucleotide
NADH	The reduced form of NAD^+
NIR	Near infrared
PDT	Photodynamic therapy
PpIX	Protoporphyrin IX
RF	Radio frequency
UV	Ultraviolet

Symbols

E	Electric field	V/m
c	Speed of light	m/s
J	Electric current density	A/m^2
H	Magnetic field	A/m

$\mathbf{P}$	Electric polarization	As/m^2
σ	Conductivity	A/Vm
μ	Permeability	Vs/Am
χ	Electric susceptibility	-
r	Position vector	m
ε_r	Complex permittivity	As/Vm
ω	Angular frequency	rad/s
ε_0	In vacuo permittivity	As/Vm
n_c	Complex refractive index	-
$\mathbf{S}$	Poynting vector	W/m^2
I	Irradiance	W/m^2
μ_a	Absorption coefficient	m^{-1}
ε_x^λ	Molar extinction coefficient	m^2/mol
λ	Wavelength	nm
A	Area	m^2
V	Volume	m^3
q	Source function	W/m^3
C_s	Effective scattering cross- section	m^2
μ_s	Scattering coefficient	m^{-1}
μ_s'	Reduced scattering coefficient	m^{-1}
g	Anisotropy factor	-
μ_{eff}	Effective attenuation coefficient	m^{-1}
μ_t	Total attenuation coefficient	m^{-1}
P	Power	J/s(=W)
F	Radiant flux	W/m^2
N	Photon distribution function	$m^{-3}sr^{-1}$
L	Radiance	W/m^2sr
Φ	Fluence rate	W/m^2
δ	Penetration depth	m
D	Diffusion coefficient	m
R	Diffuse reflectance	W/m^2
T	Diffuse transmittance	W/m^2
ν	Frequency	s^{-1}
mfp	Mean free path length	m
I	Intensity	W/sr

Chapter 1

Introduction

And God said, "Let there be light,"
and there was light.

The Holy Bible

Let There Be Light! In the beginning, it was dark and cold. There was no sun, no light, no earth, and no solar system. There was nothing, just the empty void of space. Then slowly, about 4.5 billion years ago, a huge cloud of gas and dust was formed. Eventually this cloud contracted and grew into a central molten mass that became our Sun. At first the sun was a molten glow. As the core pressure increased, and the temperature rose to millions of degrees - a star was born. Through the process of thermonuclear hydrogen fusion, the sun began to shine. This is the nebular hypothesis, first proposed in 1755 by the great German philosopher, Immanuel Kant[2]. It is said that, about 4 billion years ago, soon after the Sun was formed, the Earth and the other planets in our solar system were formed from violent explosions and spin offs from the process that created the Sun[2]. Gradually oceans appeared and sunlight and water gave birth to life. Without light, there would be no life. Life was dependent on three things being present: a) the basic long molecule building block, carbon, b) water, and c) light. Eventually the oceans formed a rich organic soup that ultimately bore life. Somehow, as the primitive ocean organisms developed, one managed to develop a molecule that could use the energy of sunlight to produce food for itself. Sunlight, water, carbon dioxide, and simple inorganic elements were necessary and sufficient to develop and sustain an ecological system. The plant was born and the process

of photosynthesis had begun[2]. In this process, chlorophyll of the green plants absorbs the solar radiation, and by means of water and carbon dioxide, forms carbohydrates and oxygen, which both of them are basic requirements for animal life.

The effects of sun light on human body are also very interesting. In human body many photochemical and photobiological processes take place. The production of vitamin D, after absorption of ultraviolet (UV) radiation in the skin, is one of the important photochemical reactions[3]. A wide variety of physiological and metabolic processes in the body depend on the presence of vitamin D. Another effect of UV radiation on the skin, is simulating the production of the dark pigment in the skin, called melanin, which prevents the penetration of UV radiation into the deeper layers of the skin[4,5]. On the other hand, the harmful effects of UV radiation on biological systems should not be forgotten as well. When UV radiation is absorbed by DNA, some irreversible changes are introduced by photochemical reactions, causing mutations in the genetic code. Most often, the back-up systems developed through evolution manage to repair these changes; however, sometimes when the protective systems fail, the mutations lead to cancer[6]. There are processes that reduce and control the atmospheric transmission of UV radiation. These processes are based on Rayleigh scattering by air molecules, Mie scattering by clouds, and absorption by ozone; though, still significant amounts of UV radiation reach the Earth and influence life on it[7-9]. One of the most fascinating human reaction to light is the response of the photoreceptors in the eyes to the light, which enables visual perception[10].

The beneficial properties of light employed for medicinal purposes have a long tradition. "*Light therapy*", also called, *Phototherapy,* was known by the Egyptians, the Indians and the Chinese, and has been applied since 3000 years ago. During many years, many optical methods and devices have been introduced and developed to take best advantage of light properties employed in science and technology in general, and in medicine, in particular, for diagnostic and therapeutic purposes. The invention of the Laser was the turning point in this direction. The principle of the laser was first known in 1917, when Albert Einstein described the theory of stimulated emission. However, it was not until the late 1940s that utilizing this principle for practical purposes was begun. Laser was a remarkable technical breakthrough, but in its early years it was something of a technology without a purpose. Later on, powerful lasers were developed for use in surgery and other areas of science and technology, where a moderately powerful, pinpoint source of heat was needed[11].

Biomedical Optics as an interdisciplinary field of science has been developed during many years and is experiencing tremendous growth, to cover a wide range of optical techniques and methods, utilized for medical therapeutic and diagnostic purposes. Biomedical optics contributes in the introducing methods and creation of devices used in healthcare of various specialties, such as ophthalmology, cardiology, surgery, dermatology, oncology, radiology, etc. Each of these specialities might take advantages of different optical techniques and methods such as: laser surgery, optical thermotherapy, optical tomography and imaging, optical biopsies, photodynamic therapy (PDT), *in vitro* diffuse spectroscopy, etc[1].

Among all of the mentioned methods and techniques; PDT, medical applications of *in vitro* diffuse spectroscopy, and optical biopsies, are the main categories covering the projects and researches presented in this book.

PDT is a treatment modality based on photochemical reaction involving oxygen. It is a relatively new technique for local treatment, which is mostly applied to malignant tumors. PDT requires three simultaneously present components for cytotoxicity: a photosensitizer, light, and oxygen[12]. A photosensitive compound or pro-drug is administrated systemically or topically to the patient, and the photoactive agent utilized is most often selectively accumulated into the malignant tissue. The chemical reaction occurs just when the irradiation starts. The photosensitizer molecule is excited to its higher energy level by absorbing the energy of the illuminating light. The photosensitizer molecule releases then the excess energy once they are returning to the ground state. This excess energy is transferred to the oxygen molecules present, and produces singlet oxygen. Finally, the cytotoxicity of the produced singlet oxygen leads to the cell death. Many factors effect and control the optimization of the treatment and the efficacy of PDT. The diffusion coefficient or diffusivity of a pro-drug sensitizer (methyl-aminolevulenic acid), has been studied during topical application of the drug. This investigation is presented in Paper IV.

Besides being a non-invasive modality, the main advantages of PDT are the selectivity, the smooth and rapid healing and the ability of repeating the treatment on the same area, if necessary[13,14]. On the other hand, one of the main disadvantages of this technique is the limited light penetration. To overcome this limitation interstitial photodynamic therapy (IPDT) has been introduced and developed, which by use of optical fibers inserted in the tumor mass facilitates light transportation to any deep laying target tissue.

Another concept investigated in the work presented in this thesis, is the *in vitro* diffuse spectroscopy for biomedical applications. The investigated physical disorders are associated with physiological, biochemical and morphological changes of the tissue. All these alternations will affect the interaction processes between light and tissue from molecular to cell layer level[15]. Light interaction with and propagation through biological tissue are thus investigated. The light propagation in turbid biological media is governed by both its absorption and scattering properties. This type of spectroscopic measurements can provide information in many different scientific fields including for medicine. In medicine, the knowledge of tissue optical properties has found its application in cancer diagnostics and therapy. Tissue optical properties are mainly known as absorption coefficient (μ_a), scattering and reduced scattering coefficient (μ_s, μ_s'), and anisotropy factor (g). While absorption coefficient provides information on the concentration of various chromospheres, the scattering properties and anisotropy factor, provide important information about the form, size, and the concentration of different scattering components in tissue. Measurements of the optical properties of tissue can be performed *in vivo* or *in vitro*. Most *in vivo* measurements are based on frequency domain, time-resolved, or spatially resolved measurements. To extract the optical properties, an inverse algorithm usually based on the diffusion approximation and the fact that the tissue is relatively homogeneous within a relatively large probe volume, is utilized.

The most common technique for extracting the optical properties of tissue *in vitro* is the Integrating Sphere (IS) method. This technique requires, however, bulky instrumentation, inconvenient sample handling and complicated measurements techniques. In Paper I, the principles of a fast and accurate algorithm, in combination with a new compact device developed for determining tissue optical properties, *in vitro*, are described. In Paper II, the optical properties of porcine brain tissue has been measured using this new

instrumentation and the results are compared with the measured results obtained from an integrating sphere system. Both systems were calibrated with a set of tissue phantoms with known optical properties. Paper V, is generally introducing the same work presented in Paper II, while a different calibration method is employed.

The other concept to discuss is "Optical biopsy", which by using the corresponding modification of the optical signals from light-tissue interaction, forms spectra fingerprints for tissue characterization. The spectral distribution in all optical diagnostic techniques, depend on the illumination and collection light geometry. Depending on the type of light interaction/emission with/from tissue and the absorbing molecules, four main categories of diagnostic techniques are identified: 1- Laser-induced fluorescence (LIF), 2- Raman spectroscopy, 3- Laser-Doppler flowmetry, and 4- Elastic scattering spectroscopy. In all of these techniques, the outcome results are based on the optical properties of the tissue and the induced wavelength of the applied light. In ideal situation for detecting geometry the total distribution of the scattered light is collected, which can be done by utilizing integrating sphere method. The problem is that this technique is not clinically practical. Instead, a geometry based on optical fibers is suggested.

Combining LIF and PDT, provide an important tool for diagnostic and therapeutic purposes. In Paper III, LIF is used in connection with IPDT to investigate any temperature changes during (maybe caused by) the treatment. Temperature is an important factor that can affect the result in PDT and IPDT. Due to the fact that the fluence rate is very high at the fiber tip for IPDT with bare end fibers, it would be interesting to investigate the local temperature change during such treatment. In this study, the temperature was measured during PDT/IPDT using fibers having a small crystal with temperature dependent fluorescence. The influence of the fiber geometry and different scattering properties of the tissue were investigated.

In a study not presented in this thesis, the optical properties of human brain tissue (normal and lesion tissue) have been measured using an integrating sphere system. These measurements were performed in order to compare the results obtained using IS and Optical Coherence Tomography (OCT) techniques. OCT is a very important optical technique in superficial tissue tomography[16]. Specific advantages of OCT compared to other tomography techniques are its high depth resolution, relatively high probing depth in scattering media, contact-free and non-invasive operation, and the possibility to create various function dependent image contrast methods[17].

Chapter 2

Interaction of light with tissue

Light is Love revealed.
Light is Life manifested.
Light is God fulfilled.

Sri Chinmoy

2.1 Introduction

Life in any form is surrounded by light. Interacting with matter, light participates in so many different processes. Interaction of light with matter can reveal important information about the nature of the matter. The electromagnetic spectrum, shown in Figure 2.1, ranges from radio wave to gamma radiation; while the term "light" generally refers to that portion of the spectrum with wavelength between 400 nm and 700 nm, which can be seen by naked eye. Electromagnetic radiation in general and light in particular, has a dual nature as both particles and waves.

Considering the duality nature of light, the concept of light-tissue interaction is to be discussed. Because of its dualistic nature and also depending on the type of the experiment, we can look at it in two ways. One is as changing electric and magnetic fields, which propagate through space, forming an electromagnetic wave. This wave has

amplitude, which is the brightness of the light, wavelength, which is the color of the light, and an angle at which it is vibrating, called polarization**.** This was the classical interpretation, crystallized in Maxwell Equations, which held sway until Planck, Einstein and others came along with quantum theory. In terms of the modern quantum theory, electromagnetic radiation consists of particles called photons, which are packets-quanta, of energy, which move at the speed of light. In this particle view of light, the brightness of the light is the number of photons, and the color of the light is the energy contained in each photon.

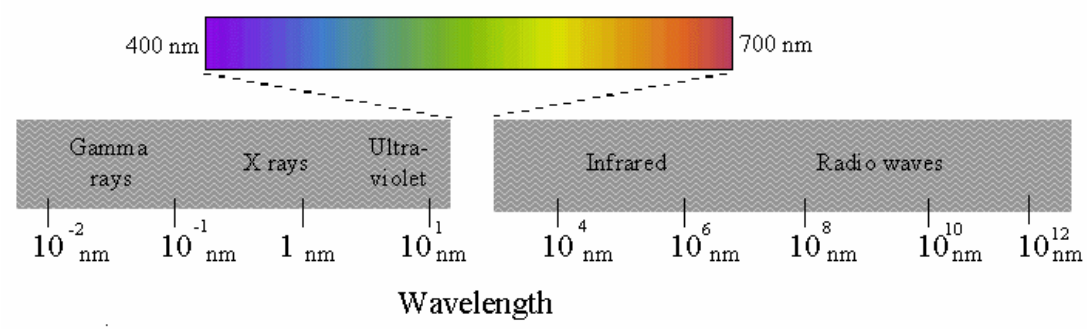

Figure 2.1 *Electromagnetic radiation spectrum***.**

To describe the wave nature of the electromagnetic radiation, the terms wavelength λ, or frequency ν are used; while in the particle description of the electromagnetic radiation, the energy E, is used. These quantities are connected as

$$E(J) = h.\nu = h.\frac{c}{\lambda} = E(eV).q_e \qquad (2.1)$$

where h denotes Planck's constant, c the speed of light, and q_e the electron unit charge. E(J) and E(eV) are energy in joules and energy in electron-volts; respectively.

Interacting different parts of the electromagnetic spectrum with matter have different effects on it. For example, the human body is quite transparent to the low frequency radio waves, while moving to microwaves and infrared to visible light, the body absorbs more and more. In the lower ultraviolet range, all the UV radiation from the sun is absorbed in the thin outer layer of skin, while moving towards the X-ray region of the electromagnetic spectrum, the body becomes transparent again.

2.2 Properties of light

Both the wave and particle descriptions of light appear in tissue optics. When light is passing through a tissue with regular structure such as flowing blood, as disc-shaped cells, a characteristic asymmetry can be found in the angular distribution of the scattered light, a phenomenon can be taken into account using the wave propagation properties of light. While in the studies of thick and dense tissues, such as breast tissue, the wave

characteristics of light are ignored as the properties associated with the wave nature of light are lost. Instead, considering the particle nature of light, a model based on the light propagation as a stream of energy quanta, takes place[15].

2.2.1 Electromagnetic wave theory

Electromagnetic waves are waves of electric and magnetic forces, where a wave motion is defined as propagation of disturbances in a physical system. A change in the electric field is accompanied by a change in the magnetic field, and vice versa. These phenomena were described in 1865 by James Clerk Maxwell in four equations, which have come to be known as the Maxwell Equations. From the classical point of view, light as any electromagnetic waves, satisfies the Maxwell equations. These equations for macroscopic electromagnetic case at interior points in matter, may in SI units be written as[18,18,19]

$$\nabla.\mathbf{D} = \rho_F \tag{2.2}$$

$$\nabla \times \mathbf{E} + \frac{\partial \mathbf{B}}{\partial t} = 0 \tag{2.3}$$

$$\nabla.\mathbf{B} = 0 \tag{2.4}$$

$$\nabla \times \mathbf{H} = \mathbf{J}_f + \frac{\partial \mathbf{D}}{\partial t} \tag{2.5}$$

where **E** is the electric field, **B** the magnetic induction, **J** the current density, and ρ the volume charge density. **D** and **H** are defined by

$$\mathbf{D} = \varepsilon_0 \mathbf{E} + \mathbf{P} \tag{2.6}$$

$$\mathbf{H} = \frac{\mathbf{B}}{\mu_0} - \mathrm{M} \tag{2.7}$$

where **D** is the displacement, **H** the magnetic field, **P** the electric polarization, and M the magnetization. The permittivity and the permeability of the free space are represented by ε_0 and μ_0, respectively. All the Eqs. (2.2) to (2.7) must be supplemented with the following constitutive relations

$$\mathbf{J} = \sigma \mathbf{E} \tag{2.8}$$

$$\mathbf{B} = \mu \mathbf{H} \tag{2.9}$$

$$\mathbf{P} = \varepsilon_0 \chi \mathbf{E} \tag{2.10}$$

where σ is the conductivity, μ the permeability, and χ the electric susceptibility. These coefficients depend on the characteristics of the medium under consideration. Regard to

the electromagnetic terms which a bulk non-scattering medium may be approximated by a homogeneous and isotropic continuum of free charges and small dipoles[20]; these coefficients will be assumed to be independent of position (the medium is homogeneous), and independent of directions (the medium is isotropic).

In the time harmonic case, the Maxwell equations may be written in complex form as[18]

$$\nabla.(\varepsilon_r\varepsilon_0\mathbf{E}(r,\omega)) = 0 \tag{2.11}$$

$$\nabla\times\mathbf{E}(r,\omega) = i\omega\mu_0\mathbf{H}(r,\omega) \tag{2.12}$$

$$\nabla.\mathbf{H}(r,\omega) = 0 \tag{2.13}$$

$$\nabla\times\mathbf{H}(r,\omega) = -i\omega\varepsilon_r\varepsilon_0\mathbf{E}(r,\omega) \tag{2.14}$$

where r is the position vector, ε_r the complex permittivity, and ω the angular frequency of the harmonic fields. Considering the *constitutive relations* in Eq. (2.8) to (2.10), the complex permittivity is given by

$$\varepsilon_r = \varepsilon_0(1+\chi(\omega)) + i\frac{\sigma}{\omega} \tag{2.15}$$

2.2.2 Plane wave propagation

Maxwell equations show that propagation of electromagnetic waves must satisfy the following wave equations

$$\nabla^2\mathbf{E}(r,\omega) + \frac{\omega^2 n_c^2}{c_0^2}\mathbf{E}(r,\omega) = 0 \tag{2.16}$$

$$\nabla^2\mathbf{H}(r,\omega) + \frac{\omega^2 n_c^2}{c_0^2}\mathbf{H}(r,\omega) = 0 \tag{2.17}$$

where c_0 is the speed of light *in vacuo*, and n_c the complex refractive index that is defined by

$$n_c = n + i\kappa = \sqrt{\varepsilon_r} \tag{2.18}$$

The solutions to the Eq. (2.16) and (2.17) yield the plane-wave equations as

$$\mathbf{E} = \mathbf{E_0}\exp(i\mathbf{k}\cdot x - i\omega t) \tag{2.19}$$

$$\mathbf{H} = \mathbf{H_0}\exp(i\mathbf{k}\cdot x - i\omega t) \tag{2.20}$$

where $\mathbf{E_0}$ and $\mathbf{H_0}$ are constant vectors, and $\mathbf{k}$ is the wave vector indicating the direction of propagation. The wave vector may be complex[20]

$$\mathbf{k} = \mathbf{k}' + i\mathbf{k}'' \tag{2.21}$$

where k' and k" are real vectors. If Eq. (2.21) is substituted in Eqs. (2.19) and (2.20), we obtain

$$\mathbf{E} = \mathbf{E_0} \exp(-\mathbf{k}''\cdot x)\exp(i\mathbf{k}'\cdot x - i\omega t) \tag{2.22}$$

$$\mathbf{H} = \mathbf{H_0} \exp(-\mathbf{k}''\cdot x)\exp(i\mathbf{k}'\cdot x - i\omega t) \tag{2.23}$$

$\mathbf{E_0}\exp(-\mathbf{k}''\cdot x)$ and $\mathbf{H_0}\exp(-\mathbf{k}''\cdot x)$ are the amplitudes of the electric and magnetic waves, and $(i\mathbf{k}'\cdot x - i\omega t)$ is the phase of the waves. If $\mathbf{k}'$ and $\mathbf{k}''$ are parallel, the waves are said to be homogeneous; if $\mathbf{k}'$ and $\mathbf{k}''$ are not parallel, the waves are said to be inhomogeneous (such as waves propagating in vacuum). It should be mentioned that plane waves are physically unrealizable because they are infinite in time and space; and only certain electromagnetic waves that satisfy the Maxwell equations are physically realizable.

2.2.3 The Poynting vector

Considering an electromagnetic field ($\mathbf{E}$, $\mathbf{H}$); the magnitude and direction of the rate of transfer of electromagnetic energy at all points of space, is quantified by the Poynting vector as the following,

$$\mathbf{S} = \mathbf{E}\times\mathbf{H} \tag{2.24}$$

The Poynting vector is very important in propagation, absorption and scattering problems of electromagnetic waves. For time-harmonic fields, $\mathbf{S}$ is a rapidly varying function of frequency. Regard to the rapid oscillations of the Poynting vector, it is more convenient to apply the time-averaged Poynting vector for time-harmonic fields,

$$\langle \mathbf{S} \rangle = \frac{1}{2}\mathrm{Re}\{\mathbf{E}\times\mathbf{H}^*\} \tag{2.25}$$

The time-averaged Poynting vector for a plane harmonic wave is given by

$$\langle \mathbf{S} \rangle = \frac{1}{2} n c_0 \varepsilon_0 |\mathbf{E_0}|^2 e^{-\frac{4\pi\kappa z}{\lambda_0}} e_z \tag{2.26}$$

The magnitude of the time-averaged Poynting vector, which is denoted by the symbol I or E, is called *irradiance*,

$$I = \left|\langle \mathbf{S} \rangle\right| \tag{2.27}$$

The dimension of *irradiance* is energy per unit area and time; and so often, the term *intensity* is used to denote *irradiance.*

From Eq. (2.26) it is not only seen that *irradiance* is in the direction of propagation, i.e. e_z; and therefore parallel to k; but also it appears that as the wave transverses the medium, the *irradiance* is also exponentially attenuated as a function of distance in the propagation direction.

2.3 Absorption

By considering the definition of *irradiance* and Eq. (2.26), the following equation, known as Beer's law, is obtained.

$$I = I_0 e^{-\mu_a z} \tag{2.28}$$

where I_0 is the irradiance at $z = 0$, and μ_a (m^{-1}) is the absorption coefficient.

$$\mu_a = \frac{4\pi\kappa}{\lambda_0} \tag{2.29}$$

Therefore, the rate at which electromagnetic energy is removed from the wave as it propagates through the medium, and/or in other word, the absorption coefficient μ_a at a given wavelength λ; is determined by the imaginary part κ of the complex refractive index n_c. This definition is based on the macroscopic electromagnetic term with a continuum medium assumption.

The absorption coefficient (μ_a) is the probability per unit distance for an absorption event to occur. In many chemical applications with homogeneous and non-scattering samples, the Beer-Lamberts law, Eq. (2.28), can be used for measuring the absorption coefficient. In turbid media, such as biological tissues, the Beer-Lambert law cannot, however, be utilized directly, as the path length of the light is not known. Figure 2.2 shows how the intensity of light directed onto a cuvette decreases exponentially through an absorbing medium according to the Beer-Lambert law.

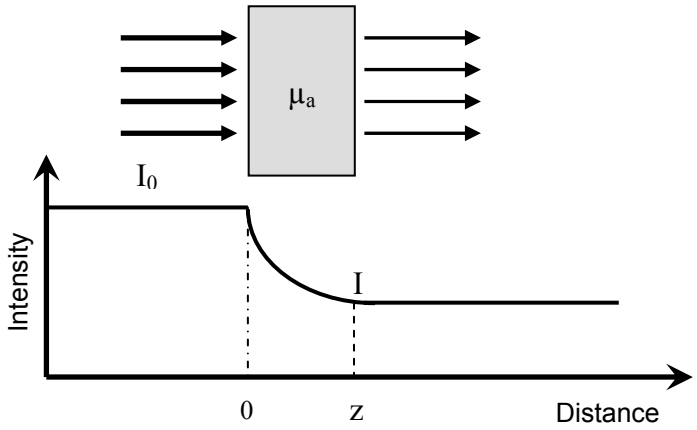

Figure 2.2 *Light absorption in a cuvette with a homogeneous absorbing medium according to the Beer-Lambert law, modified from Ref*[21].

2.3.1 Quantum theory

From the microscopic point of view and according to the quantum theory, the energy levels in atoms and molecules are quantized. If the energy of the incident photon (hν) matches the gap between to energy levels in the molecule, it can be absorbed by the molecule, otherwise the molecule will be transparent to that radiation, and it will pass through. When photon is absorbed by the molecule, the transitions between the specific energy levels can be divided into high energy electronic transitions (UV and VIS regions) and low energy vibrational or rotational transitions (NIR and IR regions)[22,23]. As it is shown in Jablonski diagram, Figure 2.3, after the absorption of a photon and the subsequent excitation to the higher energy level (S_0 --> S_n), the molecule relaxes down to the lowest excited energy level; then relaxation from the lowest excited state to the ground state may happen through different processes. If the spin state of the initial and the final energy levels be the same (S_1 --> S_0), the relaxation is called fluorescence.

If the spin state of the initial and the final energy levels are different (T_1 --> S_0), the relaxation is called phosphorescence. Fluorescence and phosphorescence are radiative processes. Transitions between the same spin states are called internal conversion (IC), while such transitions between different spin states are called intersystem crossing (ISC).

Usually the stable ground state in most molecules is the singlet state (S_0 in Figure 2.3), while the triplet states ($T_{1,\,2}$ in Figure 2.3) are unstable excited states with an increased internal energy. Oxygen is one of the rare molecules for which the lowest triplet state is the ground state. Excited molecular oxygen is in the singlet state. This is important in the photodynamical reaction occurring during photodynamic therapy (PDT)[24], (see Chapter 7). There is another type of photon-electron transition called stimulated emission, which happens in atoms.

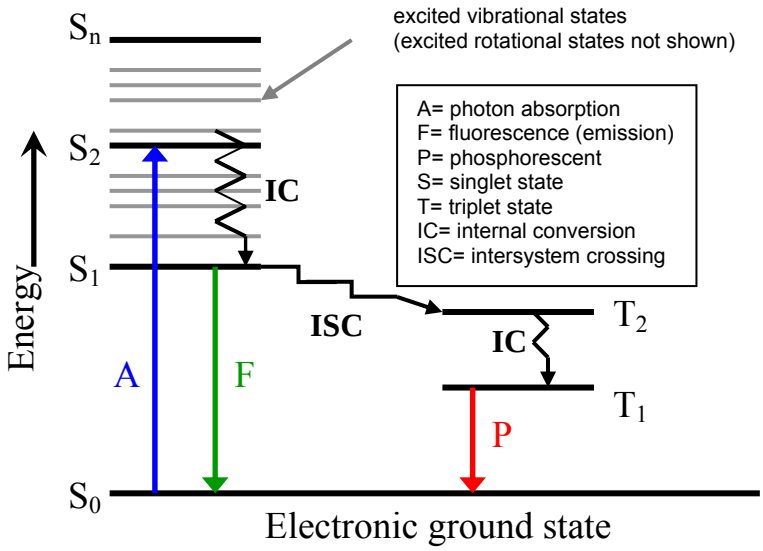

Figure 2.3 *Jablonski diagram. Energy levels and the possible pathways following light absorption by an absorbing molecule (chromophore). Modified from Ref.*[22,25].

When an atom or molecule already is in an excited state, then an incoming photon with quantum energy equal to the excess internal energy of that atom or molecule, can produce a second photon of the same energy by stimulating the atom or molecule to fall down to its lower energy state, shown in Figure 2.4. This is the principle of the light amplification happens in lasers (**L**ight **A**mplification by **S**timulated **E**mission of **R**adiation). Photons produced by stimulated emission have the same phase and frequency, resulting in very intense and coherent light (laser).

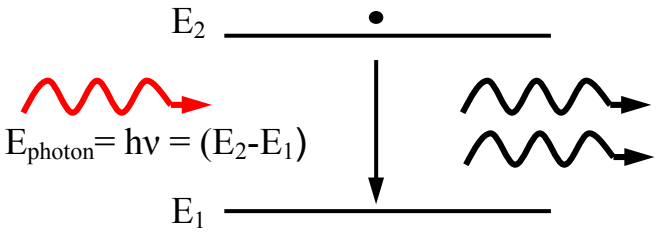

Figure 2.4 *Stimulated emission. The electron in the excited state falls into the lower state emitting a photon.*

2.3.2 Tissue absorption

Inside tissue, light can be absorbed by tissue absorbers, called chromophores. The probability of absorption is described by the absorption coefficient, μ_a, which is defined as the probability of absorption per unit length. The absorption coefficient equals the sum of all the contributions to absorption by chromophores in the tissue [26], as the following

$$\mu_a^{\lambda} = \ln(10) \cdot \varepsilon_x^{\lambda} \cdot C_x \qquad (2.30)$$

where ε_x^{λ} is the molar extinction coefficient, and C_x is the absorber concentration of the chromophore. The product of $\varepsilon_x^{\lambda} \cdot C_x$ is in units of cm^{-1}. From Eq. (2.30) it is seen that absorption coefficient is wavelength depended as a result of different chromophores have different absorption spectra. Figure 2.5, shows the absorption spectra of some important chromophores in human skin tissue.

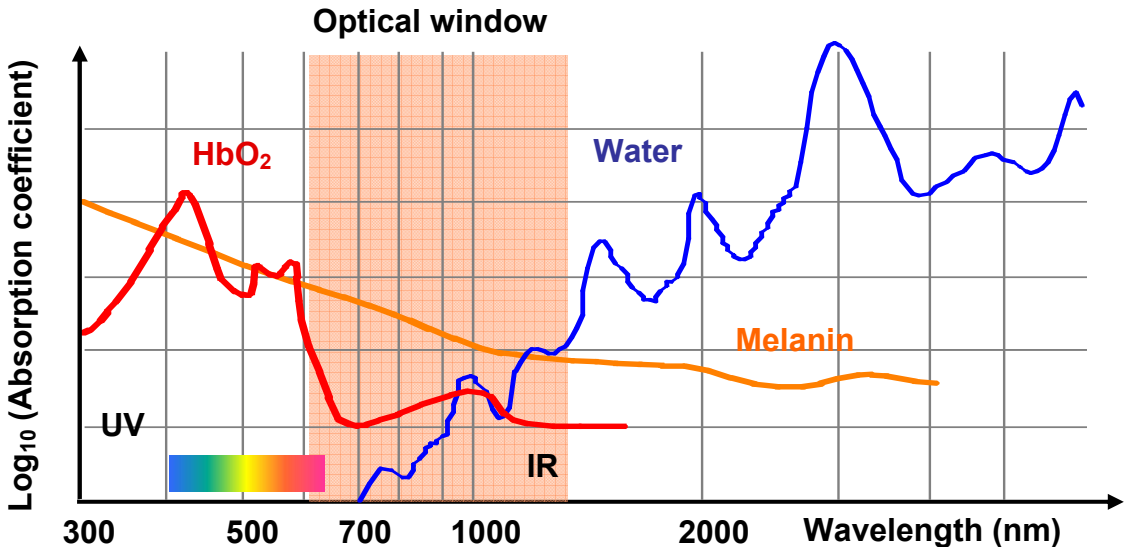

Figure 2.5 *Absorption spectra of some important chromophores in human skin tissue, as function of wavelength. Adapted from Ref*[27].

Constituting 75 % of the tissue, water is the most important absorber in tissue, dominating in the UV ($\lambda < 200$ nm), and IR ($\lambda > 1300$ nm) region[28]. Other important chromophores in tissue are haemoglobin and melanin. The absorption of light by blood depends on the oxygenated (HbO_2) and deoxygenated (Hb) haemoglobin. The absorption spectra shows one sharp peak at about 430 nm for HbO_2, while dropping off until 530 nm, the spectra picks up at 540 nm and 576 nm, and finally its lowest absorption takes place for wavelengths above 600 nm (Figure 2.5). Melanin is a pigment in hair, skin and eye. Protecting the organism from UV radiation is the main function of melanin in the skin. Melanin absorption decreases with increasing wavelength.

The low-absorbing region between approximately 630 nm and 1300 nm is referred to as the tissue optical window. In this range, the penetration of light into biological tissue is at its deepest.

2.4 Refraction, Reflection[29]

Light incident on a surface of tissue, will be partially reflected and partially transmitted as a refracted ray. Due to interaction of light with the medium, the effective speed of light is reduced. This reduction is determined by the real part of the refraction index of the medium, Eq. (2.18). The real part of the index of refraction is defined as the ratio between the speed of light in vacuum and the speed of light in the medium.

$$n = \frac{c}{v} \tag{2.31}$$

The angle relationships for both reflected and refracted light can be derived according to Fermat's principle. Fermat's principle says that light follows the path of least time. Considering Figure 2.6, the following shows how the law of reflection can be derived from the Fermat's principle. The path length L, along the light ray from A to B is

$$L = \sqrt{a^2 + x^2} + \sqrt{b^2 + (d - x)^2} \tag{2.32}$$

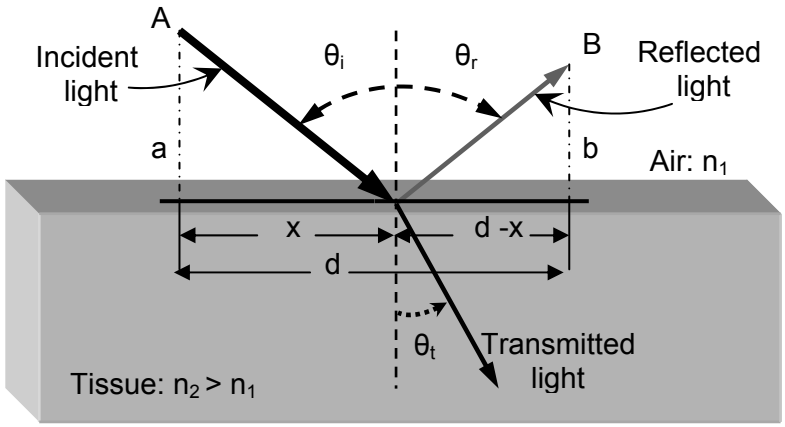

Figure 2.6 *Light incidents to the surface of a medium will partially be reflected and partially be transmitted (refracted).*

As the speed of light is constant, we can obtain the point of reflection yielding the minimum path distance by setting the derivative of L with respect to x equal to zero ($\frac{dL}{dx} = 0$).

$$\frac{x}{\sqrt{a^2 + x^2}} = \frac{(d - x)}{\sqrt{b^2 + (d - x)^2}} \tag{2.33}$$

which results in

$$\sin\theta_i = \sin\theta_r \quad \text{yielding} \quad \theta_i = \theta_r \tag{2.34}$$

The above results show the law of reflection. According to the law of reflection, a light ray incident upon a reflective surface, will be reflected at an angle equal to the incident angle with respect to the normal to the surface. As mentioned in the beginning of this section, the index of refraction is defined as the speed of light in vacuum divided by the speed of light in the medium, Eq. (2.31); so the index of refraction for different media can be measured. Snell's law relates the indices of refraction of the two media to the directions of propagation in terms of the angles to the normal.

Considering Figure 2.7, it is seen that Snell's law can also be derived from Fermat's principle, by setting the derivative of time equal to zero ($n_1 < n_2$).

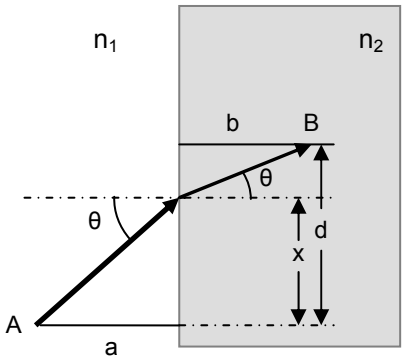

Figure 2.7 *Light traveling from one medium (n_1)* into another one (n_2) with $n_1 < n_2$; bends toward the normal on the surface leading to Snell's law.

$$t = \frac{\sqrt{a^2 + x^2}}{v_1} + \frac{\sqrt{b^2 + (d-x)^2}}{v_2} \tag{2.35}$$

$$\frac{dt}{dx} = \frac{x}{v_1\sqrt{a^2 + x^2}} - \frac{(d-x)}{v_2\sqrt{b^2 + (d-x)^2}} \tag{2.36}$$

$$0 = \frac{\sin\theta_1}{v_1} - \frac{\sin\theta_2}{v_2} \tag{2.37}$$

Considering the index of refraction defined as $n = \frac{c}{v}$, Snell's law is concluded from the last formula (2.37) as

$$\frac{n_1}{n_2} = \frac{\sin\theta_2}{\sin\theta_1} \tag{2.38}$$

In case of unpolarized light, Figure 2.6, the specular reflectance R, which is the fraction of the reflected intensity, is given by Fresnel's formula[20],

$$R = \frac{1}{2}\left(\frac{\tan^2(\theta_i - \theta_t)}{\tan^2(\theta_i + \theta_t)} + \frac{\sin^2(\theta_i - \theta_t)}{\sin^2(\theta_i + \theta_t)} \right) \tag{2.39}$$

For the light reflected in a surface between two media with different index of refraction, $n_1 < n_2$, Snell's law yields that there is a critical angle. Beyond the critical angle, no light will be refracted, but 100 % will be reflected. The critical angle for internal reflection for light propagation inside tissue, is given by

$$\theta_c = \arcsin\left(\frac{n_1}{n_2} \right) \approx 46^\circ \tag{2.40}$$

Most biological tissues have an average refractive index ranging 1.38-1.41[30,31], except for fatty tissues where the refractive index is about 1.46.

In tissue optics, turbid biological media is considered as a collection of discrete randomly distributed scattering particles (Figure 2.8). As the index of refraction of these discrete elements, n_s, is different from that of the surrounding medium, n_m; the relative refractive index is introduced as the following,

$$m = \frac{n_s}{n_m} \neq 1 \tag{2.41}$$

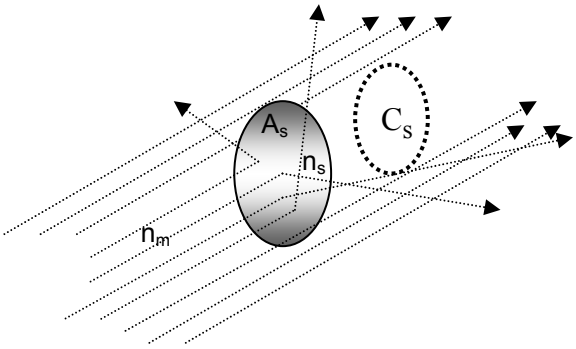

Figure 2.8 *Scattering by a discrete particle. Adapted from Ref[1]*

2.5 Scattering

Light passing through tissue can be attenuated by absorption and by scattering. Only part of the light that is transported into the biological tissue will be transmitted. Light attenuation in tissue depends on wavelength of the incident light, and the tissue

characteristics. Tissue absorption was discussed earlier (see section 2.3.2). Here, the scattering will be discussed. There are two major types of scattering event. If the frequency of the scattered wave is equal to that of the incident wave, it is called *elastic scattering*, but if the frequency of the incident wave and the scattered wave differs, it is called *inelastic scattering*. Rayleigh and Mie scattering are two types of elastic scattering. Rayleigh scattering happens when the size of the scatterers (molecules and very tiny particles) are much smaller than the wavelength of the incident wave (up to about a tenth of the wavelength). Mie scattering predominates when the size of the scatterers are larger than the wavelength of the incident light. In Mie scattering the intensity of the scattered light increases with shorter wavelength, approximately proportional to λ^{-2}; while in Rayleigh scattering, it is proportional to λ^{-4}. It is helpful to consider the molecular structure to understand the inelastic scattering event. A molecule is formed by the binding of two or more atoms in such a way that the total energy is lower than the sum of the energies of the constituents. The description of molecular structure is considerably more complicated than that of isolated atoms[32] since, apart from energy levels corresponding to different electronic arrangements, there are also different states corresponding to vibrational and rotational[22]. The allowed internal energy for molecular structures of diatomic molecules is schematically shown in Figure 2.9.

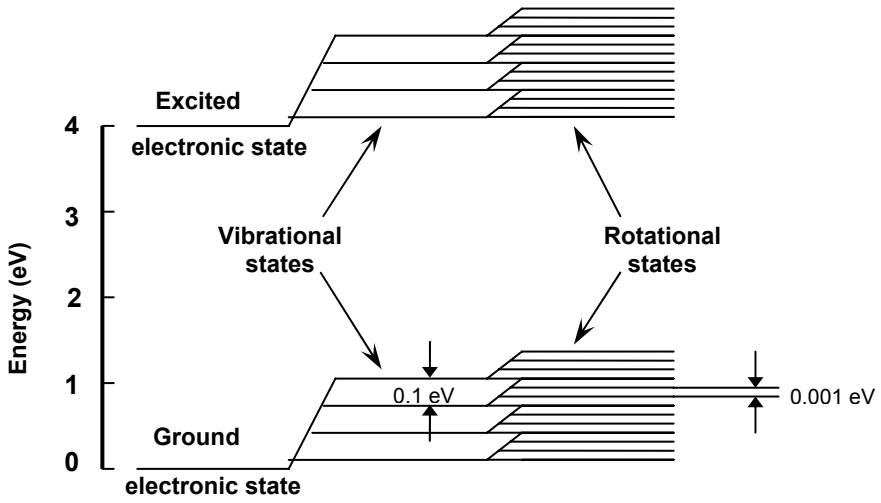

Figure 2.9 *Schematic molecular energy level for diatomic molecules, modified from Ref.*[22].

Inelastic scattering happens when the incident light interacts with vibrational and rotational levels of molecules causing transition between these levels, and altering the wavelength (energy) of the scattered light comparing to the incoming light, see Figure 2.10. The Raman effect represents inelastic scattering. If the energy of the incident light is not corresponding to the energy separation between two electronic levels, still weak scattering effects, Rayleigh and Raman scattering, are obtained. As illustrated in Figure 2.10, depending on the initial and final states, energy of photon is preserved (Rayleigh

scattering), increased (Raman Anti-Stokes) decreased (Raman Stokes)[33]. In quantum mechanical theory, virtual levels are introduced, which mediate the scattering[22].

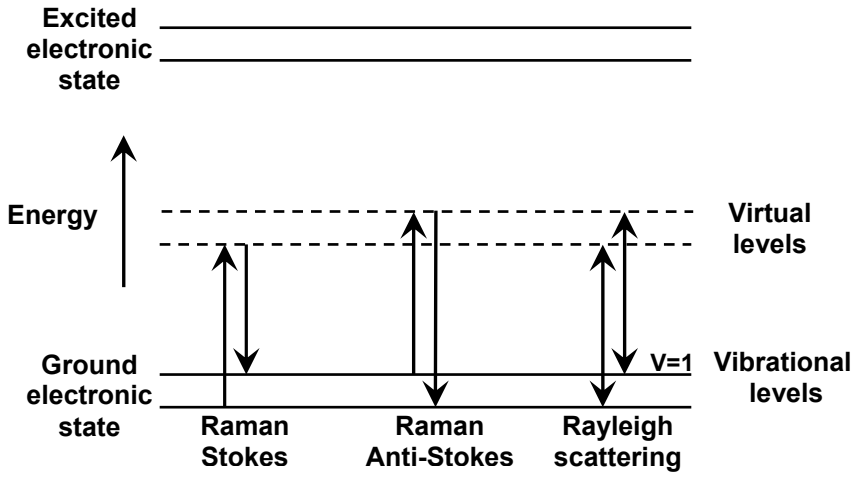

Figure 2.10 *Raman and Rayleigh scattering. Modified from Ref[33].*

Scattering in tissue is due to several optical effects[34]; a) reflection and refraction of light from interfaces between materials having different refractive indices, b) reflection of light by discrete particles in the tissue ranging from organic molecules to whole cells, c) absorption of light rays by atoms and molecules and re-radiation at the same wavelength but in other directions[24]. In all these processes just the direction of light changes due to the scattering, and no energy loss is involved, so they are under the label elastic scattering.

Scattering in turbid media is described by the scattering coefficient, μ_s, which is defined as the probability of scattering per unit length; and describes the average of how many times per unit length a photon change its direction. In tissue, scattering is not isotropic, but forward directed[35,36].

2.5.1 Scattering cross- section, coefficient, and mean free path length

Considering Figure 2.8, the effective scattering cross- section, C_s is defined as

$$C_s = \delta_S A_s \tag{2.42}$$

where A_s is the scattering element through the scattering efficiency δ_S. Hence, the scattering coefficient is concluded as

$$\mu_s = C_s \rho_s \tag{2.43}$$

where ρ_s is the volume density of the scattering elements. The average distance a photon travels between scattering events, is called the mean free path length, and is defined as

$$mfp_s = \frac{1}{\mu_s} \tag{2.44}$$

2.5.2 Scattering phase function and anisotropy factor

In biological tissue the scattering of light is not isotropic, but has been shown to be strongly forward directed[35,36]. Also, neither Rayleigh nor Mie scattering completely describe scattering in tissue. Therefore, it is very convenient to define a probability function p(θ) of a photon to be scattered by an angle θ, which can be fitted to experimental data[37]. By furthermore assuming that tissue is isotropic in terms of physical properties (such as refractive index, density, etc.)[38], scattering depends only on the angle θ between unit vector directions ŝ and ŝ' (Figure 2.11). The angular dependence of scattering, called the probability distribution function and/or the scattering phase function, is a function of the scattering angle such that p(ŝ, ŝ') = p(θ).

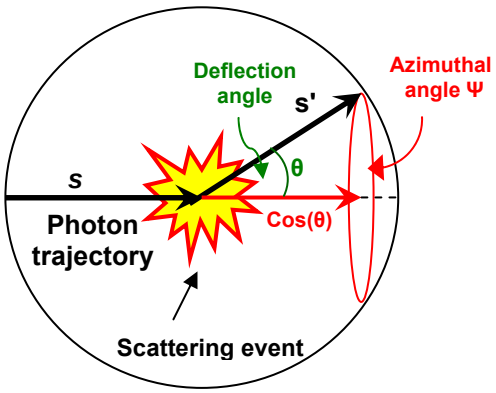

Figure 2.11 *A scattering event causes a deflection at angle θ from the original direction* ŝ *to the direction* ŝ'. *Adapted from Ref*[39].

For light transport in biological tissue the Henyey-Greenstein function is usually applied as the following[39,40],

$$p(\theta) = \frac{1}{4\pi} \frac{1-g^2}{\left(1+g^2-2g\cos\theta\right)^{3/2}} \tag{2.45}$$

such that

$$\int_0^{\pi} p(\theta) 2\pi \sin\theta d\theta = 1 \quad \text{, and} \quad \int_0^{\pi} \cos\theta p(\theta) 2\pi \sin\theta d\theta = g \tag{2.46}$$

It is also common practice to express the Henyey-Greenstein function as the function of $p(\cos\theta)$;

$$p(\cos\theta) = \frac{1}{2} \frac{1-g^2}{(1+g^2-2g\cos\theta)^{3/2}} \tag{2.47}$$

such that

$$\int_{-1}^{1} p(\cos\theta) d(\cos\theta) = 1 \quad \text{, and} \quad \int_{-1}^{1} \cos\theta p(\cos\theta) d(\cos\theta) = g \tag{2.48}$$

where "g", called anisotropy factor, is the mean cosine of scattering angle θ ($g = \langle \cos\theta \rangle$), which measures the degree of anisotropy in scattering. Figure 2.12, shows a series of Henyey-Greenstein functions corresponding to different g- values.

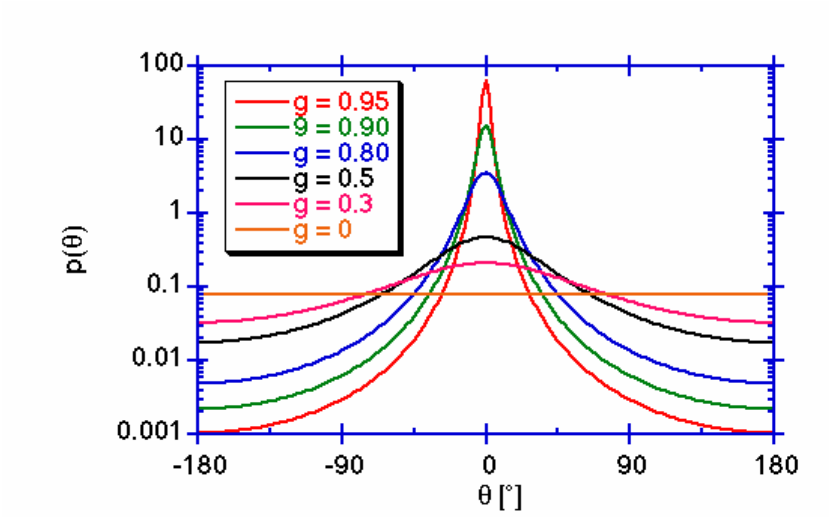

Figure 2.12 *A series of plots of the Henyey-Greenstein functions for different g-values. Adapted from Ref*[40].

The g-factor ranges between -1 (for totally back scattering), and 1 (for totally forward scattering); while $g = 0$ corresponds to isotropic scattering. For most biological tissues the value of "g" varies between 0.8 and 0.95[41]. For *in vitro* tissues in the visible and near-infrared wavelength regions, "g" has been measured to be between 0.7 and 0.99[38].

2.5.3 Mie scattering

Very often, the scattering medium behaves like a collection of discrete spherical particles. In this case the Mie scattering, which in its pure form, deals with spherical particles will dominate[21].

The Mie-scattering theory also called Lorenz-Mie, was developed by Gustav Mie in 1908. The theory is named after German physicist Gustav Mie (1868-1957) and Danish physicist Ludvig Lorenz (1829-1891), who independently developed the theory of electromagnetic plane wave scattering by a dielectric sphere. Mie-scattering theory provides rigorous solutions on the basis of electromagnetic theory for light scattering by an isotropic sphere embedded in a homogeneous medium[19,42]. According to Mie theory, the scattering properties of non-absorbing homogeneous particle is described in terms of two parameters; the magnitude of refractive index mismatch Eq.(2.41), and the size of the surface of refractive index mismatch[39] as the following,

$$x = 2\pi a/(\lambda/n_m) \tag{2.49}$$

which is a dimensionless constant.

In general, when the particle diameter is similar to the light wavelength, light interacts with the particle over an effective cross-sectional area larger than the geometrical cross section of the particle. The Mie calculation output provides this scattering cross section, C_S. Often this parameter is divided by the geometrical cross-sectional area to give a dimensionless scattering efficiency parameter; δ_S (Figure 2.8).

$$\delta_S = C_S/A_S \tag{2.50}$$

where δ_S, is the efficiency of scattering, and $A_S = \pi a^2$ is the true geometrical cross-sectional area of the particle. The scattering coefficient can be related to the scattering number density, ρ_S, and the cross-sectional area of scattering as,

$$\mu_S\ (cm^{-1}) = \rho_S\ (cm^{-3})\ C_S\ (cm^2) \tag{2.51}$$

From the mathematical point of view, Mie scattering can be described briefly by considering a source, a spherical scattering particle, and an observer whose three positions define a plane called the scattering plane. The incident and the scattered light can be reduced to their components which are parallel or perpendicular to the scattering plane[39], see Figure 2.13. As it is seen from the figure, the parallel and perpendicular components can be experimentally selected by a linear polarization filter oriented parallel or perpendicular to the scattering plane.

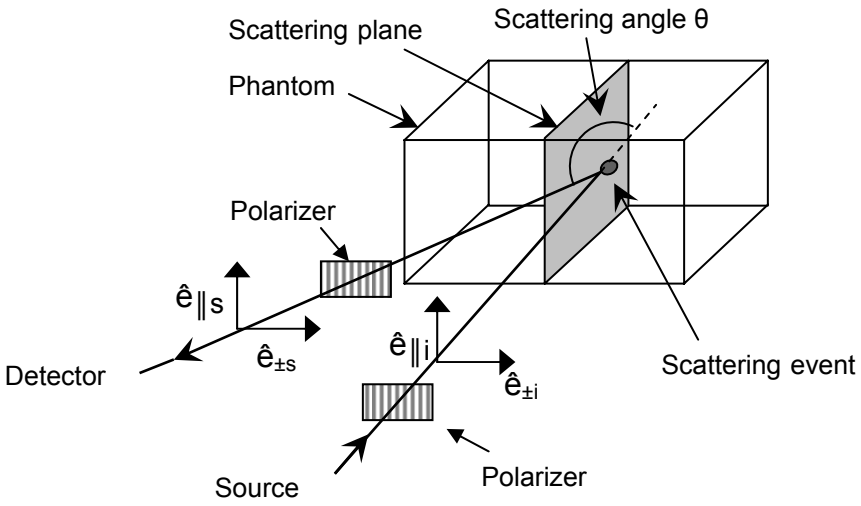

Figure 2.13 *A single scattering event considering the incident and the scattered light components. Adapted from Ref*[39].

The scattering matrix describes the relationship between the incident and scattered electric field components perpendicular and parallel to the scattering plane, as the following[18]

$$\begin{bmatrix} E_{\parallel s} \\ E_{\pm s} \end{bmatrix} = \frac{\exp(-ik(r-z))}{-ikr} \begin{bmatrix} S_2 & S_3 \\ S_4 & S_1 \end{bmatrix} \begin{bmatrix} E_{\parallel s} \\ E_{\pm i} \end{bmatrix} \tag{2.52}$$

The exponential term in Eq. (2.52), which is a transport factor, depends on the distance between the scatterer and observer. If one measures scattered light at a constant distance 'r' from the scatterer, then the transport factor becomes a constant[18]. The total field (E_{tot}) depends on the incident field (E_i), the scattered field (E_s), and the interaction of these fields (E_{int}). In practical experiments, if one observes the scattering from a position, which avoids E_i, then both E_i and E_{int} are zero and only E_s is observed. In practical scattering measurements, Eq. (2.52) simplifies to the following[39],

$$\begin{bmatrix} I_{\parallel s} \\ I_{\pm s} \end{bmatrix} = \text{cons tan t} \begin{bmatrix} |S_2|^2 & 0 \\ 0 & |S_1|^2 \end{bmatrix} \begin{bmatrix} I_{\parallel i} \\ I_{\pm i} \end{bmatrix} \tag{2.53}$$

For unpolarized incident light, it can be shown that

$$E_s = \frac{S_{11}}{k^2 r^2} E_i \tag{2.54}$$

where S_{11} is identical to the first element in the so-called Mueller matrix and in this case is defined by[1]

$$S_{11} = \frac{1}{2}|S_1|^2 + \frac{1}{2}|S_2|^2 \tag{2.55}$$

2.5.4 Reduced scattering coefficient

An expression for effective scattering in tissue should include both the scattering coefficient and the anisotropy factor. The reduced scattering coefficient μ_S' is a property incorporating these factors as the following,

$$\mu_S' = \mu_S (1\text{-}g) \tag{2.56}$$

The purpose of μ_S' is to describe the diffusion of photons in a random walk of step size of $1/\mu s'$, called reduced mean free path length, where each step involves isotropic scattering[39];

$$mfp_s' = \frac{1}{\mu_s'} \tag{2.57}$$

Such a description is equivalent to description of photon movement using many small steps $1/\mu_S$ that each involves only a partial deflection angle θ. This way to describe light propagation becomes important in cases where there are many scattering events before an absorption event, i.e. $\mu_a << \mu_S'$.

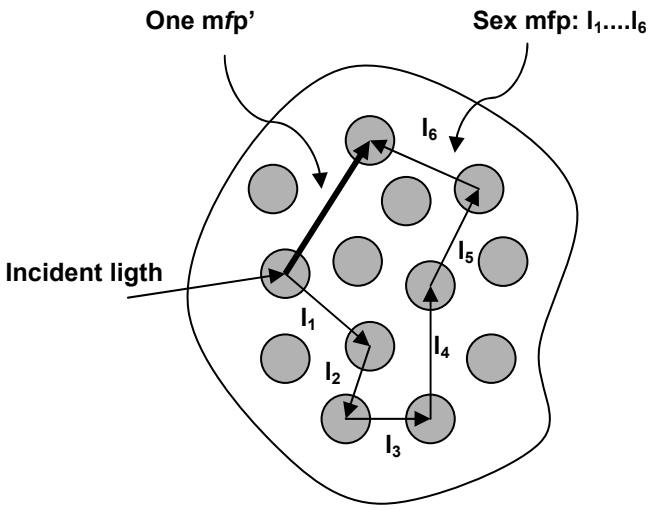

Figure 2.14 *The equivalence of 6 small steps of mfp = 1/μ_s with one mfp' = 1/μ_s'.*

This situation of scattering-dominated light transport is called the diffusion regime and μ_S' is useful in the diffusion regime, which is commonly encountered when visible and near-infrared light propagates through biological tissues. Figure 2.14 shows the equivalence of

taking 6 smaller steps of "mean free path" m*f*p = $1/\mu_s$ with anisotropic deflection angles and one big step with a "reduced mean free path" m*f*p' = $1/\mu_s'$.

2.6 Optical properties of biological media

In general, three photophysical processes affect light propagation in biological tissues: refraction, scattering and absorption[43]. These are defined in forms of refraction index (n), scattering coefficient (μ_s) and absorption coefficient (μ_a), respectively. Scattering of light occurs in media that contains fluctuations in the refractive index (n), whether such fluctuations are discrete particles or more continuous variations in (n).

In biomedical optics, scattering of photons is an important event. Scattering provides feedback during therapeutic procedures, and has diagnostic values as well. It depends on the ultrastructure of a tissue, e.g., the density of lipid membranes in the cells, the size of nuclei, the presence of collagen fibers, the status of hydration in the tissue, etc[39].

Another important event in biomedical optics is absorption of photons. Absorption is the primary event that allows a laser or other light source to cause a potentially therapeutic (or damaging) effect on a tissue. Without absorption, there is no energy transfer to the tissue and the tissue is left unaffected by the light. It also provides a diagnostic role, as well. Absorption can provide a clue as to the chemical composition of a tissue, and serve as a mechanism of optical contrast during imaging[39].

As stated earlier, scattering and absorption are defined by their coefficients. These coefficients are used and investigated as fingerprints in biological optics. While absorption coefficient (μ_a) provides information on the concentration of various chromophores[44], the scattering properties provide information on the form, size, and concentration of the scattering components in the medium[45,46]. The scattering properties are divided to scattering coefficient (μ_s), the reduced scattering coefficient (μ_s'), and anisotropy factor (g). The relation between the scattering properties has been shown by Eq. (2.56), earlier.

There are other terms of concerns in tissue optical properties, such as: the total attenuation coefficient (μ_t), and the effective attenuation coefficient (μ_{eff}), defined as following,

$$\mu_t = \mu_a + \mu_s \tag{2.58}$$

$$\mu_{eff} = \sqrt{3\mu_a\left[\mu_a + \mu_s(1-g)\right]} \tag{2.59}$$

2.6.1 Some biological chromophores and scatterers[39]

Molecules that absorb light are called *chromophores*. Depending how light is absorbed, these molecules are divided to two types: those that absorb light through electric transitions and those that absorb light through vibrational transitions. Electronic transitions

are relatively energetic and hence are associated with absorption of UV, VIS, and NIR wavelengths. Porphyrins are effective chromophores for absorbing photons. Hemoglobin and vitamin B_{12} are examples of porphyrins in biology. Protoporphyrin IX (PpIX) is one of the important factors in PDT (see Chapter 7). The field of infrared spectroscopy, studies the variety of bonds, which can resonantly vibrate or twist in response to IR wavelengths and thereby absorb such photons. Perhaps the most dominant chromophore in biology, which absorbs via vibrational transitions, is water. In the IR region, the absorption of water is the strongest contributor to tissue absorption.

About the biological scatteres, it can be said that the light scattered by a tissue has interacted with the ultrastructure of the tissue. Tissue ultrastructure extends from membranes to membrane aggregates, collagen fibers, nuclei, and cells. Photons are most strongly scattered by those structures whose size matches the photon wavelength. Scattering of light by structures on the same size scale as the photon wavelength is described by Mie theory. Scattering of light by structures much smaller than the photon wavelength is called the Rayleigh limit of Mie scattering, or simply Rayleigh scattering. Mitochondria, collagen fibers, and fibrils are examples of structures which scatter light in biology.

Mitochondria are intracellular organelles about 1 μm in length (variable) which are composed of many folded internal lipid membranes called cristae. The basic lipid bilayer membrane is about 9 nm in width. The refractive index mismatch between lipid and the surrounding aqueous medium causes strong scattering of light. Folding of lipid membranes presents larger size lipid structures, which affect longer wavelengths of light. The density of lipid/water interfaces within the mitochondria make them especially strong scatterers of light. Collagen fibers (about 2-3 μm in diameter) are composed of bundles of smaller collagen fibrils about 0.3 μm in diameter (variable). Mie scattering from collagen fibers dominates scattering in the infrared wavelength range. About fibrils, it must be said that the periodic fluctuations in refractive index on this ultrastructureal level, appear to contribute a Rayleigh scattering component that dominates the visible and ultraviolet wavelength ranges.

Chapter 3

Light transport in tissue - theory and models

Light is life- share it with others.

Shri S. C. Pathak

3.1 Introduction

When light interacts with biological tissues, different processes can occur. These processes depend both on the intensity and wavelength of light and the type of the tissue that light interacts with. As it was discussed in the previous chapter, while most of the light enters the tissue, a small part of light, depending on the angel of incidence and the index of refraction, can be reflected from the tissue surface. Inside the tissue, light interacts with the outermost electrons of the molecules; resulting in absorption or scattering. These two processes, which are highly wavelength dependent, are the fundamentals of tissue optics. From measurements of tissue absorption and scattering-optical properties, physiological and structural information about the probed tissue such as the average cell size and shape, and the quantity of characteristic tissue biomolecules can be extracted. Light propagation in biological medium as multiple scattering medium, is fundamentally governed by the Maxwell's equations. However, the electromagnetic theory, in spite of preserving the wave

properties of the light, because of the complexity of the mathematical formalism is overwhelming; instead, in tissue optics light propagation in turbid media is investigated by models based on photon transport. These models are expressed as differential or integro-differential equations, e.g. the transport equations, which is derived from simple phenomenological consideration on the basis of the radiative transport theory[1,47]. In this chapter, the mathematical aspects of light transport in tissue will be discussed.

3.2 Propagation of light in tissue

Light propagation in tissue is modeled according to transport theory[47]. The fundamental difference between transport theory and electromagnetic theory is that, while electromagnetic theory describes light propagation by superposition of electromagnetic fields, transport theory basically relies on superposition of energy flux, so that the wave properties of light (e.g. polarization, interference, and etc.) are not considered in transport theory[38]. There are on the other hand also similarities between these two theories. For example, as it was discussed in the previous chapter, while in electromagnetic theory the Poynting vector **S** expresses the energy transport of electromagnetic waves, in transport theory equivalent of **S** is the flux vector **F**. In addition, the radiant power P transferred through a surface with the area A in electromagnetic theory,

$$P = \int_A \mathbf{S}.\mathbf{n}\, dA \tag{3.1}$$

can be compare with the power P (J/s = W) transferred through a surface with the area A within transport theory,

$$P = \int_A \mathbf{F}.\mathbf{n}\, dA \tag{3.2}$$

3.2.1 Transport theory

To be able to describe the propagation of light in turbid media, it is essential to explain some of the important optical parameters, which are used in modeling of light propagation in turbid media. Therefore, the propagation of photons, the radiance, fluence rate, and flux are introduced below[38].

3.2.1.1 Photon distribution function and photon power

The photon distribution function N(r,ŝ), is defined as the number of photons per unit volume moving in the direction of unit vector ŝ, in an element of solid angle containing ŝ, divided by that element, at a given point r. The power of the photons that propagate through the infinitesimal area dA in the infinitesimal solid angle $d\omega$ in the direction of ŝ, with velocity c_t, and energy hv (per photon) is defined as

$$\mathrm{d}p(\mathrm{r},\hat{\mathrm{s}})\ [\mathrm{Js}^{-1}=\mathrm{W}] = N(\mathrm{r},\hat{\mathrm{s}})\ \mathrm{d}A\ d\omega\ c_t\ h\nu \tag{3.3}$$

where c_t is the velocity of light in tissue ($c_t = c_0/n$). Note that dA is perpendicular to ŝ.

3.2.1.2 Radiance

In transport theory, light is modeled in terms of the radiance $L(\mathrm{r},\hat{\mathrm{s}})$ [W/sr], Figure 3.1(a). Radiance is the quantity used to describe the propagation of photon power with a certain direction ŝ, through a small surface dA,

$$L(\mathrm{r},\hat{\mathrm{s}}) = \frac{\mathrm{d}p(\mathrm{r},\hat{\mathrm{s}})}{\mathrm{d}A\ d\omega} \tag{3.4}$$

The radiance can thus be obtained by multiplying the light distribution function with the speed of light and energy of the photons in the medium as following,

$$L(\mathrm{r},\hat{\mathrm{s}}) = N(\mathrm{r},\hat{\mathrm{s}})\ \frac{hc_t^{\,2}}{\lambda} \tag{3.5}$$

where h is Planck's constant, c the speed of light inside the medium (c_t), and λ the wavelength of light inside the medium.

3.2.1.3 Fluence rate

The Fluence rate $\Phi(\mathrm{r})$, is the integral of the radiance over all directions, Figure 3.1(b). In biomedical optics, fluence rate is more practical than the radiance itself, as it deals with the propagations of photons in all direction. The fluence rate is defined as,

$$\Phi(\mathrm{r}) = \int_{4\pi} L(\mathrm{r},\hat{\mathrm{s}})\, d\omega \tag{3.6}$$

$\Phi(\mathrm{r})$ shows the total power incident on a small sphere at position r, divided by the cross-sectional area dA of the sphere.

3.2.1.4 Net flux

The net flux is defined in terms of radiance as the sum of elemental flux according to Figure 3.1(c),

$$F(\mathrm{r}) = \int_{4\pi} L(\mathrm{r},\hat{\mathrm{s}})\,\hat{\mathrm{s}}\, d\omega \tag{3.7}$$

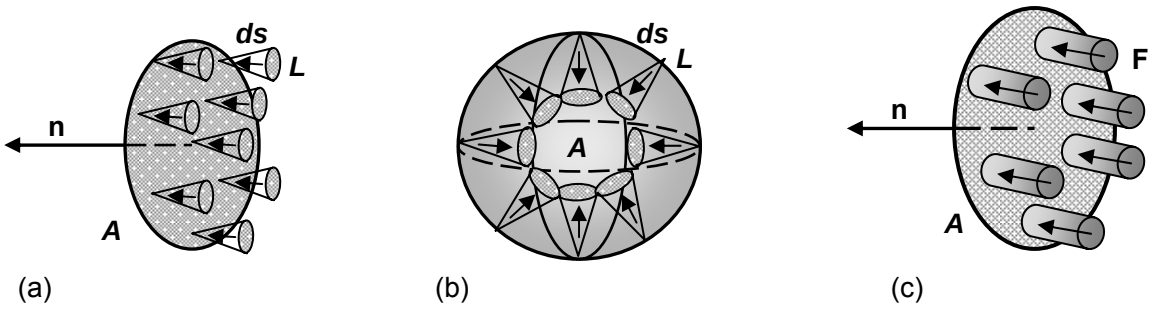

Figure 3.1 *Illustration of incident power P on an area A, described by three important optical parameter in transport theory: (a) the radiance L, (b) the fluence rate Φ, and (c) the flux* F. *Modified from Ref*[1].

From Eqs.(3.5) and (3.7), the power incident on the right-hand side of surface *A* in Figure 3.1(a), can be calculated as[1],

$$P = \int_{A}\int_{2\pi} L(\mathrm{r},\hat{\mathrm{s}})\ (\hat{\mathrm{s}}.\hat{\mathrm{n}})\ d\omega\ dA \tag{3.8}$$

Medical applications of lasers, often involves light incident on tissue. The amount of light can be expressed as the irradiance E_0 [W/m^2], which is defined as the radiant energy flux incident, on an element of the surface, divided by the area of the surface[38]. A portion of this incident light is reflected, and the portion of the beam entering the tissue is attenuated by scattering and absorption according to Beer's law,

$$\Phi(\mathrm{d}) = \mathbf{E_0}\ (1-\mathrm{R})\ \exp\left(-(\mu_a-\mu_s)\ \mathrm{d}\right) \tag{3.9}$$

where $\Phi(\mathrm{d})$ is the fluence rate due to the unscattered beam at position d, E_0 is the irradiance, and R is the Fresnel surface reflection. The penetration depth is defined according to the total attenuation coefficient, $\mu_t = \mu_a + \mu_s$ as,

$$\delta = \frac{1}{\mu_t} \tag{3.10}$$

3.2.1.5 Transport equation

Transport equation consists of different components and terms. In order to describe these terms, photons traveling at speed *c* in direction $\hat{\mathrm{s}}$ within a small volume *dV* are considered. Conservation of energy yields that photons can only be added to or subtracted from the photon distribution function in specific interactions. In this case, the first term of

the transport equation, expresses changes in the photon distribution function with time, Figure 3.2(a),

$$\int_V \frac{\partial N(r,\hat{s},t)}{\partial t}\, dV \tag{3.11}$$

The second term, shows the photons lost through the boundary that can be expressed as a surface integral, or by using Gauss' theorem as volume integral, Figure 3.2(b),

$$-\oint_S c\, N(r,\hat{s},t)\, \hat{s}.dS \qquad \text{or} \qquad -\int_V c\, \hat{s}\, \nabla N(r,\hat{s},t)\, dV \tag{3.12}$$

The third term expresses the absorption of incoming photons in the direction $\hat{s}$, Figure 3.2(c),

$$-\int_V c\, \mu_a(r)\, N(r,\hat{s},t)\, dV \tag{3.13}$$

The next term, shows the photons scattering from direction $\hat{s}$ into any other direction $\hat{s}'$, Figure 3.2(d),

$$-\int_V c\, \mu_s(r)\, N(r,\hat{s},t)\, dV \tag{3.14}$$

The fifth term yields the photons gained through scattering from any direction $\hat{s}'$ into the direction $\hat{s}$, Figure 3.2(e)

$$+\int_V c\, \mu_s(r) \int_{4\pi} p(\hat{s}',\hat{s})\, N(r,\hat{s}',t)\, ds'\, dV \tag{3.15}$$

And the last term expresses the photons gained through a light source "q", Figure 3.2(f),

$$+\int_V q(r,\hat{s},t)\, dV \tag{3.16}$$

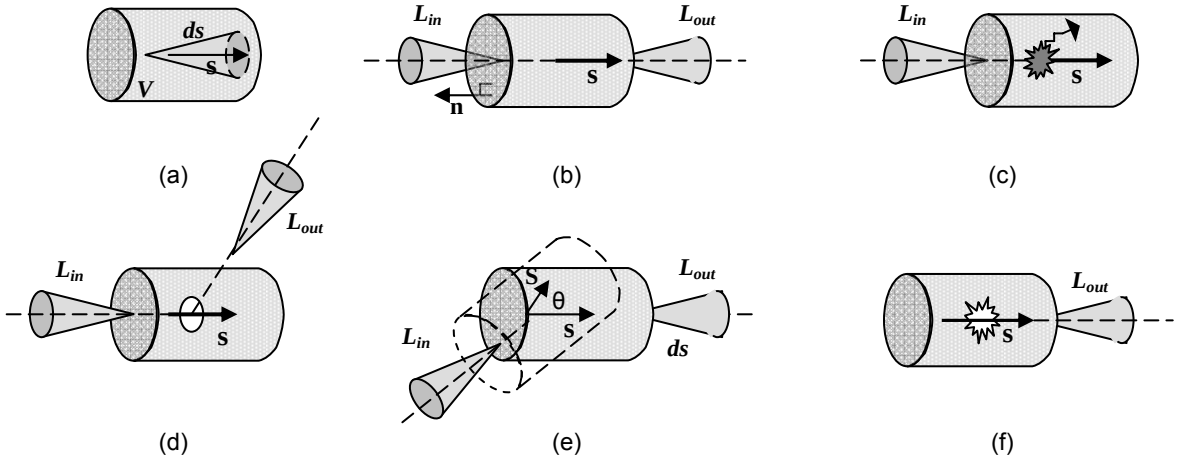

Figure 3.2 *Schematics of the transport equation component terms. (a) The energy of the photons in volume V, (b) losses through the boundaries, (c) losses due to absorption, (d) losses due to scattering, (e) gain through scattering from any direction to direction* $\hat{s}$ *, and (f) gain due to a light source within volume V. Modified from Ref*[1].

Finally, the time-dependent transport equation is presented as following,

$$\int_V \frac{\partial N(r,\hat{s},t)}{\partial t}\, dV = -\int_V c\,\hat{s}\,\nabla N(r,\hat{s},t)\, dV - \int_V c\,\mu_a(r)\,N(r,\hat{s},t)\, dV - \int_V c\,\mu_s(r)\,N(r,\hat{s},t)\, dV + \int_V c\,\mu_s(r) \int_{4\pi} p(\hat{s}',\hat{s})\,N(r,\hat{s}',t)\, ds'\, dV + \int_V q(r,\hat{s},t)\, dV \tag{3.17}$$

It must be noticed that despite all interactions with the medium, there is no loss or gain in photon energy due to the interaction and all the scattering is considered elastic here; in short, the transport equation is derived under the assumption that the energy of the non-absorbed photons are the same. Another assumption is restricted to monochromatic light for this analysis.

Dropping the volume integrals in Eq. (3.17), the time-dependent transport equation is obtained as the following;

$$\frac{1}{c}\frac{\partial L(r,\hat{s},t)}{\partial t} + \hat{s}\nabla L(r,\hat{s},t) + (\mu_a + \mu_s)\, L(r,\hat{s},t) = \mu_s \int_{4\pi} L(r,\hat{s},t)\, p(\hat{s}',\hat{s})\, ds' + q(r,\hat{s},t) \tag{3.18}$$

Now the transport equation has been formulated. The next step is to find its solution. Since it is very difficult to solve the transport equation analytically, various numerical and approximation methods are employed. These methods are classified in three groups called expansion method, probabilistic method, and discretisation method.

3.2.2 Diffusion theory

According to the expansion method, one way of solving the transport equation is to find the solution to its homogeneous part and expand the general solution in terms of the obtained homogeneous solution[47,48]. In diffusion theory, the radiance (L), the phase function (p), and the source function (q) of the transport equation Eq. (3.18), are then expanded in spherical harmonics. Hence, the expansion of L can be written as,

$$L(\mathrm{r},\hat{\mathrm{s}},\mathrm{t}) = \sqrt{\frac{1}{4\pi}}\, L_{00}(\mathrm{r},\mathrm{t})\; Y_{00}(\hat{\mathrm{s}}) + \sqrt{\frac{3}{4\pi}} \sum_{m=-1}^{1} L_{1m}(\mathrm{r},\ \mathrm{t})\; Y_{1m}(\hat{\mathrm{s}}) \tag{3.19}$$

By inserting the above expression into the transport equation, Eq. (3.18), and integrating over $\hat{\mathrm{s}}$, the four unknowns L_{00} and L_{1m} (m = 0, +1,-1) may now be found. Another approach is to observe that Y_{00} is a scalar and that Y_{1m} (m = 0, +1,-1) represent the three components of a vector, and thus the radiance can be expressed by them as[47]

$$L(\mathrm{r},\hat{\mathrm{s}},\mathrm{t}) = A(\mathrm{r},\mathrm{t}) + \overline{B}(\mathrm{r},\mathrm{t}).\hat{\mathrm{s}} \tag{3.20}$$

According to Eq. (3.20), it is seen that radiance is composed of an isotropic part $A(\mathrm{r},\mathrm{t})$ and an anisotropic part $B(\mathrm{r},\mathrm{t})$ that is the linear gradient of the photon distribution function, $\hat{\mathrm{s}}$ is the vector of gradient. By inserting Eq. (3.20) into Eq. (3.6), the fluence rate will be yielded as following,

$$\Phi(\mathrm{r},\mathrm{t}) = 4\pi\ A\ (\mathrm{r},\mathrm{t}) \tag{3.21}$$

Consequently, we may present the net flux, Eq. (3.7) as

$$\overline{F}(\mathrm{r},\mathrm{t}) = \frac{4\pi}{3}\,\overline{B}(\mathrm{r},\mathrm{t}) \tag{3.22}$$

Utilizing Eqs. (3.21) and (3.22) in Eq. (3.20), the radiance is expressed as

$$L(\mathrm{r},\hat{\mathrm{s}},\mathrm{t}) = \frac{1}{4\pi}\,(\Phi(\mathrm{r},\mathrm{t}) + 3\,\overline{F}(\mathrm{r},\mathrm{t})\cdot\hat{\mathrm{s}}) \tag{3.23}$$

Now, assuming that the light source (q) is isotropic, its expansion into spherical harmonics will be

$$q(\mathrm{r},\hat{\mathrm{s}},\mathrm{t}) = \frac{1}{4\pi}\ q_0\ (\mathrm{r},\mathrm{t}) \tag{3.24}$$

Finally, considering all the expanded term, the transport equation can be written as the following,

$$\frac{1}{c}\frac{\partial}{\partial t}\left(\Phi(r,t)+3\,\overline{F}(r,t)\cdot\hat{s}\right) = -\hat{s}\,.\,\nabla\left(\Phi(r,t)+3\,\overline{F}(r,t).\hat{s}\right) - (\mu_a+\mu_s)\left(\Phi(r,t)+3\,\overline{F}(r,t).\hat{s}\right) + \mu_s\int_{4\pi} p(\hat{s}',\hat{s})\left(\Phi(r,t)+3\,\overline{F}(r,t).\hat{s}\right)ds' + q_0(r,t) \tag{3.25}$$

Considering the scattering phase function, and applying Eqs. (3.23) and (3.24); Eq. (3.25) is reduced to

$$\frac{1}{c}\frac{\partial}{\partial t}\left(\Phi(r,t)+3\,\overline{F}(r,t).\hat{s}\right) = -\left(\hat{s}\,.\,\nabla+\mu_a\right)\Phi(r,t) - 3\left(\hat{s}\,.\,\nabla+\mu_a+\mu_s'\right)\overline{F}(r,t).\,\hat{s} + q_0(r,t) \tag{3.26}$$

Integrating this expression over $\hat{s}$ results in

$$\frac{1}{c}\frac{\partial\Phi(r,t)}{\partial t} = -\mu_a\,\Phi(r,t) - \nabla\,.\,\overline{F}(r,t) + q_0(r,t) \tag{3.27}$$

On the other hand, if Eq. (3.26) is multiplied by $\hat{s}$ and then the integration is carried out, it results in

$$\frac{1}{c}\frac{\partial\overline{F}(r,t)}{\partial t} = \frac{1}{3}\nabla\,\Phi(r,t) - (\mu_a+\mu_s')\,\overline{F}(r,t) \tag{3.28}$$

The last two expressions, Eqs. (3.27) and (3.28), are the basic equations of diffusion theory. By eliminating the dependent variable F, these two equations can be reduced to one equation. The steady-state solution of Eq. (3.28) presents Fick's law,

$$\overline{F}(r,t) = -D(r)\nabla\,\Phi(r,t) \tag{3.29}$$

where the diffusion coefficient D is introduced as,

$$D(r) = \frac{1}{3(\mu_a+\mu_s')} \tag{3.30}$$

Finally, from the last two equations, Fick's law and the diffusion coefficient expression, the time-dependent diffusion equation is obtained as the following,

$$\frac{1}{c}\frac{\partial \Phi(r,t)}{\partial t} - D(r)\nabla^2 \Phi(r,t) + \mu_a \Phi(r,t) = q_0(r,t) \tag{3.31}$$

It must be noticed that the diffusion equation is valid only if the propagating light is diffused, and this implies that the reduced scattering coefficient is much larger than the absorption, i.e.

$$\mu_s' >> \mu_a \tag{3.32}$$

The other point is that the source and detector must be separated in space and time to allow that the light is diffused when it reaches the detector. It has been shown that diffusion theory is inaccurate in applications that involve structures near the surface of the medium, small source-detector distances, and geometrical configurations with sharp discontinuities of the scattering properties[1,49].

3.2.2.1 Time- domain and point source solutions

For an infinite homogeneous medium or a medium with simple boundary conditions, and with a short pulse isotropic point source, i.e.

$$q_0(r,t) = \delta(0,0) \tag{3.33}$$

where δ is Dirac's delta function; the solution to the diffusion equation is a Green's function expressed as[50],

$$\Phi(r,t) = Q_s c\,(4\pi D c t)^{-3/2} \exp\left(-\frac{r^2}{4Dct} - \mu_a c t\right) \tag{3.34}$$

where Q_s is the energy of the short pulse from the point source at (t = 0) and "r" is the radial distance from the source.

When illuminating a small spot on the tissue surface, the source function cannot be described by an isotropic point source. In this case a line source consisting of isotropic point sources with an exponentially decay strength, proportional to exp [- (μ_a+μ_s') z] is used; where "z" is the distance from the boundary. Thus, the fluence rate can be calculated from an integral of Green's function for sources at all depths. Assuming that all the incident photons are initially scattered at a depth equal to the mean free path ($z = 1/\mu_s'$), simplifies the case for isotropic scattering, Figure 3.3. Here, source can be approximated with the simple delta-function, as the following[50,51],

$$q_0(r,t) = \delta(r-r_0)\,\delta(t) \tag{3.35}$$

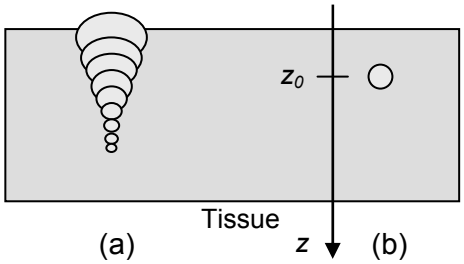

Figure 3.3 *Schematics of the two possible representations of the source. (a) A continuous line of sources with an exponential decay, and (b) the source at a depth of* $z = 1/\mu_s'$*, represented by delta function. Modified from Ref*[50].

The boundary conditions must be considered in solving diffusion equation for anything else than for an infinite medium. It means that, if the refractive indices are matched, the physical requirement is that there should be no photon flux back into the turbid medium at the surface. A good approximation is to introduce a virtual, or extrapolated boundary ($z=z_e$), and there apply $\Phi = 0$[52]. For index matching, one can derive the value $z_e \approx 2D$[19]. In index mismatched, i.e. when the tissue and the surrounding medium do not have the same refractive index, this distance will change; because of an internal reflection at the boundary[52,53]. For n = 1.4, an extrapolated boundary at $z_e \approx 5.5D$ is appropriate. The method of images or negative mirror sources, is introduced to set the fluence to zero at the extrapolated boundary[53]. As it is shown in Figure 3.4, the point source $z = z_0$, is mirrored in $z = -z_e$, resulting in a negative source at $z = -(2z_e + z_0)$.

Figure 3.4 *Schematic picture showing the principle of an extrapolated boundary at* $z = -z_e$ *, with* $\Phi = 0$*. A dipole source is placed symmetrically around the extrapolated boundary, with a positive part at* $z = z_0$*, inside the medium, and a negative part at* $z = -(2z_e + z_0)$.

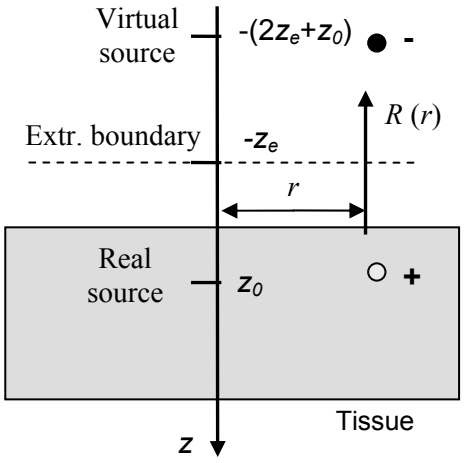

It should be noticed that when the observation of the radiance is made at a distance from the source that is considerably larger than the extrapolated boundary length, the zero radiance at the physical boundary is a valid approximation; but at too short distances, the diffusion approximation is not valid.

Now, the simple solutions for a semi-infinite homogeneous geometry can be derived. The time resolved diffuse reflectance is expressed as the following [51]

$$R(\mathrm{r},\mathrm{t}) = \frac{1}{2}(4\pi \mathrm{D}c)^{-3/2}\,\mathrm{t}^{-5/2}\exp(-\mu_a ct)\left[\mathrm{z}_0\exp\left(-\frac{\mathrm{r}_1^2}{4\mathrm{D}c\mathrm{t}}\right)+(\mathrm{z}_0+2\mathrm{z}_e)\exp\left(-\frac{\mathrm{r}_2^2}{4\mathrm{D}c\mathrm{t}}\right)\right] \tag{3.36}$$

The corresponding steady-state diffuse reflectance is expressed as

$$R(\mathrm{r}) = \left[\frac{1}{4\pi}\mathrm{z}_0\left(\mu_{\mathrm{eff}}+\frac{1}{\mathrm{r}_1}\right)\frac{\exp(-\mu_{\mathrm{eff}}\mathrm{r}_1)}{\mathrm{r}_1^2}+(\mathrm{z}_0+2\mathrm{z}_e)\left(\mu_{\mathrm{eff}}+\frac{1}{\mathrm{r}_2}\right)\frac{\exp(-\mu_{\mathrm{eff}}\mathrm{r}_2)}{\mathrm{r}_2^2}\right] \tag{3.37}$$

where

$$\mu_{\mathrm{eff}} = \sqrt{\frac{\mu_a}{\mathrm{D}}}\ ,\ \mathrm{r}_1 = \sqrt{\mathrm{z}_0^2+\mathrm{r}^2}\ ,\ \mathrm{r}_2 = \sqrt{(\mathrm{z}_0+2\mathrm{z}_e)^2+\mathrm{r}^2}\ ,\ \mathrm{z}_0 = \frac{1}{\mu_s'},\ \mathrm{z}_e \approx \mathrm{b}\mathrm{z}_0 \tag{3.38}$$

Here, "b" is dependent on the actual Fresnel reflection coefficient, for example, b = 2 for a typical tissue-air boundary[1].

The total diffuse transmitted light through a homogeneous slab, detected on the side opposite to the source, will then is written as the following,

$$\begin{aligned} T(\mathrm{d},\mathrm{t}) = {} & (4\pi \mathrm{D}c)^{-1/2}\,\mathrm{t}^{-3/2}\exp(-\mu_a ct)\times \\ & (\mathrm{d}-\mathrm{z}_0)\exp\left[-\frac{(\mathrm{d}-\mathrm{z}_0)^2}{4\mathrm{D}c\mathrm{t}}\right]+(\mathrm{d}+\mathrm{z}_0)\exp\left[-\frac{(\mathrm{d}+\mathrm{z}_0)^2}{4\mathrm{D}c\mathrm{t}}\right] \\ & +(3\mathrm{d}-\mathrm{z}_0)\exp\left[-\frac{(3\mathrm{d}-\mathrm{z}_0)^2}{4\mathrm{D}c\mathrm{t}}\right]-(3\mathrm{d}+\mathrm{z}_0)\exp\left[-\frac{(3\mathrm{d}+\mathrm{z}_0)^2}{4\mathrm{D}c\mathrm{t}}\right] \end{aligned} \tag{3.39}$$

where "d" is the thickness of the slab. Fitting the analytical solutions of Eqs. (3.36) and (3.39) to a measured reflectance or transmittance curve, will provide an estimate of optical properties μ_a and μ_s'. The g-value can never be evaluated with diffusion theory.

3.2.2.2 Frequency domain solutions

In frequency domain, instead of pulsed light source, a sinusoidal modulated light source with frequency *f*, is used to launch photons into the tissue[38]. The source fluence rate has

two components; AC (Φ_0) and DC (Φ_1). In this way, photon density waves are generated. These propagate in the tissue with fast decaying DC and AC amplitudes. The net fluence rate which describes the photon density wave initiated by a point source within an infinite homogeneous medium, can be written as[53,54]

$$\Phi(r,t) = DC(r) + AC(r)\exp[i(k_i - \omega t)]$$

$$= \Phi_0 \frac{\exp(-\mu_{eff} r)}{r} + \frac{\exp(-k_r r)}{r} \exp[i(k_i r - \omega t)] \quad (3.40)$$

where

$$\mu_{eff} = \left(\frac{\mu_a}{D}\right)^{1/2} = (3\mu_a(\mu_a + \mu_s'))^{1/2} \quad (3.41)$$

In comparison between light propagation in time domain and in frequency domain it can be said that in applying short pulse to a scattering medium, this pulse is broadened in time due to propagating to many paths between source and detector. Then, the observed quantity is the number of photons reaching the detector per unit time at a given time, $h(t)$. However, in frequency domain, applying the sinusoidially modulated light source, the observed quantity at the detector, are the phase angle between the detector and the source, and the amplitude of the oscillation relative to the DC level. In this case, the photon flux at the detector will be sinusoidal in time but the oscillation will be delayed in time relative to the source and reduced in amplitude relative to the average flux. The time domain signal $h(t)$ is linked to the modulation and phase by Fourier transformation so that any information obtained in the time domain can be obtained in the frequency domain, as well[38]. However, there are a few advantages of using frequency domain rather than time domain sources such as narrow band and noise resistant measurements in frequency domain measurements.

3.2.3 Monte Carlo simulations

In Monte Carlo (MC) technique, every simulation is based upon events that happen randomly, and so the outcome of a calculation is not always absolutely predictable. This element of chance reminds one of gambling, so the originators of the Monte Carlo technique, Ulam and von Neumann, called the technique Monte Carlo to emphasize its gaming aspect. MC simulations can be used for simulating all kinds of particle transport. It has mainly been developed for neutron transport in combination with nuclear reactions.

In tissue optics, Monte Carlo (MC) modeling is used as a technique for describing light transport in tissue, based on the transport equation and the random walk of photons in absorbing and scattering medium. In this case, the photons are considered as neutral particles and all wave phenomena are neglected.

In MC simulation, a photon package is traced through the tissue until it exits or is terminated due to absorption. Many physical parameters of the photon package such as the distribution of absorption, exiting position, time-of-flight, etc can be logged. By repeating the tracking process for a large number of photon packages, it is possible to obtain statistics for these physical quantities. In MC simulations, the key decisions are the mean free path for scattering or absorption event, and the scattering angle, see Figure 3.5(a). The number of photons needed depends on the problem and the wanted accuracy. Another aspect of the MC simulations is that they are based on macroscopic optical properties (μ_a, μ_s, and g) that are assumed to extend uniformly over small units of tissue.

The main advantage of MC method is that there is no limitation concerning boundary conditions or spatial localization of inhomogeneties in the tissue. On the other hand, the main drawback of MC is the problem of getting good statistics, particularly if the point of interest is located far away from the point of entry of the light and the scattering and absorption coefficients are high. For sampling the random variable x in MC simulation, a probability density p(x) is considered, which defines x over the interval $a \le x \le b$ such that:

$$\int_a^b p(x)dx = 1 \tag{3.42}$$

The probability that x will fall in the interval [a, x] is given by the distribution function $F_x(x_1)$ as the following,

$$F_x(x_1) = \int_a^{x_1} p(x)dx \tag{3.43}$$

By using a random number generator, one can obtain a random number ζ in the range of [0, 1]. The probability density function for this random number is 1 in the range [0, 1], and the corresponding probability distribution is as the following,

$$F_\zeta(\zeta_1) = \int_a^{\zeta_1} p(\zeta)d\zeta = \zeta_1 \quad , \quad 0 \le \zeta_1 \le 1 \tag{3.44}$$

This means that the picked random number gives the integrated value of p(x), which is the basic equation for sampling random variables from non-uniform distribution using uniformly distributed random number[55]. This equation is defined as

$$\zeta = F_x(x) = \int_a^{x_1} p(x)dx \tag{3.45}$$

This sampling principle in MC simulation is illustrated in Figure 3.6.

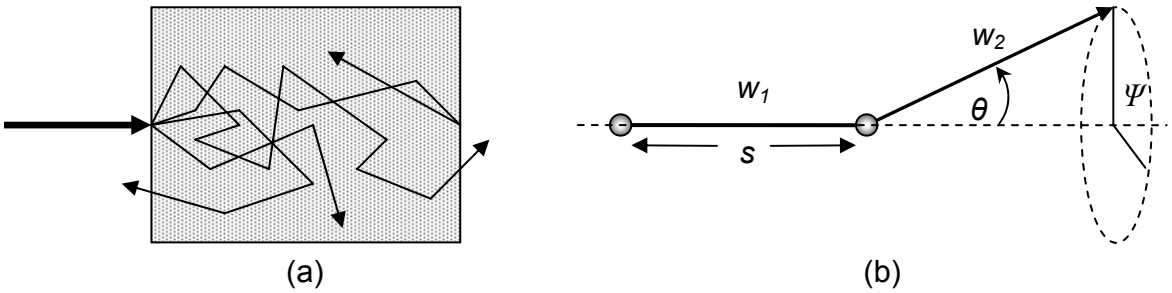

Figure 3.5 *Schematic of Monte Carlo simulations showing (a) random walks of multiple photons, and (b) the basic stochastic parameters governing the photon migration, i.e. step size s, scattering angle θ, and azimuth angle Ψ. Modified from Ref*[1].

The free path length of the photon between two interactions, called step size, is calculated based on the sampling probability for the interactions. From the probability for absorption, μ_a ds, and the probability for scattering. μ_s ds, the probability for any interaction is given by $(\mu_a+\mu_s)$ ds. Therefore, the probability density function of the step size "s", ($s\in [0, \infty]$), is defined accordingly as the following,

$$p_S = (\mu_a + \mu_s)\, e^{-(\mu_a+\mu_s)s} \tag{3.46}$$

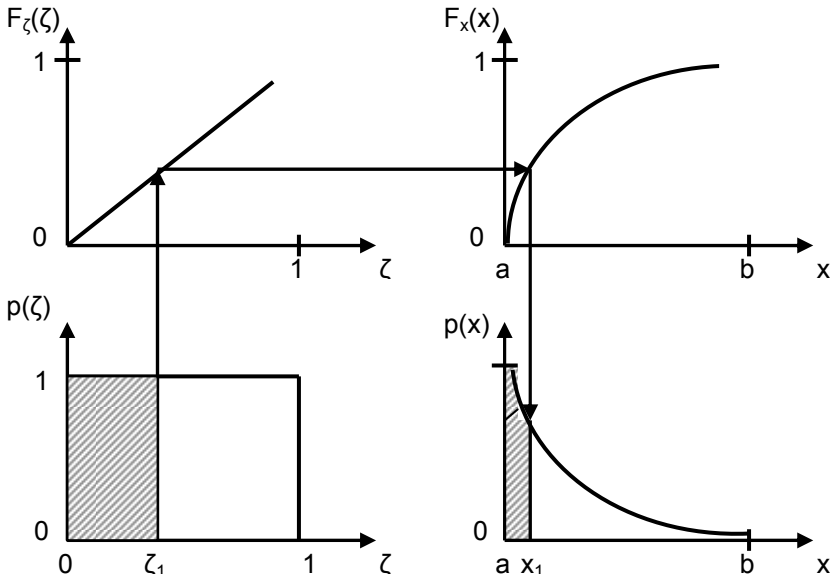

Figure 3.6 *Schematic of sampling of a random variable from a non-uniform distribution. The arrows show the mapping from the probability density function p (ζ), via the distribution function $F_\zeta(\zeta)$ and $F_x(x)$, to the probability density function p(x). The shaded areas are equal, but shown in different scale*[38,55].

From Eqs. (3.45) and (3.46), the step size, shown in Figure 3.5(b), can randomly be sampled as the following

$$s = \frac{-\ln(\zeta)}{(\mu_a + \mu_s)} \tag{3.47}$$

The scattering deflection angle θ is sampled from the Henyey-Greenstein distribution, within $[0, \pi]$. For convenience, $\mu = \cos(\theta)$ with μ distribution in the interval [-1, 1] is considered. Taking each step, photon looses a fraction of its energy due to the absorption. This can be described in form of the deposited energy (ΔQ) as the following,

$$\Delta Q = W \frac{\mu_a}{\mu_t} \tag{3.48}$$

where W is the photon weight. The new photon weight, ΔW, is given by

$$\Delta W = W \frac{\mu_s}{\mu_t} \tag{3.49}$$

Note that ($\Delta Q + \Delta W = W$) equals unity, so energy is conserved.

Now, the weight of the photon is reduced by ΔW, and the deflecting angle, $\theta \in [0, \pi]$, can be sampled by considering ($\mu = \cos\theta$) for convenience, as the following,

$$\cos\theta = \frac{1}{2g}\left(1 + g^2 - \left(\frac{1 - g^2}{1 - g + 2g\zeta}\right)\right) \quad \text{for} \quad g \neq 0$$

, and

$$\cos\theta = 2\zeta - 1 \quad \text{for} \quad g = 0 \tag{3.50}$$

For Mie scattering the Henyey- Greenstein (HG) which is a good approximation for the probability density function, is sampled as

$$p(\mu) = \frac{1 - g^2}{2(1 + g^2 - 2g\mu)^{3/2}} \tag{3.51}$$

The HG approximation implies symmetric scattering around the direction of propagation, in other words, the azimuthal angle, Ψ, is uniformly distributed within the interval $[0, 2\pi]$.

Thus, Ψ, is sampled as the following,

$$\Psi = 2\pi\zeta \tag{3.52}$$

For each step one has to check if the photon package crosses an internal or external boundary. If this is the case, the reflection and/ or escape must be checked by utilizing the Snell and Fresnel laws. The escaped fraction adds to the result file and reduces the left weight of the photon package. After a certain number of scattering events, the remaining photon package weight will be low. Thus, by applying a technique called *roulette*, an efficient MC code is to use. This technique gives a package a chance of m of surviving with a weight mW; otherwise the weight is reduced to zero and the package is terminated. This cycle of calculations repeatedly continues until the photon leaves the medium or terminated.

As already discussed, in MC simulations, results can be recorded as absorbed, reflected, or transmitted fraction. These functions can be recorded as a function of position, trajectory direction, and time.

Computer code for MC simulations is written using the guidelines above. A standard MC program for MC simulation in the filed of tissue optics for Multi-Layered media, MCML, written by Jacques and Wang, is well known[56,57]. This program is written in C. All simulations performed in this thesis were don using codes based on MCML.

As it was explained already, the MC method has been widely used to solve radiative transfer problems due to its flexibility and simplicity in simulating the energy transport process in arbitrary geometries with complex boundary conditions. However, the major drawback of the conventional (or forward) Monte Carlo method (FMC) is the long computational time for converged solution. Reverse or backward Monte Carlo (RMC) is considered as an alternative approach when solutions are only needed at certain locations and time. The reverse algorithm is similar to the conventional method, except that the energy bundle (photons ensemble) is tracked in a time reversal manner. Its migration is recorded from the detector into the participating medium, rather than from the source to the detector as in the conventional MC. There is no need to keep track of the bundles that do not reach a particular detector. Thus, RMC method takes up much less computation time than the conventional MC method. On the other hand, RMC will generate less information about the transport process as only the information at the specified locations, e.g., detectors, is obtained.

In the situation where detailed information of radiative transport across the media is needed the RMC may not be appropriate. RMC algorithm is most suitable for diagnostic applications where inverse analysis is required, e.g., optical imaging and remote sensing[58]. Figure 3.7, shows the schematics of forward and reveres MC. As it is seen from this figure, the main discrepancies are expected at the interface between two layers with different refractive indices.

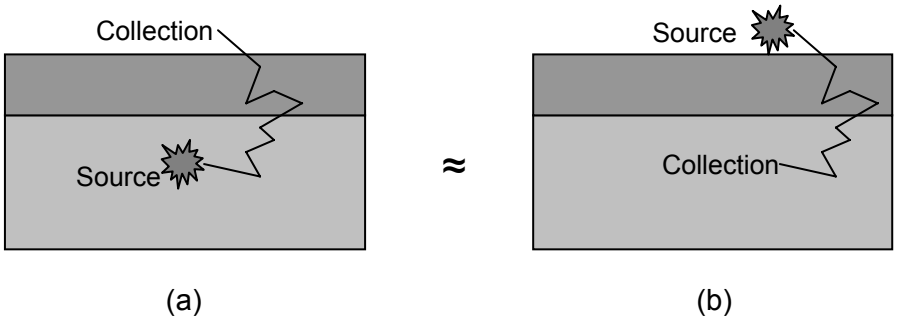

Figure 3.7 *Schematic of the two types of Monte Carlo simulations, (a) Forward MC, and (b) reverse MC*

3.2.4 The adding-doubling method

The adding-doubling (A-D) method is another way for solving the radiative transport equation, with accurate solution for anisotropic scattering and mismatched boundaries with arbitrary sample thiknesses[59]. It yields angle-dependent reflection and transmission readily, while especially reflectance is important for diagnostic applications using light. The general idea of A-D method is that, it assumes knowledge of the reflection and transmission properties for a single thin homogeneous layer; then, the reflection and transmission for an arbitrary thick slab are obtained by repeatedly doubling until the desired thickness is reached. The adding method extends the doubling method to dissimilar slabs, thereby allowing one to simulate different layers and/ or internal reflection at boundaries[60]. The main disadvantages of this method are that it is (a) restricted to layered geometries with uniform irradiation, and (b) necessary that each layer have homogeneous optical properties.

The inverse adding-doubling (IAD) is also another method for generating the optical properties of turbid media. Reflection and transmission measurements, typically made with an integrating sphere (see Chapter 4), are converted to the optical properties of the sample using a computer program. The IAD model, finds the optical properties characterizing a sample by using reflection and transmission measurements. A set of optical properties is guessed and the reflection and transmission is calculated. These values are compared with the measured reflection and transmission values. If they match then the optical properties for the sample have been found. If they do not match then a new set of optical properties is guessed and the process is repeated[61].

3.3 Polynomial regression

Although analytical expressions for R (μ_a, ,μ_s, g) and T (μ_a, μ_s, g) are provided by different methods such as diffusion theory[62], the inverse problem of determining μ_a (R,T) and μ_s (R,T), has no analytical solutions[63]. Furthermore, the analytical solutions of R (μ_a, μ_s) and T (μ_a, μ_s) are not accurate; thus most contemporary approaches are based on numerical methods, which provide more accurate calculations of R (μ_a, μ_s) and T (μ_a, μ_s),

e.g., the inverse adding–doubling (IAD) or methods involving Monte Carlo simulations[15,63]. For all the above methods it is common that μ_a (R, T) and μ_s (R, T) have to be determined by iterative numerical calculations. This may prove to be too slow in some cases. So, the inverse problem can be solved using a fast root solver. In Papers I, II and V, this method has been employed. A pre-computed result was generated, yielding maps of R and T as functions of μ_s' and μ_a. The Monte Carlo data were then fitted to an expansion of Chebyshev polynomials with least-squares regression, according to Eq. (3.53). Chebyshev polynomials form a complete orthogonal function set and are thus suited for this kind of expansion[55], see Figure 3.8.

$$P(\mu_a, \mu_s', m) = (a_0 + a_1 \mu_a + a_2 \mu_a^2 + ... + a_m \mu_a^m) \times (b_0 + b_1 \mu_s' + b_2 \mu_s'^2 + ... + b_m \mu_s'^m) \quad (3.53)$$

where (a_0, a_1, a_2, ...and b_0, b_1, b_2, ...) are fitting coefficients determined by least-squares regression, and m is the order of the double polynomial. The resulting polynomials fit to simulated R (R_{sim}) and simulated T (T_{sim}), were defined as[63]

$$R_{fit} = P_R(\mu_a, \mu_s', m)$$
$$T_{fit} = P_T(\mu_a, \mu_s', m) \quad (3.54)$$

To solve the inverse problem of extracting the optical properties from the measured values, it means R_{meas} and T_{meas}, new polynomials are formed, as the following,

$$F(\mu_a, \mu_s') = R_{fit} - R_{meas}$$
$$G(\mu_a, \mu_s') = T_{fit} - T_{meas} \quad (3.55)$$

The solution is obtained by finding the common roots of the polynomial equations formed by setting these polynomials equal to zero[55]. A Newton-Raphson algorithm was used for this purpose.

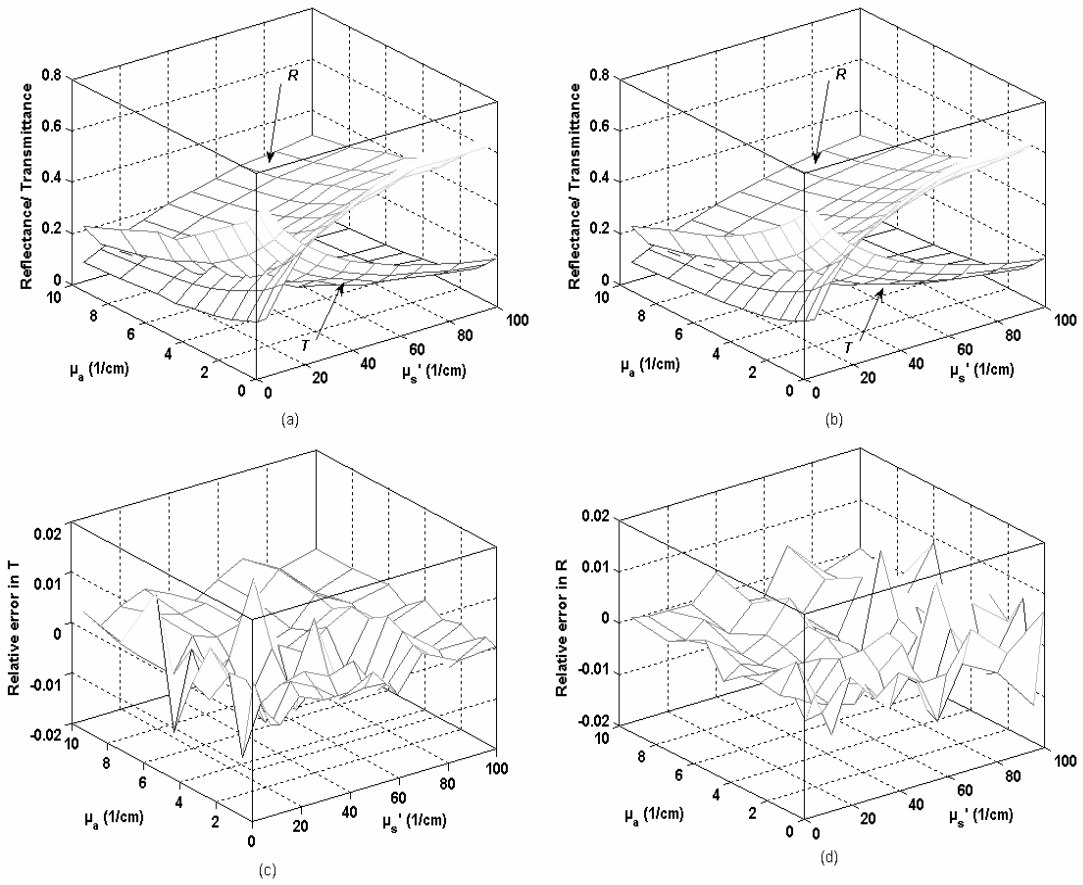

Figure 3.8 *Polynomial regressions for Monte Carlo data to solve the inverse problem for integrating sphere measurements. (a) Monte Carlo computed data for R and T, (b) the corresponding fitted polynomials; (c) and (d) show the relative error between the Monte Carlo data and the polynomials for T and R, respectively.*

3.4 Tissue phantoms

Usually, in order to validate the light propagation models, and also for calibrating and testing the validation of the systems used for measuring the optical properties; artificial samples are needed. This artificial samples, called tissue phantoms, must be easy to make and shape; and must be stable and reproducible to be trusted to use for calibration and validation purposes. Also, they should be matched with the optical properties in terms of scattering coefficient (μ_s'), absorption coefficient (μ_a), anisotropy factor (g), and refractive index (n), over the entire spectral range of interest[55,64]. There are many different tissue phantoms from liquid to hard forms, but most of them are either water or resins based. Epoxy is one of the most common materials used as a hardener to make solid phantoms.

3.4.1 Water-based phantoms

Ordinary milk is the simplest phantom material. The scatter contents of milk are the fat droplets and proteins suspended in the water[55,65]. The only absorber in pure milk is water, which considering Figure 2.5, it has very low absorption in the visible spectrum; and starts increasing the absorption when approaches the NIR region. However, by adding dyes or ink into milk, absorption can be obtained in other parts of the spectrum. Relatively high absorption of water at 970 nm, is a problem in using milk as water-based phantom, if the measurements over 900 nm are to be done[55]. The main problem of using milk as a phantom material is that milk does not have well defined optical properties, and it also can not be verified by theory. Instead, another material, called *Intralipid* or *Nutralipid*, which is a suspension of lipid particles, is used most often in investigations, as tissue phantom[63,66-68]. Intralipid which is very similar to milk in composition, has a long and glorious history of being measured, and also is used clinically as an intravenously administered nutrient, and in research provides the scattering component in a tissue phantom to investigate the propagation of light in tissue [69]. In Papers II, and V, different concentrations of intralipid, providing different scattering coefficients have been used.

However, there are advantages and disadvantages of using intralipid for making tissue phantoms. The quality of the intralipid can be controlled, and as it is sterile, it can be kept longer, but still its optical properties are not particularly well defined[55]. On the other hand, intralipid it is a food substance and not an optical medium. Consequently, no effort has been made to make all bottles of intralipid optically equal. Moreover, it seems that the optical properties of a bottle of intralipid change over time. Experiments show that a variation in order of 20 % can be seen from the values Van Staveren *et al.* are predicting for intralipid-10 %[69]. One must be careful in choosing absorber to add to the phantoms, as some absorbers changes the scattering properties of the phantoms. In general, acidic dyes can cause the fat emulsion of the intralipid to split[55]. Some of the dyes used as absorber, are: food dyes (in the visible region), carbon-based inks (in the NIR), inks, and etc.

3.4.1.1 Polystyrene microspheres

Suspension of monodisperse microspheres is the best water-based phantoms, but expensive ones. Apart from the possibilities of keeping the microsphere suspension longer than the intralipid ones, the main advantage of using this type of phantoms is that as the size of the scattering spheres is known, it is possible to do the Mie calculation for the scattering properties, and hence the g-value can be controlled[55]. Microsphere suspensions have been used in an investigation not presented in this book, when a comparison between optical properties measurement with IS method and optical coherence tomography method was performed.

3.4.2 Resin phantoms

Plastics phantoms are stable and reproducible, on the other hand as solid phantoms it is possible to make them in different shapes and embedded inhomogeneities, but making them is complicated and once it has been set, there is no possibility to alter their

properties. Curing plastics such as polyester and epoxy resins are commonly used in laboratories as phantom materials, since the scattering and absorbing agents can easily be mixed with the liquid resin. In Paper I, the phantoms used for the investigation were made of epoxy resin with an aliphatic amine as hardener, and TiO_2 powder as scatterer.

3.4.3 Refractive index

Usually, the main contents of tissue phantoms are either water or resin. The real tissue refractive index is n = 1.4, while for water and resin is 1.33 and 1.55, respectively. For validation purposes, these differences may not be of concern, since a model that is accurate for each one, is likely to be so for the other one. However, for calibration purposes, this might be needed to be taken under consideration[55].

Chapter 4

Measurement of tissue optical properties - methods & instrumentation

You see things; and you say, "Why?
" But I dream things that never were;
and I say "Why not?"

George Bernard Shaw

4.1 Introduction

As it was described already, the propagation of light in a medium is described by its optical properties. The fundamental optical properties of interest are the absorption coefficient, μ_a, scattering coefficient, μ_s, total attenuation coefficient, μ_t, scattering anisotropy, g, reduced scattering coefficient, μ_s', effective attenuation coefficient, μ_{eff}, and the tissue refractive index, n [70]. One way to classify the techniques for measuring optical properties, is to divide them into *in vivo* and *in vitro* methods. Another way of classification is to divide the techniques into *direct* and *indirect* methods. The direct one refers to measuring a particular microscopic coefficient, independent of any light propagation model in tissue, such as diffusion approximation or adding-doubling model. Indirect methods involve, on the other hand, derivation of the optical properties from results of e.g. reflection or transmission measurements by solving an *inverse problem.* In

inverse problems, the optical properties can be obtained by an iteration algorithm. Values of optical properties are guessed and inserted in a light propagation model, and then reflection and transmission values are computed, so that the optical properties are adjusted until the computed reflection and transmission values are matching the measured ones[71,72]. All these techniques, can be further sub-divided in three major divisions called, one-parameter, two-parameter, and three-parameter techniques.

4.2 One-parameter techniques

In this technique, the number of possible unknowns is N=1, meaning that only one of the tissue optical properties is derived. The *narrow-beam* method, illustrated in Figure 4.1, is such a technique. Here the fraction of light passing straight through an optically thin sample without interacting is measured. The signal is called the collimated transmittance[15]. The total attenuation coefficient, $\mu_t = \mu_a + \mu_s$, can thus be obtained by using the Beer-Lambertian law, Eq. (4.1).

$$I = I_0 \exp(-\mu_t d) \tag{4.1}$$

Figure 4.1, shows the schematic set-up for narrow beam transmission measuring, using a collimated detector[73,74].

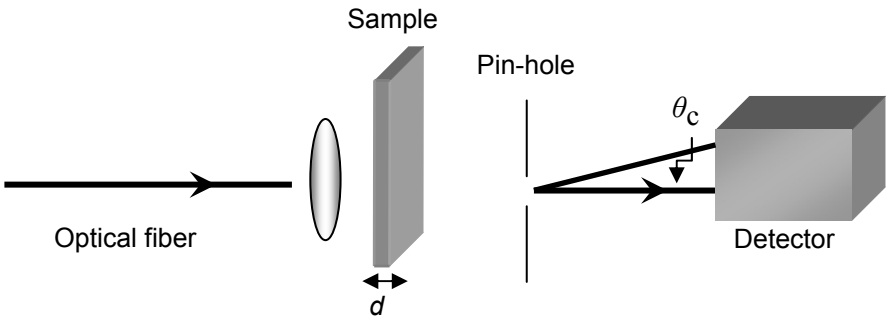

Figure 4.1 *Schematic of narrow beam set-up.*

Here, the validity of the derivation of μ_t is critically dependent on how true the assumption that the detected scattered light is negligible compared with the detected unscattered light is. Two experimental factors affect this assumption: one is the collection angle θ_c of the detector, and the other is the scattering optical depth $\mu_s d$ of the sample. The collection angle determines the percentage of scattered photons collected by the detector, while the scattering optical depth determines the number of scattered photons compared with the unscattered photons[75]. This measurement is thus suitable for optically thin samples only. For optically thick samples, this measurement provides interesting data, only if the multiple scattered light is prevented from reaching the detector. This can be assured by providing a large distance between the sample and detector and utilizing small apertures in front of the detector[15]. In narrow-beam measurement, the relative error of the measurements increases non-linearly with sample thickness and scattering coefficient. The

measurements include recording a beam passing through the tissue, as well as an unattenuated beam, yielding a reference measurement. The limitations posed by the limited dynamic range in the detection can be overcome by using calibrated neutral density filters in the light path for the reference measurement. In addition, the scattered light intensity can be reduced by placing two polarizing filters with parallel polarization axes before and after the sample[76,77].

4.3 Two-parameter techniques

In two parameter methods in this field, the unknowns are usually the reduced scattering (μ_s') and absorption (μ_a) coefficients. It is frequently impossible to measure μ_s by the methods under this category. As these methods often apply to dense tissues, the advantage is the possibility to perform *in vivo* measurements. The two-parameter methods are typically based on measurements of the diffuse reflectance or transmittance from the medium. To extract the optical properties, these measured quantities are followed by inverse computation and fitting procedures, which have been described above. In two-parameter techniques, the measured diffuse reflectance or transmittance of medium can be analyzed with three different methods; spatially-, time-, and frequency-resolved methods. The concepts of those are shown in Figure 4.2.

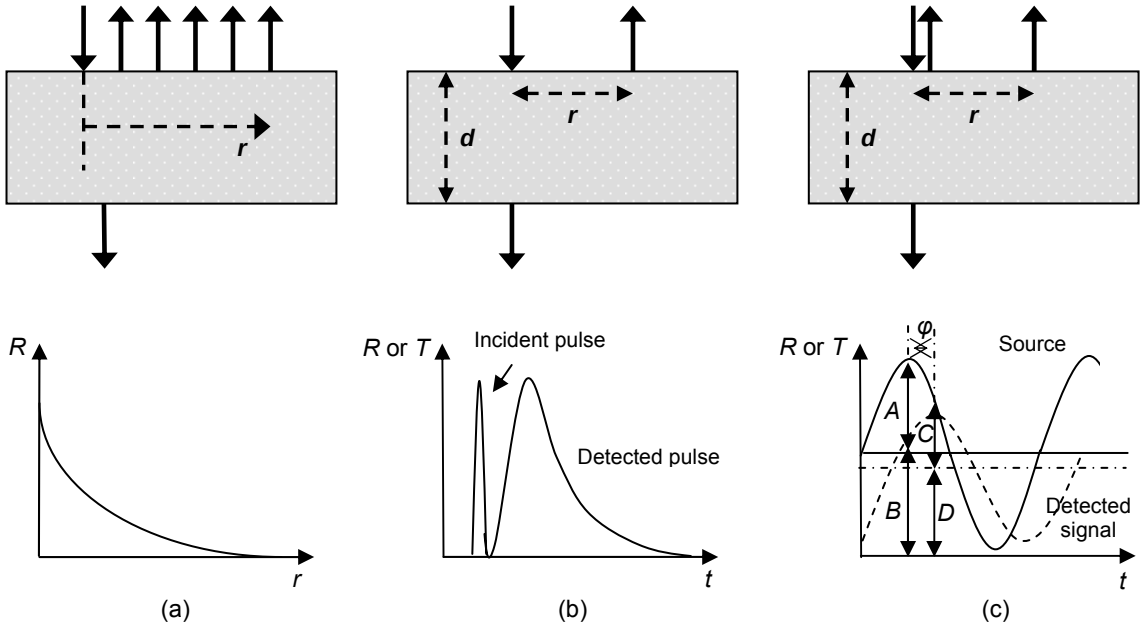

Figure 4.2 *The principles of the three different two-parameter techniques: (a) CW spatially resolved reflectance measurements, (b) time-resolved measurement by injecting a short pulse and measuring the temporal point-spread function (either reflectance or transmittance mode), and (c) frequency-modulated measurement (either reflectance or transmittance mode). In (c), the phase shift φ and the modulation depth, (C/D)/ (A/B), are measured. Modified from Ref*[55].

4.3.1 Spatially resolved techniques

In this technique, as it has been illustrated in Figure 4.2(a), the diffused reflected continuous wave (CW) is monitored as a function of its distance from the incident beam. The evaluation is normally done by fitting the measured $R(r)$ to the solution of the diffusion equation. In this technique, the light probes somewhat different volumes and at slightly different depths depending on the distance from the light source, see Figure 4.3.

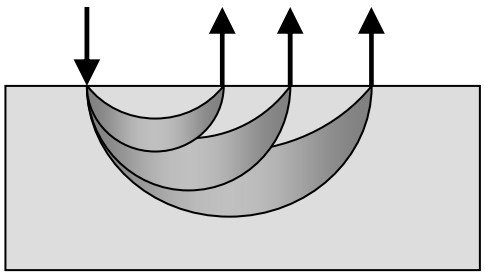

Figure 4.3 *The CW reflectance for different source-detector distances.*

In Figure 4.3, the shape of the radial, which depends on the reflection, is determined by the optical properties of the tissue. Hence, in highly scattering tissue, photons will have longer propagation before they are detected; higher reflectance in the reflectance pattern is yielded. Therefore, in the tissue with higher scattering properties, great reflectance over the entire radial range is produced. Moreover, a very isotropically scattering tissue, results in higher reflectance close to the center. The reduced scattering coefficient and the absorption coefficient can be obtained from analytical fitting expression generated by the diffusion equation[52,78,79], and also Monte Carlo method[80,81] Although, since the measurements are performed close to the light source; the diffusion equation might not be an ideal model for the light transport. There are advantages and disadvantages of using spatially resolved technique for extracting optical properties. Small, portable and inexpensive instrumentation together with possibility of performing measurements on patients *in vivo*, are the main advantages of this technique, while sensitivity of this method to inhomogeneities in tissue together with the limitation of measurements for deep structures inside the medium, are the main drawbacks.

4.3.2 Time-resolved techniques

In time-resolved measurements, a combination of short pulse light source (picoseconds) and a fast detector is employed. As it is schematically shown in Figure 4.2(b), the temporal behavior of the diffuse reflected pulse is detected at some distance from the incident light. The optical properties can be evaluated by fitting the solution of the diffusion equation to the result of a measurement. Alternatively, time-resolved Monte Carlo simulations, can also be employed in the data analysis[15,82,83]. In time-resolved method, the shape of the detected signal is more important than its absolute intensity; because the shape of the signal is characteristically influenced by the optical properties of

the medium[51,84-86]. It means that, the absorption coefficient (μ_a) affects the final slope of the attenuation curve, while the early part of the curve is practically invariant of μ_a. The reduced scattering coefficient (μ_s'), on the other hand, does not affect the final slope to any higher degree, but only the early part of the curve. The scattering increases the effective path length of light in tissue, meaning that an increase in scattering coefficient will effectively shift the peak of the time-resolved curve towards longer recording times.

In comparing the time-resolved and the spatially resolved techniques, it can be said that time-resolved measurements is relatively less sensitive to small inhomogeneities. This gives an advantage for *in vivo* measurements on patients. The main disadvantage of this technique is the relatively complicated and expensive instrumentation required.

4.3.3 Frequency-resolved techniques

In this technique a sinusoidally amplitude-modulated source is used to launch photons into the tissue rather than a pulsed light source used for time-resolved measurements[26]. In this way, a photon density wave, associated with a certain phase velocity, is propagating in tissue[15]. As can be seen in Figure 4.2(c), the amplitude modulation $\left((C/D)/(A/B)\right)$, decreases and the phase φ shifts when the light propagates in tissue. These changes are due to the absorption and the scattering properties of tissue. A Fourier transformation of the time-resolved diffusion equation, links the measurements to μ_s' and μ_a[87]. With constant source-detector distance and modulation frequency, it can be shown that a decreasing absorption coefficient or increasing effective scattering coefficient, results in a larger phase shift and weaker modulation[15,54,87,88].

4.4 Three-parameter techniques

The most frequently used method of measuring optical properties of small tissue volumes is the integrating sphere (IS) technique. This method is used to probe a thin slice of excised tissue [89]. It can be employed as either a three-parameter technique for extracting μ_a, μ_s, and g from measured total diffused reflectance (R_{tot}), total diffused transmittance (T_{tot}) and collimated transmittance (T_{col}), or as a two-parameter technique for measuring μ_a and μ_s' from the recorded values of R_{tot} and T_{tot}[90]. The technique has been shown to provide relatively accurate results for tissue phantoms[63]. It can, however, be debated how much the optical properties of tissues are affected by tissue excision and sample preparation.

4.4.1 The integrating sphere method

According to S. Prahl (1999), there is a long history of the use of integrating spheres. Good 'ole Ulbrecht reported the first one a hundred years ago. Utilizing an integrating sphere (IS) method, measurements of the total and collimated transmittance as well as diffuse reflectance, can be conducted. The sphere has an inner surface covered by highly reflecting barium sulphate. Light transmitted through a thin tissue sample (around 1mm

for biological tissue) when placed at entrance port, facing the light source, is scattered in the highly scattering surface of the sphere until reaching the detector. Similarily, the diffusely reflected light flux is measured by placing the tissue sample at the exit port of the sphere. The scattering by the integrating sphere transfers the transmitted and reflected light to diffuse light fluxes, being independent of its initial direction, and thus allows it to be probed by the detector with the same sensitivity independent on the direction of the light as it escapes the tissue sample. The detector may consist of an optical fiber or bundle guiding the collected light to a spectrometer to allow simultaneous measurements in a broad wavelength-range, see Figure 4.4. Measurement with IS system is following a few steps. First, it requires a background recording, and it is performed while all the ports of the sphere are blocked, Figure 4.4(a). Then, a reference measurement is performed. The reference intensity, I_{ref}, is probing the light flux filling the sphere without any tissue sample present, but with merely a highly diffuse reflective barium sulphate plug at the exit port, Figure 4.4(b). The barium sulphate plug is a calibration standard with a well known diffuse reflectivity, R_{BS}.

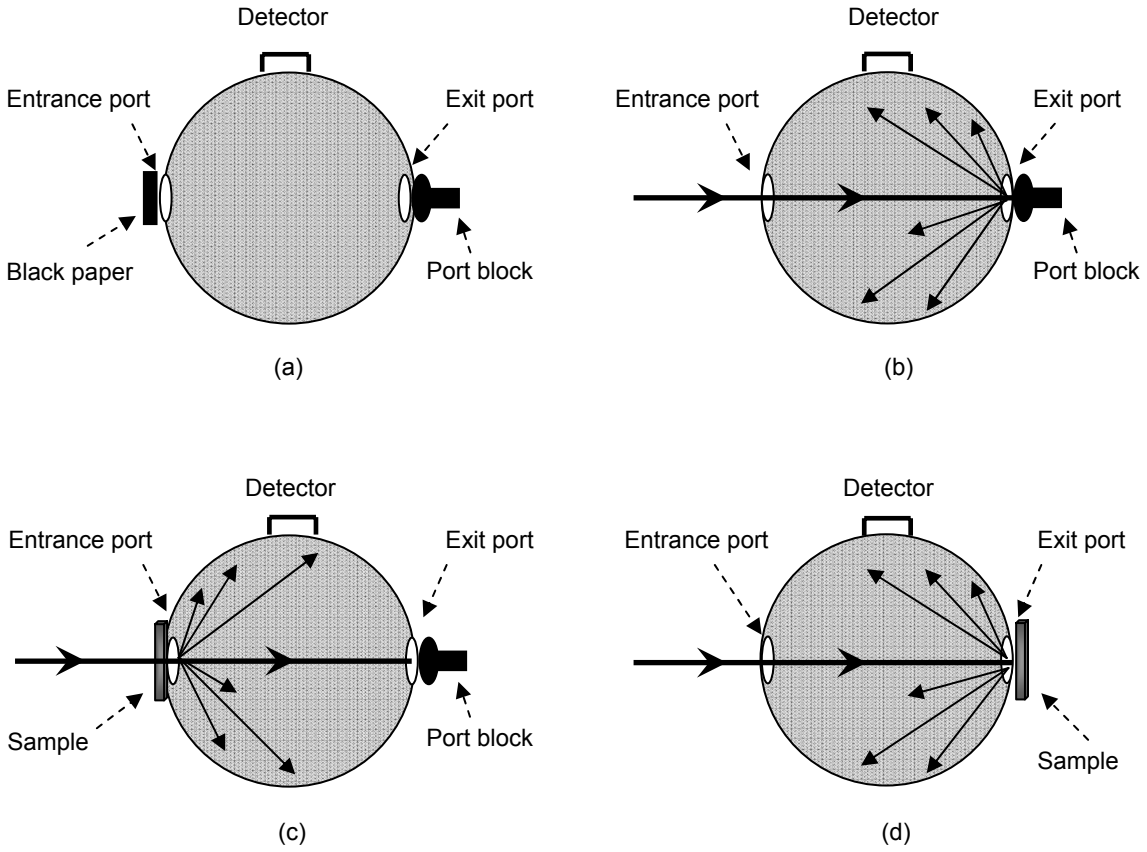

Figure 4.4 *The configuration of the integrating sphere measurements. The basic set-up for performing (a) the background measurement, (b) the reference measurement by using the calibrated barium sulphate plug at the exit port, (c) the transmitted signal measurement through the sample, and (d) the reflected signal measurement from the sample.*

Next, with placing the sample at the entrance port and keeping the exit port blocked, the transmission of light through the sample, I_T, is measured, see Figure 4.4(c). Finally, the sample is repositioned at the exit port, where the diffuse reflected light from the sample, I_R, can be measured. For this measurement the entrance port is kept open, see Figure 4.4(d). The reflectance and transmittance can then be determined by the following formulas, respectively:

$$R = R_{BS} \cdot \frac{I_R}{I_{ref}} \tag{4.2}$$

$$T = \frac{I_T}{I_{ref}} \tag{4.3}$$

By measuring both R and T, μ_s' and μ_a can be determined. Thus, so far the method is representing a two-parameter technique. To determine the g-value and hence separate μ_s' into g and μ_s, the sphere measurements are combined with a narrow beam measurement (one-parameter technique) to measure the collimated transmittance, see Figure 4.1. From this additional measurement one can derive μ_t, ($\mu_t = \mu_a + \mu_s$), using the Beer-Lambertian law[91,92], Eq. (4.1). The reference measurement for the narrow beam set-up is made using a water-filled cuvette replacing the sample. Figure 4.5, shows the schematics of an integrating sphere set-up.

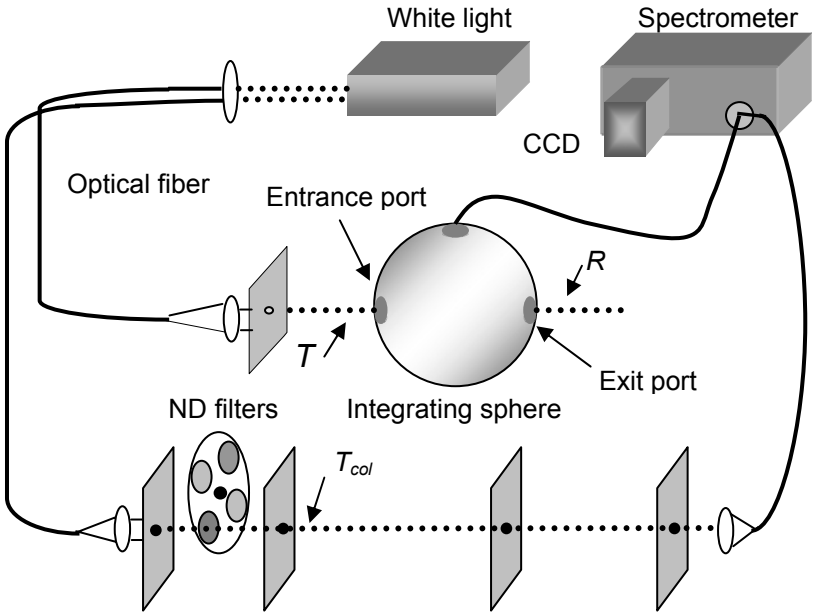

Figure 4.5 *The schematic set-up of an integrating sphere system. Sample is placed at positions indicated by T, R, and T_{col} for measurements. Neutral density filters are used to attenuate the reference signal in the collimated beam par (modified from Ref[93]).*

There is a slightly modified version of this system, containing two spheres, called double-integrating sphere system. Two integrating spheres placed so that the exit port of one and the entry port of the other are adjacent, with only a sample intervening; will allow the simultaneous determination of the reflectance and transmittance of the sample. A sample in between the spheres is illuminated with a collimated beam; and the reflectance is measured in the first sphere, the diffusely transmitted light is measured in the second sphere and the collimated transmission is measured at some distance from the sample through a hole in the second sphere[94].

While the measurements with double integrating spheres are simplified as compared to the single sphere setup, the analysis becomes more complex. This is due to the exchange of light between the spheres, an effect that one has to compensate for in the analysis. Thus the measured signal is always greater than or equal to that for the single sphere, and the increase of the signal depends on both the reflection and transmission properties of the sample [89].

Analysis of the optical properties from the three measured parameters, R, T, and μ_t, can be performed by an iterative algorithm, based on forward adding-doubling and/or Monte Carlo based methods, discussed in Chapter 3. Both these models have their own advantages and disadvantages. Adding-doubling provides quick computations, but it may provide imprecise values due to lateral losses of light caused by the finite size of the sample and/or integrating sphere ports, which cannot be modelled. These losses lead to an underestimation of R and T compared with the ideal case, which in turn lead to overestimation of the absorption coefficient of the sample[55,95,96].

These lateral losses can easily be incorporated in the Monte Carlo method. Normally Monte Carlo simulation-based evaluation requires extensive computation and thus takes a relatively long time. To solve this problem and allow a quick extraction of the optical properties from the measured R and T, a new method, based on a Monte Carlo database and a polynomial regression technique[63], employing Newton-Raphson algorithm, is presented in Paper I, and also is utilized in Papers II and V.

In order to interpret the results in an adequate way, the sources of errors in measurements with integrating sphere system, both for the sphere part and the narrow beam set-up, must be taken into consideration. In total, reflectance or diffuse transmittance cannot be measured perfectly, due to the losses of light at the different ports of the sphere. Results from the reference measurement could be sufficient to compensate for these losses. A problem is, however, that the sample placed at the entrance port (for T measurement), reflects some of the light that has entered the sphere. An improved correction can be introduced in the analysis expression[89,97]so that Eq. (4.3) can be rewritten as:

$$T = \frac{I_T}{I_{ref}} \frac{(1-\varepsilon_s)R_w\{1-[(1-\varepsilon_s)R_w+\varepsilon_s R]\}}{[(1-\varepsilon_s)R_w+\varepsilon_s R][1-R_w(1-\varepsilon_s)]} \tag{4.4}$$

where ε_s is the ratio between the sample port area and the total sphere area, and R_w is the reflectance of the sphere wall[55]. For a double-integrating system this correction factor is more important to incorporate the cross talk between the spheres in the analysis.

Another source of errors may be losses of light due to the size of the sample used for sphere measurements. The sample must cover the entire port of the sphere, and also a large port/beam diameter ratio is necessary to avoid overestimated absorption for samples with low absorption[95,96]. Moreover, Monte Carlo computations incorporating lateral boundary conditions reveals that too small samples can decrease the accuracy of the sphere measurements[15], leading to an overestimation of the absorption coefficient. In fact, measurement with an integrating sphere is very critical for samples with very low absorption coefficient. This limitation constitutes another major weak point of this system. Errors in measurements of R and T directly effect the evaluation of μ_a, so that for small μ_a, even 1% error in the measurements could lead to relative errors of several hundred percent in μ_a[55].

The sphere part of Figure 4.5, is illustrating the arrangement of the integrating sphere system[63,98] used in Papers II, and V. Guiding light along a 600-µm optical fiber from the light source (Xe-lamp), to the sample mounted on the sphere, provides light in a broad spectral region. The light was formed into a ~2 mm parallel light beam using a positive lens with a 10 mm focal length. This resulted in a beam width of a couple of millimetres. This should be compared to the diameter of the entrance and exit ports of the sphere of 2.5 cm. In addition, the samples were prepared with a size of 2.5 x 2.5 cm, entirely covering the entrance and exit ports of the sphere.

As discussed earlier, the purpose of the narrow-beam measurement is to detect the unscattered light passing through the sample. Compared to the sphere measurements, optically thinner samples are used for the collimated measurements. The reason is to avoid as much as possible of the scattered light to be detected. In practice the detected signal is measured as the following,

$$I_{meas} = I_{col} + \varepsilon I_s \tag{4.5}$$

where ε is the fraction of the scattered light that falls inside the collection angle of detection, I_{meas} and I_S refer to the measured and the scattered light, respectively[55].

The error increases linearly with sample thickness and scattering coefficient, quadratically with the collection angle, and is inversely quadratically proportional to (1-g) and the refractive index of the sample[75]. Another problem in narrow beam measurements is the limited dynamic range in the detection. The use of calibrated neutral density filters in the reference measurement brings down the signal level in this measurement to that in sample measurements, and can thus solve this problem.

4.4.2 The combined angular and spatially-resolved head sensor

Integrating sphere measurements are widely used as a reference method for determination of the optical properties of turbid samples[63,99,100]. However, this technique is associated with bulky equipment, complicated measuring techniques, interference compensation techniques, and inconvenient sample handling. A new technique that resembles the integrating sphere method has been presented in Papers I, II, and V. As shown in these Papers, the integrating sphere can be replaced by a new compact device, which is called the Combined Angular and Spatially-resolved Head (CASH) sensor, to measure the optical properties of thin turbid samples in some applications. The CASH sensor is a new compact device, which may prove to be a good alternative to the integrating sphere system. The device designed and constructed in collaboration between Bang & Olufsen Medicom A/S, Denmark and the Department of Physics, Lund University.

This technique is fast and accurate, useful for real-time determination of the absorption coefficient, the scattering coefficient, and the anisotropy factor of thin turbid samples. The technique is based on a simple continuous wave (i.e., steady-state) non-coherent light source. The three optical properties are extracted from recordings of angularly resolved transmittance in addition to spatially resolved diffuse reflectance and transmittance. The data evaluation is based on a multivariate calibration and prediction technique consisting of multiple polynomial regression (MPR)[63]of Monte Carlo produced data followed by a Newton-Raphson[101]algorithm to extract the optical properties. The evaluation is similar to the technique used for the integrating sphere data discussed above. The optical properties can be determined from two to four combined recordings of angularly resolved transmittance, spatially resolved diffuse transmittance, and spatially resolved diffuse reflectance of the sample.

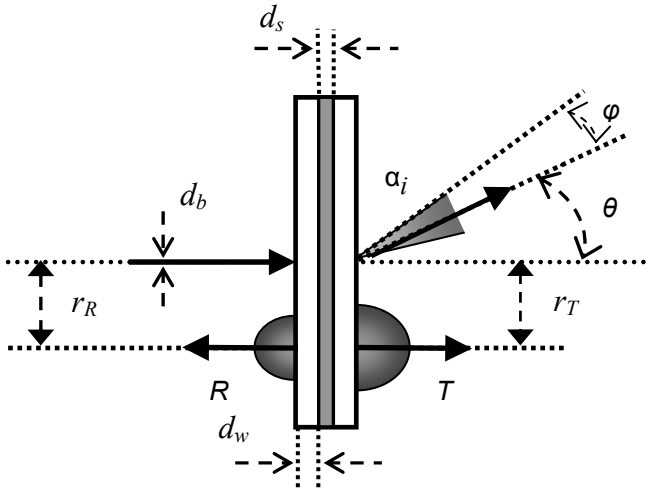

Figure 4.6 *Geometric configuration of CASH sensor developed for measuring μ_a , μ_s , and g . In the figure R and T denotes the spatially resolved diffuse reflectance and transmittance, respectively with radial distance r. The angularly resolved transmittance is denoted α_i , where θ is the deflection angle and φ is the acceptance angle. Finally, d_s is the sample thickness, d_b is the diameter of the collimated source beam, and d_w is the thickness of the cuvette walls.*

The basic geometric configuration of the setup for the analyses used in Paper I, is shown in Figure 4.6. The setup models a cuvette with sample thickness d_s = 1.0 mm, wall thickness d_w = 1.0 mm, and collimated beam diameter d_b = 1.0 mm. The refractive indices of the sample n_s, the wall n_w, and the surrounding media n_m are 1.49, 1.33, and 1.00, respectively. Recordings of the spatially resolved diffuse reflectance and transmittance from the cuvette are denoted as R and T, respectively, whereas various recordings of the angularly resolved transmittance are denoted as α_i, where i = 1, 2, . . . The geometry shown in Figure 4.6 is one alternative to measure four properties, with which we are able to determine the optical properties of the sample. Also other geometrical configurations were evaluated in Paper I. Four such possibilities are schematically shown in Figure 4.7.

In Paper I, a series of MC simulations[57], based on the geometry specified in Figure 4.6 was carried out to investigate the optical property prediction performances of the four configurations shown in Figure 4.7. Thus, in each single MC simulation, R and T were recorded as a function of the radial distance r_T and r_R, respectively, and α_i was recorded as a function of the deflection angle θ and the acceptance angle φ. In each case, r_T and r_R varied within the ranges 0–10 mm in steps of 0.1 mm, whereas θ varied within the range 0°–90° in steps of 0.25°.

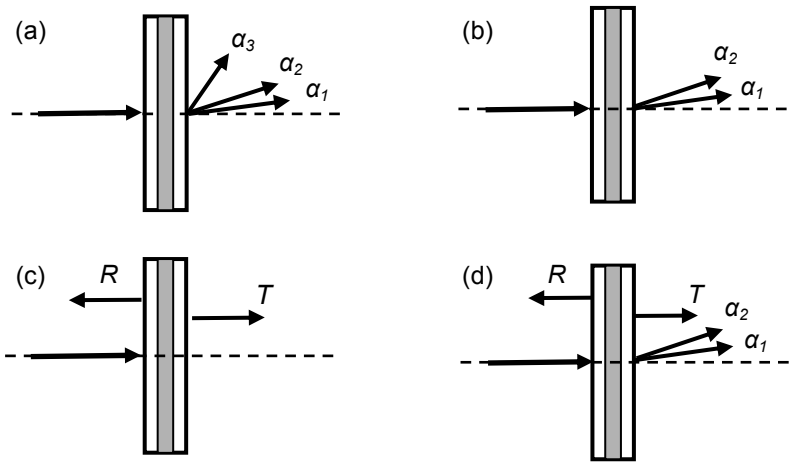

Figure 4.7 *Four different setups used to predict optical properties using various combinations of spatially or angularly resolved data. Each single setup can be used for determination of (a) μ_a, μ_s, and g; (b) μ_s and g; (c) μ_a and μ_s'; (d) μ_a, μ_s, and g. See Figure 4.6 for nomenclature.*

The scored recordings of R, T, and α were obtained and stored in a calibration matrix, i.e., a database containing all combinations of a number of values of μ_a, μ_s, and g within the typical biological ranges[41],

$$0 < \mu_a < 2 \text{ cm}^{-1}$$

$$10 < \mu_s < 200 \text{ cm}^{-1}$$

$$0.85 < g < 0.99 \qquad (4.6)$$

The calibration matrix applied throughout this Paper was generated using 10^6 photon packets in each single case. As presented in Paper I, the numerical test results based on Monte Carlo simulations show mean prediction errors of approximately 0.5 % for all three optical properties within ranges typical for biological media. In addition, to support the presented numerical results, preliminary experiments were performed using measurements on solid epoxy phantoms[102] (see Chapter 3) and milk samples. These experiments were carried out using a laboratory setup based on the geometry shown in Figure 4.7(d). In this case, the thickness of the samples d_s was 1.0 mm; the radial distances r_R and r_T were 2.5 and 2.0 mm, respectively; and the angles α_1 and α_2 were 0° and 5°, respectively. Furthermore, a He–Ne laser (633 nm) with a beam diameter d_b of 1.0 mm was used as a light source. Optical fibers were used to collect the output signals from the setup. These fibers were connected to a set of silicon detectors with matching amplifier electronics mounted in a separate box. This box was connected to a data-acquisition PC board controlled by LabVIEW software. These preliminary experimental results presented exhibited errors of approximately 5 % as compared with the known optical properties of the samples. This demonstrated, in our opinion, a substantial potential of the proposed method for simultaneous absorption and scattering characterization of turbid media.

Such instrumentation is especially interesting because of its obvious advantages compared with integrating-sphere-based methods, e.g., (a) the sample does not have to be moved during the measurements, providing possibilities for true real-time analysis; (b) no bulky spheres are needed; and (c) no technically complicated collimated transmittance measurements are required, and (d) it is quite cost-effective.

4.4.2.1 CASH sensor measurements on brain tissue

Optical measurements of brain tissue have recently attracted much interest, especially for brain activation studies[103-107], and for planning photodynamic therapy (PDT) (see Chapter 7) in the treatment of brain tumors[108-111]. Another area of interest is the assessment of lesion size and site during radio frequency (RF) ablation for the treatment of motor disorders caused, for example, by Parkinson's disease[112]. In Papers II and V, results from optical measurements on normal and coagulated porcine brain tissue are presented using both the CASH sensor and an IS system as a reference system.

The aims of this work were to measure the optical properties of porcine brain tissue before and after coagulating with a monopolar radio frequency electrode and to evaluate whether our newly developed instrument could provide accurate results for real tissue measurements. In this study we focused on measuring the absorption (μ_a) and reduced scattering (μ_s') coefficients, as these measurements can be compared with IS measurements without using the narrow-beam set-up. We limited the evaluation of the optical properties to the spatially resolved diffuse reflectance (R), and angularly resolved diffuse transmittance (α_0), using the set-up that schematically is shown in Figure 4.8.

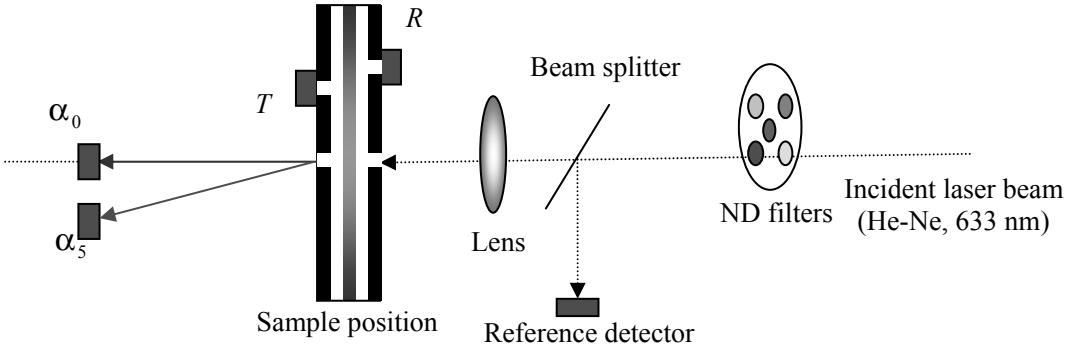

Figure 4.8 *CASH sensor set-up. R, T, α_0 and α_5 denote light referred to as reflectance, transmittance, and angular transmittance at 0˚ and 5˚ to the detectors, respectively. The light is collected by optical fibers. Neutral density (ND) filters were used to increase the dynamic range of the measurements.*

As it is shown in Figure 4.8, a 2 mW HeNe laser (633 nm) with a beam diameter of 1.0 mm was used as a light source. Part of the beam was split off to a reference detector to check that the output from the laser remained constant throughout the measurements. The rest of the light beam was aligned and sufficiently focused to pass through a ϕ=1.0 mm pinhole in a black metal sheet to irradiate the central part of the cuvette. The cuvette was mounted between two black metal sheets. In the centre of the cuvette, transmitted light could escape through a ϕ=1.0 mm hole. Two 400 μm core diameter optical fibers were placed at a distance of 75 mm from the cuvette surface to collect light escaping at two angles of 0^o and 5^o, the signals being denoted α_0 and α_5, respectively. The flat polished ends of two other 400 μm fibers were mounted in holes next to the cuvette at radial distances of 2.5 mm (*R*) and 2.0 mm (*T*). In the measurements performed in Papers II and V, only the α_0 and R signals were used in the subsequent analysis, as in the project, the aim was to extract two coefficients only - μ_a and μ_s'. The optical fibers were terminated on Si detectors controlled by a LabVIEW© PC card. The detectors were used to read the light intensities from each fiber. All signals were recorded simultaneously using an exposure time of 10 ms.

To calibrate both the systems, liquid samples with known optical properties containing a mixture of intralipid-ink and water were prepared in ten groups. Each group contained ten samples with fixed intralipid concentration, providing a constant scattering coefficient, while the concentration of ink was varied in between 0.001 % - 0.1 % to provide ten different absorption coefficients. Likewise, the intralipid concentration was varied between groups within the range 0.4 % - 6.8 % to provide ten different scattering coefficients. In this way a matrix of samples was formed with known optical properties, covering the typical biological range of absorption and scattering coefficients,

$$\begin{aligned} 0.1\ \text{cm}^{-1} \le \mu_a < 10\ \text{cm}^{-1} \\ 5\ \text{cm}^{-1} \le \mu_s' < 85\ \text{cm}^{-1} \end{aligned} \qquad (4.7)$$

Identical cuvettes were made for the measurements, consisting of two glass microscope slides (1 mm thickness) glued with an air gap of 0.3 mm between them. One end was left open so that the liquid sample could be introduced.

The brain tissue samples were obtained from five Swedish native-bred pigs. Five slices of the white matter and five slices of the coagulated samples were prepared with 0.3 mm thickness, placed between two glass plates, and investigated with the optical systems. Small slices were cut to a thickness of 0.3 mm, 2 cm in diameter. The glass slides were marked to ensure that the same part of each sample was irradiated in all the measurements. The optical measurements were performed within 3 h after thawing. During this time the samples were stored at room temperature wrapped in thin plastic film.

For data processing, a multiple polynomial regression (MPR) technique was used, employing fitting of an analytical expression to a discrete number of measured or modelled data points[63]. In this way a simple expression was obtained describing the behaviour of the measured parameters as a function of the optical properties. This provides a fast and accurate method for applications involving real-time, multi-parameter extraction problems. Rapid data processing is of particular importance for spectral recordings including data from a large number of wavelengths. The MPR method was utilized to calibrate and evaluate measurements from both the IS system and the CASH sensor. The calibration process presenting in Papers II and V are slightly different. In Paper II, the prepared intralipid-ink samples with known optical properties, were divided to two parts. One part were used for calibrating the systems and the other part for evaluation of the measured values, Figure 4.9. The evaluated μ_a and μ_s' obtained from each system are shown in Figure 4.10.

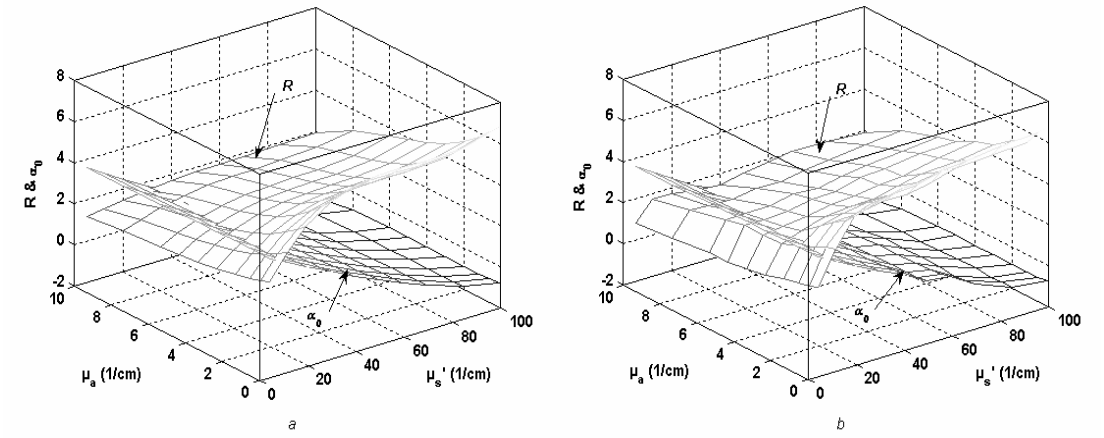

Figure 4.9 *a) Fitted polynomials for R and α_0, and b) measured values of R and α_0.*

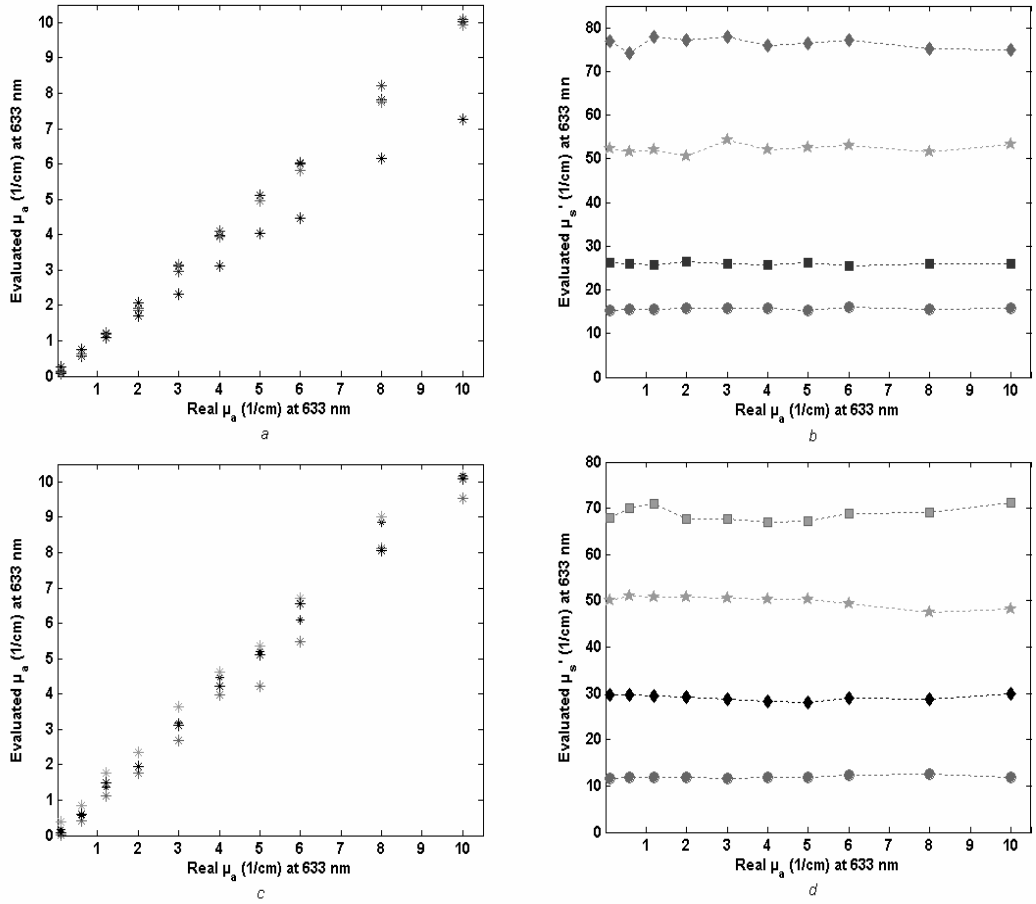

Figure 4.10 *Absorption (μ_a) and reduced scattering coefficient (μ_s') of the intralipid-ink samples measured with the IS and CASH sensor. a) and b) show μ_a and μ_s' measurements with IS; c) and d) show μ_a and μ_s' measurements with the CASH sensor.*

The precision and accuracy of the systems were quantified from these data. The inaccuracy was calculated according to Eq. (4.8), while the spread in data, given as the coefficient of variation (CV), was calculated using Eq. (4.9). The results are presented in Table 4.1.

$$\text{Inaccuracy} = \frac{< \text{x} > - known(\text{x})}{known(\text{x})} \tag{4.8}$$

$$\text{CV} = \frac{\sigma(\text{x})}{< \text{x} >} \tag{4.9}$$

Table 4.1 *Estimated inaccuracy and coefficient of variation of μ_s' and μ_a measurements of intralipid-ink samples, with the IS and CASH sensor.*

Instrument	Inaccuracy (%)		CV (%)	
	μ_a	μ_s'	μ_a	μ_s'
Integrating Sphere	9	5	16	1
CASH sensor	12	1	17	2

For data processing in Paper V, first the IS system was calibrated using a MC simulations. The system was then evaluated with the whole set of intralipid-ink samples. The CASH sensor was subsequently trained by half of the samples, while the other half was used for evaluation. The code provided by Wang and Jacques[56], was used for the Monte Carlo simulations. The R_{tot} and T_{tot} values were simulated for a 38 x 38 matrix of μ_a and μ_s'. The values in these matrices were chosen so that their distributions were wider than their typical biological ranges[41,94]. The anisotropy factor (g) and the refractive index (n) were kept fixed to n = 1.4 and g = 0.9 in the simulations.

The geometry of the sample in the simulation was a semi-infinite slice of 0.3 mm thickness. The samples were placed between two glass slides with a thickness of 1.0 mm and n = 1.5. The beam diameter was set to 2 mm and the acceptance hole of the ports to the integrating sphere to 25 mm. In each simulation, 1 x 10^5 photons were traced. Figure 4.11 shows the simulated functions R_{tot} (μ_a, μ_s') and T_{tot} (μ_a, μ_s') obtained from Monte Carlo simulations for the integrated sphere, and the fitted R_{tot} (μ_a, μ_s') and T_{tot} (μ_a, μ_s') functions using multiple polynomial regression.

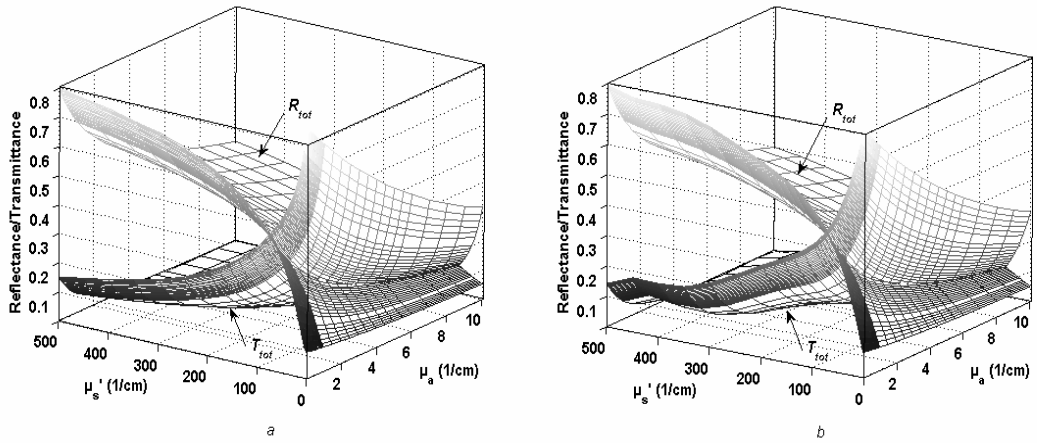

Figure 4.11 *Reflectance and transmittance as a function of the absorption coefficient, μ_a, and the reduced scattering coefficient, μ_s', for a thin slice geometry. R_{tot} and T_{tot} were generated with a) Monte Carlo simulation, b) MPR.*

Table 4.2, shows the inaccuracy and the coefficient of variation (CV) for the evaluated μ_a and μ_s' of the intralipid-ink samples.

Table 4.2 *Estimated inaccuracy and coefficient of variation of μ_s' and μ_a measurements of intralipid-ink samples, with the IS and CASH sensor.*

Instrument	Inaccuracy (%)		CV (%)	
	μ_a	μ_s'	μ_a	μ_s'
Integrating Sphere	9	7	10	3
CASH sensor	12	1	17	2

After completing the evaluation of the systems, measurements on brain tissue samples from pigs were performed. Figure 4.12, shows the IS measurement results for these samples. Both absorption and scattering exhibit considerable variations in spectral shape between the two kinds of samples (normal white matter and coagulated tissue). Also, a cross talk between the absorption and scattering is clearly visible in some of the scattering spectra in the wavelength regions of the haemoglobin peaks (the scattering spectra are not supposed to exhibit any structures in these wavelength regions). The influence of this cross talk falls, however, within the limits of measured accuracy of the technique.

As the CASH sensor measures the light scattered from a considerably smaller volume, measurements could be performed on smaller, visually more homogeneous, regions of the samples, and several measurements could be performed at different positions in the same sample. The CASH sensor provided very reproducible results, and results from different measurements on the same sample but at slightly different positions gave a CV of 8 % for μ_s' and 15 % for μ_a in normal white matter; and 4 % for μ_s' and 17 % for μ_a in coagulated brain tissue. All measurements on a single sample with the CASH sensor were recorded from visually similar tissue. The variations in μ_s' are thus much higher than for the variations in homogenous intralipid-ink samples, while the variations in μ_a already are quite high in these samples, and no difference could be observed for the brain samples. Results for absorption and scattering at 633 nm are presented in Papers II and V.

In general, the results compare very well with data obtained with an integrating sphere for well-defined samples. The instrument is shown to be accurate to within 12 % for μ_a and 1 % for μ_s' in measurements of intralipid-ink samples. The corresponding variations of data were 17 % and 2 %, respectively. The reduced scattering coefficient for porcine white matter is measured to be 100 cm^{-1} at 633 nm, while the value for coagulated brain tissue is 65 cm^{-1}. The corresponding absorption coefficients are 2 and 3 cm^{-1}, respectively. The measured optical properties for the pig brain tissues were compared with the previous measurements, performed by Yaroslavsky *et al.*[113], on human brain tissue.

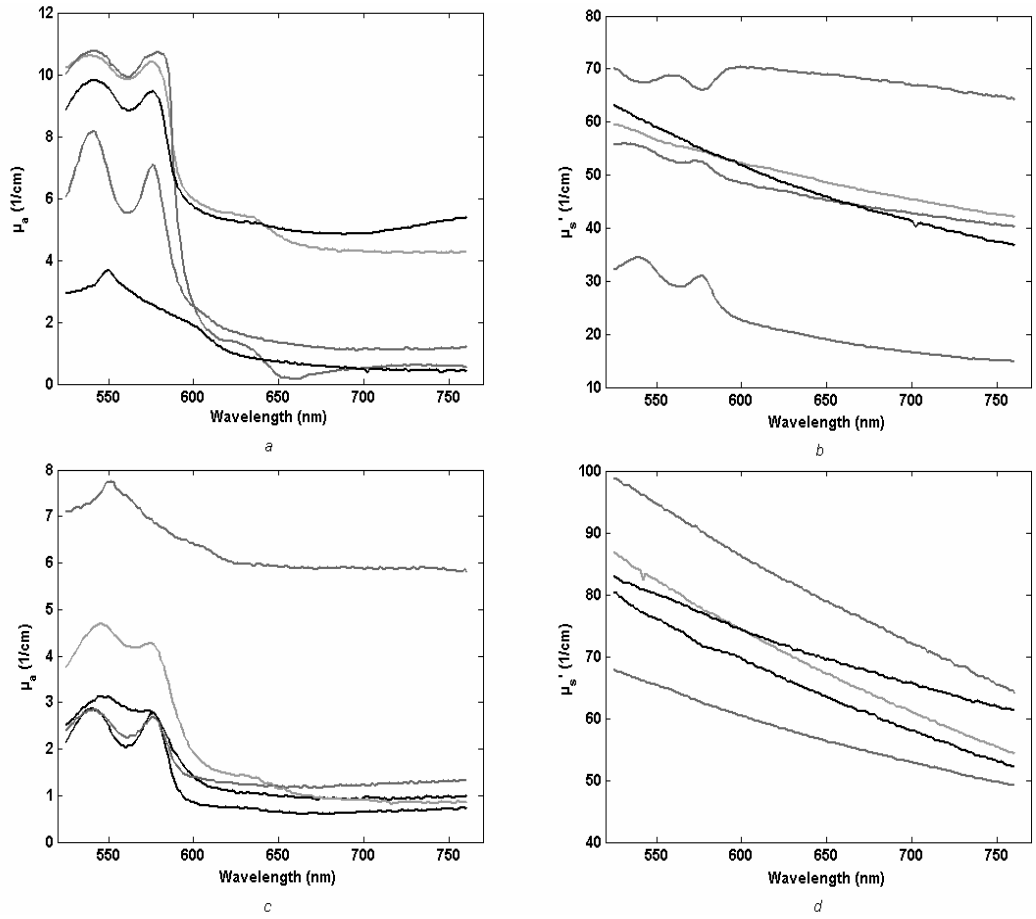

Figure 4.12 *Evaluated spectra from porcine brain samples from five animals measured with the integrating sphere set-up. a) μ_a and b) μ_s' measurements of coagulated tissue; c) μ_a and d) μ_s' measurements of white matter.*

It must be mentioned that for the measurements of brain tissue, the same intralipid-ink training set was used. A small error is then introduced, as the g-factor is expected to be different for brain samples. In a previous study, it was shown that a variation of "g" between 0.8 and 0.99 resulted in a ±2.5 % error in evaluated reduced scattering coefficient[63]. We thus believe that the effect of an assumed error in the g-factor used in the training set in the presented study could be neglected. It is also interesting to note that both systems yielded a better accuracy and lower CV for the reduced scattering as compared to the absorption coefficient. This is probably due to the small sampling distance of the light within the tissue, resulting in a low probability of absorption. It is therefore difficult to evaluate the absorption property with high precision. This has been discussed in the past[102].

The variations observed from the tissue measurements are thus not believed to be due to noise in the measurements, but rather due to true variations between the samples. This is also suggested by the low observed variations within the same sample. Besides, the variation of the results obtained from the IS measurements was higher compare to the CASH sensor measurements. These small scale variations within tissue may complicate

any diagnostic technique based on optical spectroscopy. A probable explanation of these variations is the heterogeneity of brain tissue. In these measurements, it was sometimes difficult to measure white matter or coagulated tissue only, as light was collected out to a distance of 12 mm from the optical axis in the IS set-up. This was sometimes sufficiently large to cover not only the targeted tissue, but also other parts of the samples, meaning the areas not intended to be included in the measurement. It is thus important to conduct local measurements of optical properties, as brain tissue is very heterogeneous. The CASH sensor could be considerably better than the IS in this respect, as the probed volume is smaller. For this sensor, only light at a radius of 2.5 mm is detected. Measurements of neighbouring areas within the same brain tissue sample with this sensor also produced values within 5 % of each other (see Paper V). Interestingly, the optical properties for the coagulated brain tissue varied considerably more than those for the normal white matter. This might be due to regions of white matter intermixed with gray matter inside the coagulated volume. The targeted area for coagulation was always gray matter. Other factors that may cause variations in measured results are slight variations in sample preparation, sample thickness, sample positioning, etc.

4.5 Effects of tissue preparation

The absorption properties *in vivo* depend on both circulation and the oxygen saturation of the tissue. These effects are not presented in *in vitro* measurements, which means that the obtained absorption coefficient do not reflect the *in vivo* situation. The scattering properties are, however, usually relatively unchanged by *in vitro* handling, with exception of fatty tissue if the temperature is allowed to drop to room temperature, which causes crystallization of the fatty acids[55].

It is known that tissue preparation affects the measured optical properties. Mainly the absorption coefficient is believed to alter, due to loss of liquid constituents in tissue. For example it is shown that the effective light attenuation of tissue may change by a factor of two or more in the visible wavelength range where blood is the main absorber[73,114]. Also, the transmission of light through tissue may be altered by freezing and thawing[73]. The structural changes resulting from freezing and the reduction in tissue water content upon thawing, affect the optical response of tissue. A 39 % and 160 % change in transmission of thick sample at 488 and 514 nm, respectively; due to prefreezing has previously been reported[41]. This suggests loss of haemoglobin as a result of the freezing, and the effect is therefore most probably dependent on exactly how the samples are frozen. Also, it has been demonstrated that the optical properties measured from thick samples are generally smaller than those measured from thin samples[115]. These observations suggest that one should be aware of these problems especially in evaluation of the absorption coefficient of tissue from *ex vivo* (*in vitro*) measurements.

Chapter 5

Applications adapted to sampling and analytical chemistry

"The greater danger for most of us
is not that our aim is too high
and we miss it, but that it is
too low and we reach it."

Michelangelo

5.1 Introduction

In order to perform sensitive diagnostic measurements by determining concentration or presence of specific substances, it is often necessary to employ advanced separation and identification techniques. Analytical chemistry provides and introduces many different methods for these purposes. With techniques used in analytical chemistry, a sample can be analyzed quantitatively and qualitatively, but separation and preparation techniques usually must be applied before measuring. Sampling and sample preparation are thus two very important factors affecting the results of the analysis. A method for analysis must be chosen regarding the required accuracy and sensitivity, as well as the type of the sample. In case of medical applications, the methods used for sampling is maybe especially important and delicate. Instead of surveying all different methods for sampling and sample analysis, which is out of the scope of this thesis, only the techniques utilized to measure

drug distribution in connection with Photodynamic Therapy (PDT) are discussed here. PDT, which is a non-invasive technique in cancer diagnostic and therapy, has been discussed in details in Chapter 7. In this chapter, we are interested in exploring the rate of penetration of the photosensitizing agent following topical application. In PDT of skin cancer, a photosensitizing agent, 5-aminolevulenic acid (ALA), and/or its esters is frequently used in a formulation for topical application. This substance is not excited by visible light in itself, and therefore, none of the optical spectroscopic techniques can trace its penetration into the skin. An alternative approach would be to tag the photosensitizing agent and thus be able to detect it. Radio labeling is one such possible approach, although not very appealing as it will involve toxic radioactive substances. Another tagging technique would be to rely on the antigen/antibody method. Neither this method was judged to be very promising, because of naturally existence of ALA in the body. Therefore, it seems the only direct possibility to measure the distribution of ALA in the skin, is to extract it from the skin after application, and hence one problem is how to perform the sampling. The next problem is to find a sensitive method to analyze the concentration of ALA in the collected samples. In this chapter, the studied and the suggested methods for drug sampling and analyzing are discussed.

5.2 Sampling

The intact skin is an organ among other things protecting the body from chemical substances in its local environment. The main barrier in the skin for penetration is the stratum corneum (SC), with about 10-20 μm thickness. This is a layer of densely packed dead cells. If a substance successfully passes this barrier, it is diffusing into the skin until it is reaching the blood vessels. Once inside the blood vessels, the substance will be distributed systemically to almost the entire body. The first challenge in the investigation presented in Paper IV, was to obtain samples from tissues below the stratum corneum. Sampling of the concentration of ALA in the deeper layers of the skin as a function of depth and/or time, would in theory allow both the diffusion and penetration through SC to be determined. For this purpose, a Microdialysis technique was employed.

The main advantages of utilizing a microdialysis technique are the possibilities of collecting as many samples as needed, without depleting the tissue liquid; and the ability to accuracy position the probe. By using the microdialysis technique, the chemistry of the extracellular space in living tissue is monitored. It provides thus no direct measure of the processes inside the cells, but rather what happens outside the cells. It thus provides a local “preview” of high sensitivity of what goes on in the tissue- before any chemical events are reflected in changes of systemic blood levels.

The basic principle of microdialysis is based on mimicking the function of small blood vessel in the tissue. A tubular, semi-permeable dialysis membrane perfused with a physiological solution, is inserted into the skin, and diffusion of molecules from the dermal extracellular space to the perfusate takes place. The perfusate is collected for subsequent analysis[116], see Figure 5.1.

The fact is that this technique is based on an exchange of molecules in both directions. The difference in concentration through the membrane governs the direction of the gradient.

Hence, endogenous and exogenous compounds (such as a drug), are collected simultaneously.

The gradient of a particular compound depends not only on the difference in concentration between the perfusate and the extracellular fluid, but also on the velocity of flow inside the microdialysis probe. The absolute recovery (mol/time unit) of a substance from the tissue depends also on the "cut off" of the dialysis membrane, the length of the membrane, and the diffusion rate of the compound through the extracellular fluid. The reverse holds true for substances entering the tissue from the probe.

The "cut off" of the dialysis membrane is usually defined as the molecular weight in Daltons at which 80% of the molecules are prevented from passing through the membrane[116].

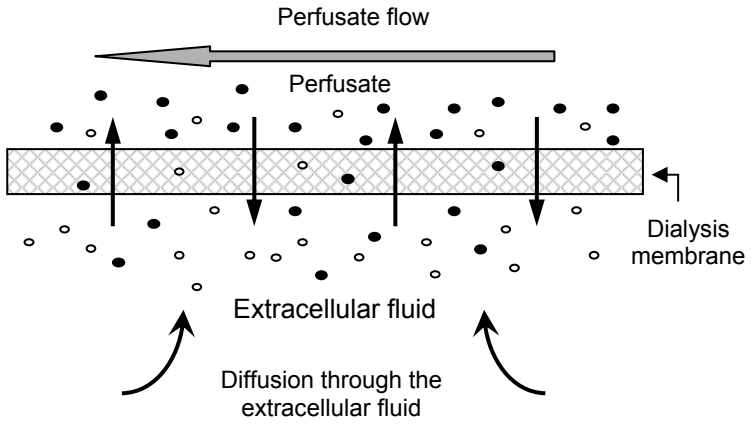

Figure 5.1 *The principle of microdialysis.*

5.3 Analyzing methods

As it was discussed already, in selecting method for analyzing the samples, one need to consider the type and volume of the analyzed sample and the accuracy required. The analysis method can most often be divided in a separation technique to concentrate the sample with regards to the substance of interest, and a detection method.

The two most common detection methods for quantifying ALA in biological fluids are spectrophotometric[117], which often relies on ion-exchange chromatography separation followed by an absorbance detection, and fluorimetric[118-122], which involves derivatization of ALA with a fluorescent label and subsequent analysis by liquid chromatography with fluorescence detection.

The fluorimetric method is more specific and sensitive than the spectrophotometric. However, it tends to overestimate low concentrations of ALA as was demonstrated in a comparative study between the fluorimetric and colorimetric techniques[123]. This limitation is due to the relative nonselectivity of the colorimetric method.

Two less frequently employed derivatization methods for ALA have been published, one based on liquid chromatography (LC) with electrochemical detection[124], and another using gas chromatography (GC) and electron capture detection[125]. Capillary electrophoresis[126] and capillary electrophoresis–mass spectrometric[127] methods were also recently developed to analyze ALA, but, to our knowledge, they have not been applied in clinical settings[128].

In an investigation, two analytical methods, High Performance Liquid Chromatography (HPLC) and Liquid Chromatography Mass Spectroscopy (LC/MS), were used for analyzing the samples provided by microdialysis from normal skin following topical application of Methyl-ALA (M-ALA). The results obtained from each method are presented and discussed in Paper IV. In the followings, both these methods are discussed and explained in more details.

5.3.1 High performance liquid chromatography

The history of the high performance liquid chromatography (HPLC) begins in the 1970's[129]. Chromatography is a broad range of physical methods used to separate and/or to analyze complex mixtures. In general, it can be said that the components to be separated are distributed between two phases: a *stationary phase* bed (solid) and a *mobile phase* (liquid), which percolates through the stationary bed.

For a long time, many different techniques for chemical separation of samples were carried out using relatively simple chromatographic techniques, such as paper chromatography, open-column chromatography, and thin-film chromatography.

However, these chromatographic techniques were inadequate for quantification of compounds and to resolve similar compounds. Later, in about the middle of 1970's, high performance liquid chromatography (HPLC) was developed and quickly improved with the development of column packing materials and the additional convenience of on-line detectors[130,131]. Modern HPLC has many applications including separation, identification, purification, and quantification of various compounds[132]. A HPLC system in general consists of the following parts: mobile phase reservoir, pumps, columns, detectors, injectors, and data system. Figure 5.2 shows the schematics of a HPLC system.

Today, optical detectors are most frequently used in liquid chromatographic systems[133]. These detectors pass a beam of light through the flowing column effluent as it passes through a low volume (~ 10 ml) flowcell. The variations in light intensity caused by UV absorption, fluorescence emission, or change in refractive index (depending on the type of detector used) of the sample components passing through the cell are monitored as changes in a voltage. These voltage changes are plotted versus time to provide retention time and peak area data.

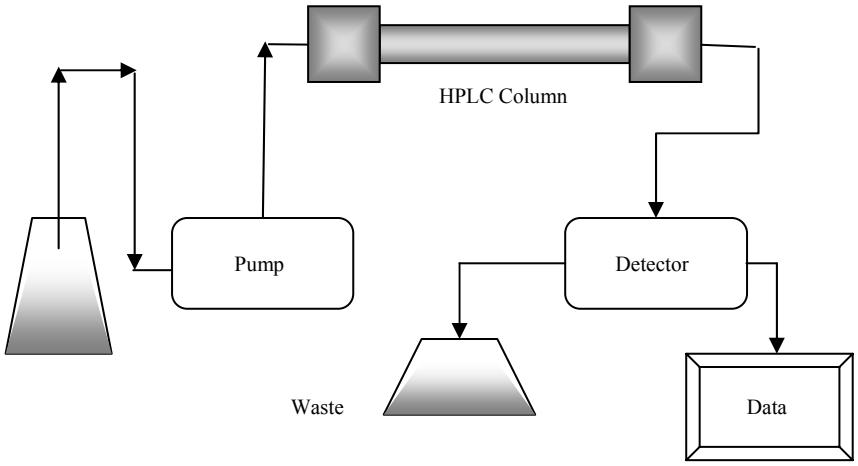

Figure 5.2 *Schematic of a high performance liquid chromatography system.*

The most commonly used detector in liquid chromatography (LC) is the ultraviolet absorption detector [133]. A variable wavelength detector of this type, capable of monitoring from 190 to 460-600 nm, is suitable as a detection unit for a majority of samples. Other detectors in common use include refractive index (RI), fluorescence (FL), electrochemical (EC), and mass-spectrometric (MS). The RI detector is universal but also the least sensitive. The EC detector is quite sensitive (up to 10-15 mole) but also quite selective. The MS detector is the most powerful, as well as the most complicated and expensive one.

The fluorescence detectors are probably the most sensitive among the existing modern HPLC detectors. With such detector, it is possible to detect even a presence of a single analyte molecule in the flow cell. Typically, fluorescence sensitivity is 10 -1000 times higher than that of the UV detector for strong UV absorbing materials. Fluorescence detectors are very specific and thus very selective. This can as mentioned provide a very high sensitivity, as the background signal is virtually non-existent and signal-to-background ratio thus becomes high.

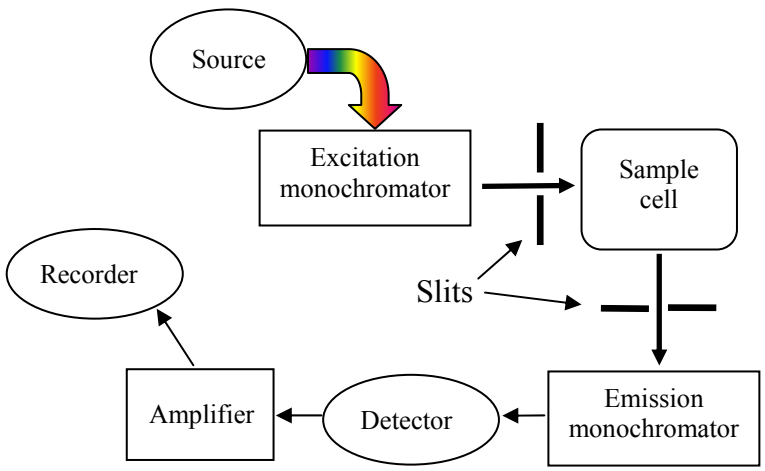

Figure 5.3 *Schematic of the components of a typical fluorescence detector for liquid chromatography.*

If the detection of a HPLC system is based on a fluorescence detector, the technique is called HPLC-Fluorimetry. Figure 5.3, shows an arrangement for a typical fluorescence detector for LC.

5.3.2 Liquid chromatography mass-spectroscopy

In the last decade, there is a significant progress in the development of LC/MS interfacing systems. MS as an on-line HPLC detector is believed to be the most sensitive, selective and in the same time the most universal detector[128].

Mass spectrometry is an analytical method used for measuring the molecular weight (MW) of a sample, and enables the rapid and easy determination of an accurate molecular weight for any given sample. In general, mass spectrometers use the difference in mass-to-charge ratio (m/e) of ionized atoms or molecules to separate them from each other. Mass spectrometry is therefore useful for quantification of atoms or molecules, and for determining chemical and structural information of molecules. Various MS approaches may be used to analyze the components of samples, and this technique is not restricted to particular types of molecules. Each mass spectrometer has three fundamental parts: the ionization source, the analyzer, and the detector, as shown in Figure 5.4.

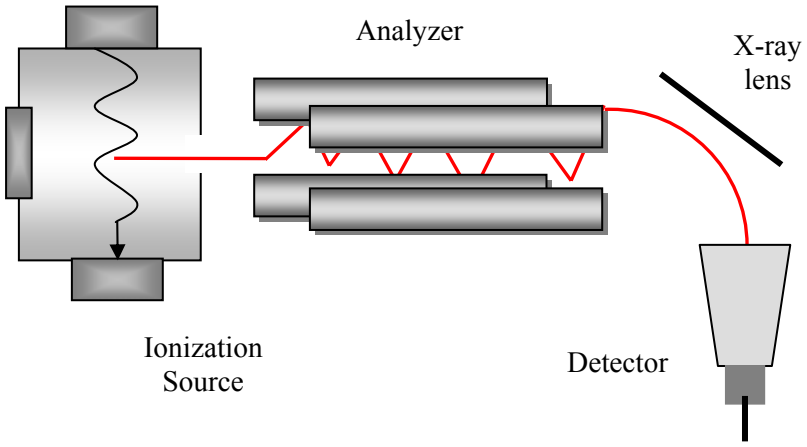

Figure 5.4 *The fundamental parts of a mass spectrometer.*

The first step in mass spectroscopy is to introduce the sample under investigation into the ionization source of the instrument. The method selected to feed the sample into the ionization source often depends on the ionization method being used, as well as the type and complexity of the sample. The sample can be fed directly into the ionization source, or can undergo some type of preparation, like chromatography, on the way to the ionization source. This latter method of sample introduction usually involves the mass spectrometer being coupled directly to a high performance liquid chromatography (HPLC), gas chromatography (GC) or capillary electrophoresis (CE) separation column, and hence the sample is separated into a series of components, which then enter the mass spectrometer consecutively for individual analysis[134,135]. The process of mass spectroscopy is schematically introduced in Figure 5.5.

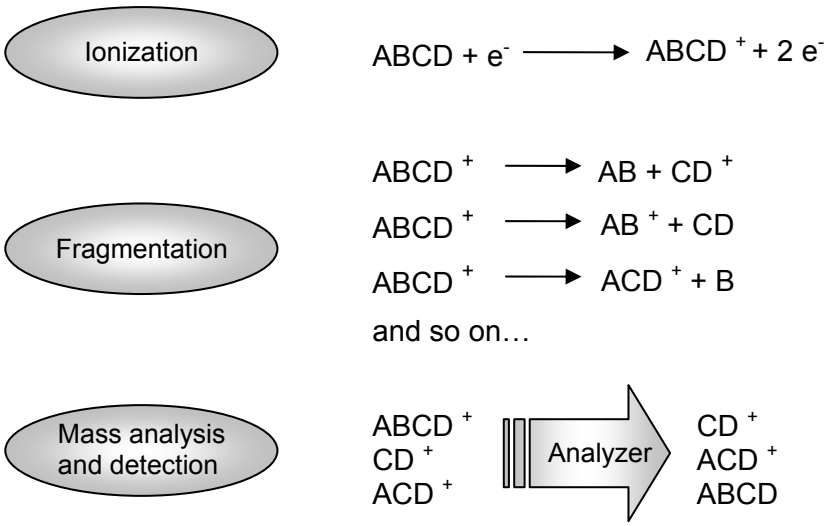

Figure 5.5 *Schematics of MS process.*

Different techniques are used for sample ionization. One of the ionization method used for the majority of biochemical analyses is the Matrix Assisted Laser Desorption Ionization (MALDI). In the investigation performed in Paper IV, a MALDI time of flight (TOF) mass spectroscopy was employed.

To understand how MALDI works; one can follow the below procedures:

1- Sample (A) is mixed with excess matrix (M) and dried on a MALDI plate.

2- Laser flash produces matrix neutrals (M) matrix ions $(MH)^+$, $(M-H)^-$, and sample neutrals (A).

3- Sample molecules are ionized by proton transfer from matrix ions:

$$MH^+ + A \rightarrow M + AH^+$$

4- High voltage is applied to the sample plate accelerating ions out of the ion source.

With the increase in interdisciplinary research in recent years, the need for accurate and sensitive methods for the analysis of biomolecules has been increasingly important for both chemists and biologists. Mass spectrometry has been emerged as an important tool for analyzing and characterizing large biomolecules of varying complexity. The MALDI technique[130], developed in 1987, has increased the upper mass limit for mass spectrometric analyses of biomolecules to over 300,000 D, and has enabled the analyses of large biomolecules by mass spectrometry to become easier and more sensitive. An attractive feature of the time-of-flight (TOF) mass spectrometer is its simple instrumental design (see Figure 5.6). TOF mass spectrometers operate on the principle that when a temporally

and specially well defined group of ions of differing mass/charge (*m/ze*) ratios are subjected to the same applied electric field, they will traverse a certain distance in a time, which depends upon their *m/ze* ratios ($K.E. = [mv^2]/2 = zeEs$, where *K.E.* is the kinetic energy; *m* is the mass of the ion; *v* is the velocity of the ion; *z* is the number of charges of the ion; *e* is the unit charge of an electron; *E* is the electric field; and *s* is the length of the ion source region).

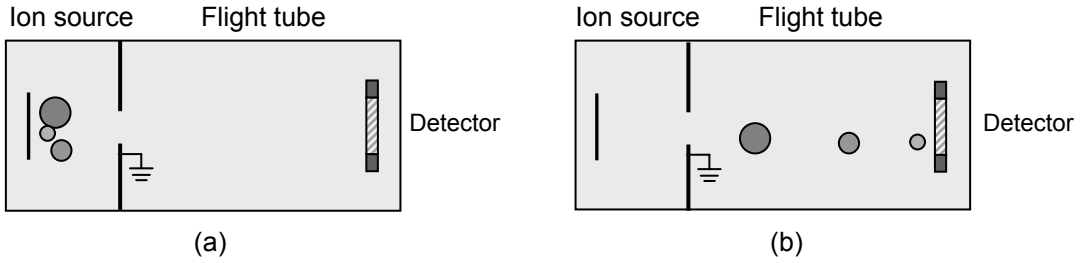

Figure 5.6 *Schematics of TOF mass analyzer. a) Ions are accelerated with the same potential at a fixed point and fixed initial time; b) the lighter ions travel faster and strike the detector, before the heavier ions.*

5.4 Practical applications of Microdialysis, HPLC, and LC-MS

The intention of our research employing the sophisticated analytical chemistry techniques described above, was thus to measure ALA penetration in skin. In a first attempt in the direction of measuring ALA concentration in biological samples, the idea was to convert ALA into a fluorescent molecule that could be more easily detected. The applied method is characterized by the formation of a fluorescent ALA derivative and its subsequent separation by HPLC. For this purpose, a type of Hantzsch reaction was employed. This reaction was first introduced by Okayama *et al*.[136]. Fluorescence derivatization of ALA in this work was slightly based on modified Hantzsch reaction scheme, in which amine compounds react with acetylacetone and formaldehyde[137]. ALA was in this way derivatizated to a fluorescent molecule. The prepared sample was then purified by HPLC. The fluorescence intensity of the eluate was monitored at a wavelength of 370/460 nm (excitation/emission) with a fluorescence monitor. An advantage of this method is the possibility to determine ALA in a small volume of biological materials. The detection limit of ALA in fortified sample was approximately 60 ng/ml (≈353 nmole/lit), which was not considered sufficient for our application.

M-ALA, which is one of the ALA esters, has an application in dermatology for treatment of skin malignancies by PDT. This molecule exhibits better penetration into the skin as compared to ALA, because of its lipophilic nature. It is of interest to study how quickly M-ALA penetrates the skin, as well as the concentration of M-ALA as a function of depth in the skin and time, following topical application (see Paper IV). PDT using ALA and its esters are discussed with more details in Chapter 7.

In another attempt, a fluorescence tag was used to label the M–ALA molecules. In this study, M-ALA cream (METVIX® 20 %, Photo Cure, Oslo, Norway) was applied topically on normal skin. Extracellular fluid samples were obtained from a depth of 500 µm of the forearm skin by a microdialysis system with a 100 KD cut-off membrane. As M-ALA is not a fluorescent molecule, it needed to be specifically labeled with a fluorescent molecule[138] in order to be detected by the HPLC-fluorimetric. For this purpose, M-ALA was coupled to a strong fluorescent molecule (Edman-type fluorogenic reagents). The dye 4-(2´-cyanoisoindonyl) phenylisothiocyanate (CIPIC) used as fluorescent molecule. This was synthesized as has been described by Imakyure[139]. M-ALA in the sample was linked with CIPIC, and separated by HPLC. A fluorimetric monitor was used at the wavelength 260/410 nm (excitation/emission). The detection limit for M-ALA in buffer was shown to be approximately 100 ng/ml.

It was, however, predicted that the concentration of M-ALA in the biological samples obtained by microdialysis was in the range of pg/ml. Therefore, looking for more sensitive technique for analysis, an MS detector was suggested. We thus investigated whether it was possible to analyze M-ALA in the sample without any derivatization by employing the LC/ MS technique. Liquid chromatography was performed on an Agilent 1100 Series, using a 4-µm, 150×2 mm Synergi Polar RP (80 Å) column from Phenomenex. The sensitivity for detection of M-ALA employing MALDI-TOF MS was assessed using a preparation of pure M-ALA in buffer. All MALDI-TOF experiments were performed on a 4700 Proteomics Analyzer (Applied Biosystems, USA). Di-hydroxy benzoic acid (DHB) was used as the MALDI matrix. The signal at 147 D, corresponding to M-ALA, overlapped with a signal from DHB and could thus not be used by itself for detection of M-ALA. Instead, the signal at 147 D was selected for fragmentation analysis with the instrument operated in MS/MS-mode. In the M-ALA samples, a characteristic fragment ion signal at 114 D could be detected and was used for identification of M-ALA. Samples were directly injected to LC without any derivatization. Fractions were collected around the retention time, where M-ALA had shown to be eluted; and then these fractions were subjected to the MALDI-TOF/MS system. However, M-ALA could not be detected from these samples, likely due to co-elution of some unknown substances, interfering with the MALDI sample preparation.

In order to refine the preparation of the samples to obtain more purified samples, microdialysis using a 20 KD cut-off membrane, instead of 100 KD, was utilized. M-ALA cream was applied on normal forearm skin of three volunteers, and samples were collected using Microdialyse every hour and kept in -70 °C until analysis. After separation and purification by HPLC, collected samples in the desired retention time window were vacuumed. For measurement by MALDI-MS, the samples were resuspended in 10 µl water. Then, 0.5 µl of each sample was prepared with 0.5 µl of a matrix solution (DHB).

Samples were analyzed in MSMS-mode, but in none of the samples the fragment ion signal at 114 D, which has been shown to be indicative of M-ALA, could be detected. It seems that the concentration of M-ALA in the sample is still too low for detecting by this method.

In order to further improve the possibilities to detect the diffusion and concentration of ALA derivatives in tissue in connection with PDT, and also to improve the understanding of the optimal timing and application route, a few methods are suggested:

1- Studying the concentration of ALA derivatives in lesions with a reduced barrier of SC. This is more similar to the situation in malignant skin lesions and will yield much higher ALA derivative concentrations in the tissue. 2- Applying other ALA esters, which could be more hydrophobic, that could penetrate through SC of intact normal skin more efficiently. 3- Utilizing an electrophoresis technique, which can increase the penetration of the drug through SC into the skin. 4- Applying tape striping method to overcome the barrier effect of SC, and hence providing the facility of the drug penetration into the skin. 5- Prevention of M-ALA uptake by capillary vessel in dermal area.

Chapter 6

Optical diagnostic techniques

"If you want happiness for a lifetime,
help someone else."

Chinese proverb

6.1 Introduction

Extensive research has been carried out providing non-invasive techniques for tissue diagnostics including delineation and identification of diseased lesions. By help of magnetic resonance imaging and X-ray, it is possible to visualize structures inside the body. A major weak-point of these techniques is, however, that those investigations are normally only offered once a tumor is large enough to cause clinical symtoms[140], and at this relatively late stage the tumor may be difficult to be treated successfully. The main ambition in developing any novel diagnostic technology is to obtain early stage diagnostic capability. All physical disorders are associated with physiological, biochemical and/or morphological changes of tissues. All these alternations can affect the interaction processes between light and tissue from molecular to cellular level[15]. A very frequent term used in optical spectroscopy is "optical biopsy". This means using modifications of the optical signals from light-tissue interaction as spectral fingerprints for tissue characterization. The idea is not to replace normal biopsies, but rather to guide the biopsy collection to the most diseased regions and thereby avoid many unnecessary biopsies. The spectral distribution in all optical diagnostic techniques, depend on the illumination and

collection light geometry. Depending on the type of light interaction with tissue, four main categories of diagnostic techniques are identified: 1- Laser-induced fluorescence (LIF), 2- Raman spectroscopy, 3- Laser-Doppler flowmetry, and 4- Elastic scattering spectroscopy. In all of these techniques, the outcome results depend on the detection geometry. Different angular distributions of the remitted light will, for instance, represent different optical paths inside the tissue and will thus provide different signals. The difference depends on the optical properties of the tissue. Hence, the optical properties of the tissue can be used as a diagnostic parameter. Otherwise, one may want to achieve a detection geometry where all remitted light is collected, which can be done by utilizing an integrating sphere, explained previously. The problem is that this technique is not clinically practical. Instead, a geometry based on optical fibers is suggested. For this reason, in the following, some fluorescence techniques are discussed. You will also find a brief description of optical coherence tomography for tissue diagnostics. This is an imaging modality based on scattered light.

6.2 Laser- induced fluorescence

Laser-induced fluorescence (LIF) is a real-time spectroscopic technique that can be used to characterize biomedical and morphological changes of different kinds of tissue both *in vitro*, and non-invasively *in vivo*[141]. *In vitro* fluorescence measurements are usually recorded from an area of the tissue surface that is large compared with the size of the excitation beam. Most clinical applications of fluorescence spectroscopy require that spectra be recorded remotely via optical fibers. The fluorescence is therefore collected from a relatively smaller area of the tissue surface[142,143]. The sampling depth for measurements of fluorescence is determined by the penetration depth of the excitation light, the various fluorescence coefficient of the tissue layers, and the escape functions for the fluorescence as well as the detection geometry[143].

The fluorophores/chromophores observed in fluorescence spectroscopy of tissue can be divided into two main categories: exogenous and endogenous fluorophores. The endogenous fluorophores include chromophores that naturally exist in tissue, while the exogenous flourophores are obtained by adding tumor marking agents or their precursors, providing a contrast between tumor and normal tissues that can be explored for diagnostic purposes. Examples of the latter type of fluorophores are the ones applied as photosensitizers in photodynamic therapy (PDT), (see Chapter 7). Laser-induced fluorescence can in this respect be a very important tool in PDT for monitoring the level of photosensitizers, and optimizing the treatment.

It is often the shape of the fluorescence spectra that is used for diagnostic purposes, rather than the fluorescence intensity. Changes of the excitation and/or emission spectral between the normal and malignant tissues can thus provide an important tool for tissue diagnostics. This makes the measurement slightly less dependent on the detection geometry and the exact excitation power and detector sensitivity.

6.2.1 Autofluorescence

Fluorescence that is obtained from endogenous tissue fluorophores, without adding any external fluorophore, is called autofluorescence[144]. Alterations in tissue composition between normal to malignant tissue forms a basis for the diagnostic potential for demarcating neoplastic tissue[145]. Tissue fluorophores will normally fluoresce in the visible wavelength range following excitation with radiation in the UV and near-UV region. The auotofluorescence intensity is frequently reduced from tumor tissue as compared to the surrounding normal tissue[146-148]. The endogenous tissue fluoropores can be divided into two main groups, one group involve in the cellular energy metabolism, and the other one in the structural proteins[149]. The most important tissue fluorophores are collagen, elastin, NADH/NADPH[150,151]. It should be mentioned that all fluorescence spectra recorded from tissue is also influenced by the tissue optical properties, meaning those absorbers, which do not fluoresce, but absorb either the excitation or fluorescent light. These absorbers will affect the overall intensity of the fluorescence spectra, while the shape of the spectra will usually be affected to a lower extent as the absorption coefficient in the visible region is lower than for the excitation light in the violet or near-UV region[151,152].

6.2.1.1 Collagen and elastin

Collagen and elastin are proteins associated with the structural matrix of tissue. There are several different types of collagen with slightly different absorption and fluorescence emission characteristics[33]. They are found in connective tissues, and dominate the autofluorescence when the excitation wavelength is about 337 nm.

6.2.1.2 NADH/NADPH and flavins

Nicotinamid adenine dinucleotide (NADH) is involved in the cell metabolism. NADH is mostly situated in the mitochondria. NADH has its excitation peak at 350 nm and emits at 460 nm. NAD^+ is the oxidized form of the NADH, and does not fluoresce if tissue is excited above 300 nm. As malignant tissues are associated with and increased metabolism, and intense oxygen consumption, the lower level of oxygen and hence reduction of pH-value, affect the alternation level of NADH/NAD^+ and their concentration, and the outcome of the tissue autofluorescence. Therefore, NADH is playing very important role in detecting the early-stage malignancies[13,153].

6.2.1.3 Other fluorophores

Tryptofan is a fluorephore involved in the cellular metabolic pathway. It is an amino acid with maximum excitation/emission rate at 275 nm and 350 nm, respectively. This fluorephore is useful as an indicator for cell metabolism[154]. Other important tissue fluorophores are known as, flavins and flavoproteins, beta-carotene, and porphyrins, which are reviewed in references[9,151,155], see also in table 1.

Table6.1 *Some of the most important fluorophores in tissue.*

Endogenous fluorophor	λ_{exc} (nm)	λ_{em} (nm)	Type
Tryptophan	275	350	Metabolic
Collagen	325,333, 370	380,400,460	Structural
Beta-caroten		520	
Elastin	420,460,360,425	500,540,410,490	Structural
Keratin	370	460	Structural
Porphyrin	400	610, 675	Metabolic
Flavins	450	512,525	Metabolic

6.2.2 Fluorescent tumor markers

In order to increase the potential of diagnostics by fluorescence, exogenous fluorescent tumor markers are sometimes utilized. The externally applied fluorescent substances are tumor selective, and can be administrated topically, orally, or intravenously. These markers are often selected to have fluorescence emission in the red and near infrared wavelength region and can thereby be distinguished from the blue-green autofluorescence emission. Hematoporphyrin derivatives are well-known tumor markers and as discussed above, these substances are also utilized as photosensitizer for PDT.

Protoporphyrin IX (PpIX) that naturally exists in the body is another substance used both as a fluorescent tumor marker and a photosensitizer for PDT. PpIX is one of the intermediate products in haem-cycle. An elevated PpIX concentration can be obtained through the haem-cycle following administration of 5-aminolevulinic acid (ALA). This is widely utilized for PDT. PpIX has also been identified as a fluorescent tumor marker for specific tumor types. The tumor localizing characteristics of ALA-induced PpIX is well documented[156-158]. Excited at 405 nm light, PpIX exhibits a dual-peaked fluorescence emission in the red region, one at approximately 635 nm and the other at about 705 nm. Many investigations have been performed to examine the kinetics of the PpIX build-up following administration of ALA and its derivatives by use of LIF[159,160]. Much lower doses of PpIX (or ALA) are necessary for diagnostic as compared to therapeutic procedures.

Figure 6.1, shows fluorescence emission spectra from some of the mentioned tissue fluorophores following excited with 337 nm light, and a comparison between the fluorescence spectra obtained from a premalignant lesion and the normal surrounding tissue *in vivo* after administration of ALA. The wavelength of the excitation light was 405 nm, the dual emission peak from PpIX are obtained at and 635 nm and 705 nm.

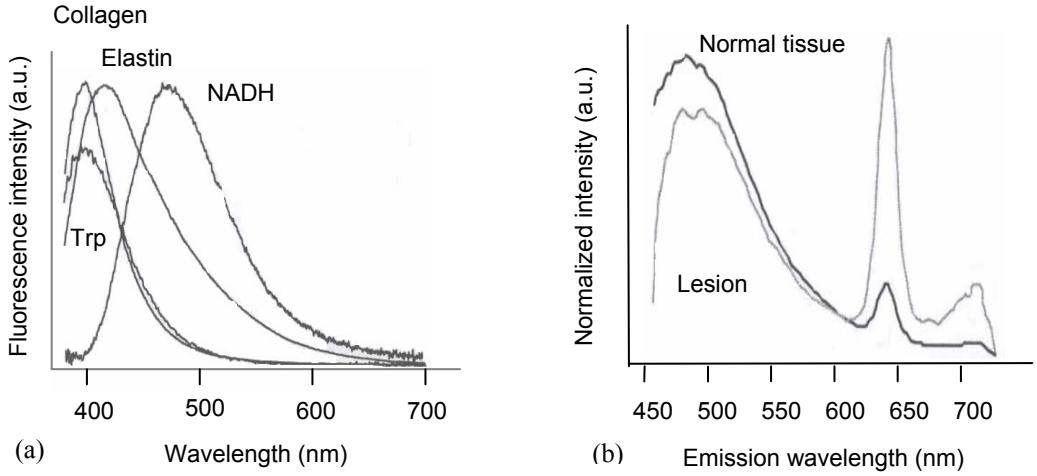

Figure 6.1 *Fluorescence spectra; (a) from some important tissue fluorophores following 337 nm excitation, (b) typical average fluorescence spectra obtained in vivo from normal and premalignant lesion on vocal folds, using 405 nm excitation light where ALA has been applied prior to the examination. Modified from Ref*[161]

6.3 Fluorescence monitoring

In general, LIF method can be divided into point monitoring techniques and imaging methods. The main advantage of using point-monitoring method is the possibility of interstitially application of fluorescence, as in this method optical fibers are used. In this method, the excitation light is guided through an optical fiber probe, and the tissue fluorescence is detected through the same or another fiber. The intensity of the excitation light and the geometry of the sample and fibers will influence the results of the measurements.

On the other hand, the presence of absorbing molecules such as haemoglobin and melanin, which do not fluoresce, is also an important factor that must be taken under consideration in fluorescence diagnostics. The observed fluorescence from biological tissue is often a composite signal and significantly distorted by absorbers and scatterers as compared to fluorescence spectra from pure chromophores. Recorded spectra cannot therefore be interpreted as the intrinsic fluorescence without interference of absorbers and scatterers present in the tissue analyzed[162].

The outcome of the measurement on the same sample alters when a point illumination is used compare to broad illumination geometry. Also, the exact measurement geometry influences the recorded fluorescence emission spectrum. These aspects are demonstrated in the Figure 6.2.

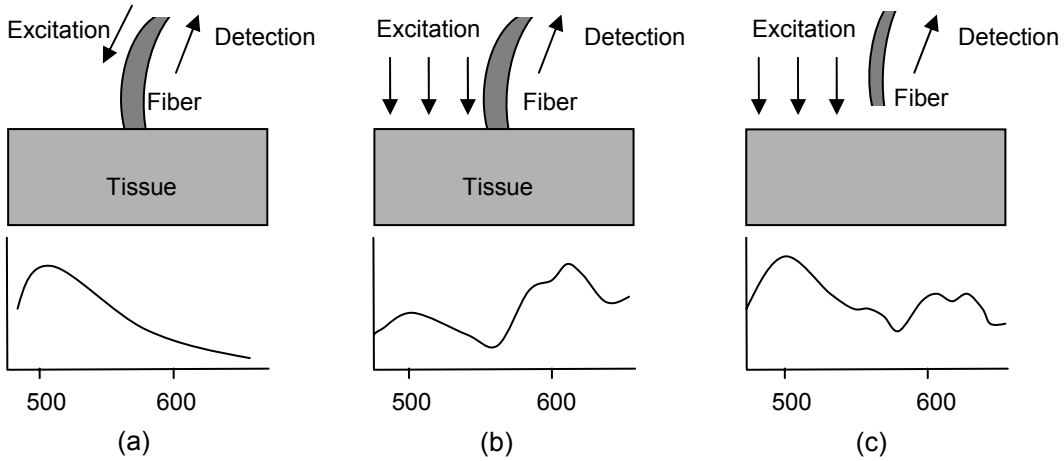

Figure 6.2 *Illustration of the influence of the measurement set-up to the detected fluorescence signal. Modified from Ref*[163].

Another important factor in point monitoring fluorescence spectroscopy is the choice of optical fiber(s). Optimization of quantitative fluorescence spectroscopy devices for medical diagnostics involves specification of a variety of system components including light sources, spectrometers, detectors, and accessories for light delivery and collection. Fiber-optic probes are often used to provide the interface between source and tissue as well as between tissue and detector[164]. Investigations indicate that fiber-optic probe design parameters have strong influence on the relative sensitivity to fluorophore layers in turbid media[165].

In Figure 6.3, two types of fiber-optic probe geometry are compared. Moreover, computational modeling results indicate that the fiber-optic probe design strongly affects light propagation and fluorophore detection. It is known that source and collection fiber size influences the detected fluorescence intensity. Increasing the source and/or detection diameter causes an increase in the attenuation[164]. Regarding the fiber-optic design, other parameters such as illumination-collection fiber separation, and fiber-tissue spacer size, affect the outcome of the measurements, as well as use of single versus multifiber probes[164,166]. In addition, it should be mentioned that longer path lengths and deeper light penetration tend to produce fluorescence spectra which are more strongly altered by hemoglobin absorption[166,167].

The affects of illumination-collection fibers separation, together with the changes of the source power have been investigated in Paper III, where the tissue temperature was monitored by fluorescence of a specially designed fiber probe including a crystal with temperature-dependent fluorescence at the tip. In addition, in this study, the role of scattering coefficient variation on fluorescence intensity was investigated in tissue phantoms.

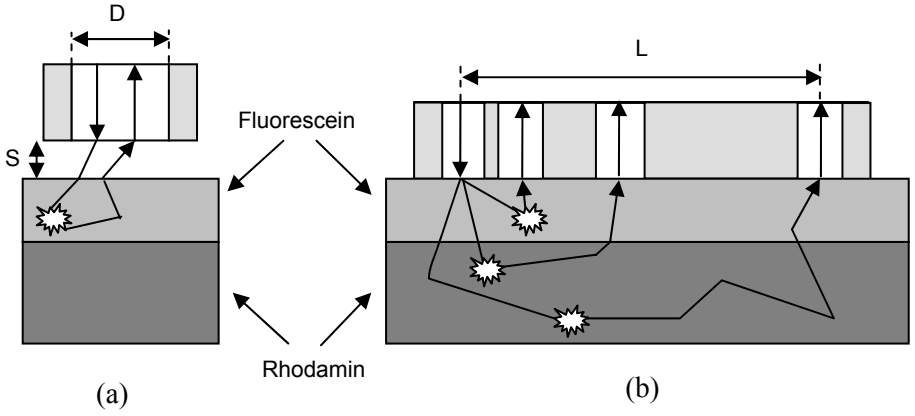

Figure 6.3 *Illustration of fiber-optic probe design parameters and fluorescence light propagation in a two-layer phantom for (a) single probe geometry, and (b) multiple-fiber geometry. The superficial layer and the deeper layer contain Fluorescein and Rhodamine, respectively. S is the probe-sample spacing distance, D is the fiber diameter, and L is the illumination-detection fiber separation distance. Modified from Ref*[165].

6.3.1 Point monitoring systems

Point monitoring measurements are frequently based on a so-called multi-channel analyzer (OMA) system, where a spectrometer and an array detector allow parallel detection of all emission wavelengths. Such systems are often based on the use of optical fibers for guiding the excitation light to the tissue, and the emitted light from the tissue. A complete system is in this way assembled by a spectrometer, a multi-channel detector, a computer, and some optical coupling. These parts will all together make an OMA system. The limitation of this system is that only small area of tissue is probed, and it may thus be difficult to identify the region of interest for such a measurement. For larger area investigations, usually imaging systems are preferred. Another aspect is that the fluorescence light is usually very weak compared to the excitation light. It is therefore necessary to employ a sensitive detector and suppress the background light efficiently. It is important to know that the detected fluorescence spectra are affected not only by the tissue optical properties, but also by the geometry of the measurement (see Figure 6.2).

Using the illumination/detection fibers, and evaluating the spectrum, one should consider that the collected light is dependent on the optical properties of tissue and hence is wavelength dependent, and thus, is dependent on the distance between the illumination and detection fibers, as well as the distance between the tissue surface and the detector fibers. However, it has been shown that in the case of a specific separation of illumination/detection fibers, it is possible to have light detection independent of the scattering properties[15,168]. The influence of the illumination/detection fiber distance on the intensity of the detected fluorescence is a part of the investigation performed in Paper III.

The choice of light source for excitation is another important factor, which must be considered. Using a continuous light source (CW), measurements must be performed in a

dark environment to decrease the effect of any background light present. This is due the low momentary intensity of the illumination light. Instead, by using a pulsed light source with a much higher momentary intensity, together with a gated detector open just during the pulse, one can obtain a sufficient fluorescence signal without being sensitive to the background light[169].

6.3.2 Imaging systems

An imaging system is often preferable to use for investigation on larger areas of clinical relevance, thus avoiding the random sampling. A multicolor fluorescence imaging system, which is used together with endoscope optical fibers, has been developed in Lund. This system uses beam-splitting optics to divide the fluorescence light into four images, which are spatially identical but filtered in separate wavelength bands. The images are detected by an intensified CCD camera. The camera is operated in gated mode to suppress the background light. Computer processing of the images yields a fluorescence image with optimized contrast between normal and diseased tissue. Choosing suitable detection wavelengths and evaluation criteria is important for optimization of the performance of the imaging system.

Another imaging approach is fluorescence lifetime imaging. The fluorescent lifetime of an endogenous fluorophore may be sensitive to local environments, providing specificity for contrast of diseased over normal tissues and optimal detection of disease[170]. By utilizing a gateable image-intensified CCD camera with different delays of the gate with respect to the excitation pulse, it is possible to obtain the lifetime distribution[171].

6.4 Optical coherence tomography

As has been discussed, optical spectroscopy provides essential ways to characterize physical and chemical properties in living tissues and cells and to monitor their functional changes occurring. Thus, optical spectroscopy offers exciting possibilities for developing computed tomography in the optical region, especially in the red and near infrared regions. One can thereby acquire 3D distributions of functional/physiological information. Nevertheless, its development and application in living tissues are complicated by the strong multiple scattering of light[172].

There have been three basic approaches to optical tomography since the early 1980's: optical diffraction tomography (ODT), diffuse optical tomography (DOT), and optical coherence tomography (OCT). Specific advantages of OCT are its high depth resolution, high probing depth in scattering media, contact-free and non-invasive operation, and the possibility to create various function dependent image contrast methods[17].

Penetration depth of OCT is determined by the tissue probed, as well as on the emission wavelength and source power used. There are two coherence properties playing important roles in this technique; the temporal coherence determines the depth resolution, and spatial coherence plays a role in both the lateral and depth resolution[17].

In OCT, light from a source is split into two paths: the sample and reference paths, as in a Michelson interferometer. The light in the sample path interacts with the tissue under investigation, with some light reflected or scattered back from different structure within it. The light in the reference path is reflected back by a mirror to recombine with light returning from the sample path. The beams interfere when the difference between the two paths is within the coherence length of the light source, and the reference path-length is varied to investigate this interference signal for different depths within the sample. The use of a broadband source (hence with short coherence length), enables more precise location of the depth of a structure within the sample than other techniques[173], since interference only occurs when the difference between the lengths of the sample and reference paths is within the coherence length of the light source.

In an investigation, measurements on several human brain tissue samples have been performed using both an OCT system and an integrating sphere system. The concepts and preliminary results obtained with both systems are compared and presented in a Paper, which is not included in this book.

Chapter 7

Photodynamic therapy

"Someone is sitting in the shade today because someone planted a tree a long time ago".

Warren Buffet

7.1 Introduction

One of the most interesting methods in photo treatment, known as *Photodynamic Therapy* (PDT), is discussed in this chapter. PDT is mainly a method to treat superficial and thin tumors, by using a combination of a photosensitizing drug and light to cause selective damage to the target tissue. An adequate concentration of molecular oxygen is also needed for tissue damage. If any one of these components is absent, there is no effect. Moreover, the overall effectiveness requires careful planning of both drug and light dosimetry.

7.2 History

From history, it is seen that light has been employed in the treatment of diseases since a very long time ago[174]. Photosensitizing drugs have been known and applied in medicine for several thousand years. However, the scientific basis for such use, and the concept of

cell death being induced by the interaction of light and chemicals[175], was vague or non-existent before about 1900. The term "photodynamic action", was introduced in 1904 by one of the pioneers of photobiology, Herman von Tappeiner in Munich, Germany, and though it is not clear why he called the process "dynamic", this term is used only for photosensitized reactions requiring oxygen.

7.2.1 Phototherapy

Phototherapy, also called "*Light therapy"*, in definition means the use of light for therapeutic purposes. In phototherapy, the treatment only consists of utilizing light within various wavelength bands and intensities. However, in phototherapy, different mechanisms and photodynamic processes are involved.

Phototherapy, was known by the Egyptians, the Indians and the Chinese, and has been applied since 3000 years ago. The founder of modern phototherapy is Niels Finsen, who got the Nobel Prize (1903), for his work on the use of light from a carbon arc lamp in the treatment of skin tuberculosis[176]. The most widely use of phototherapy is in dermatology[177], for certain types of dermatitis and for psoriasis[24]. In addition, an expanded field of phototherapy, is within psychiatry, where light is used as a therapeutic modality for treating depression, sleep disturbances and seasonal affective disorders (SAD)[24,178].

7.2.2 Photochemotherapy

In one of India's sacred book (1400 BC), it has been written that seeds of the plant *Psoralea corylifolia* can be used for the treatment of vitiligo (an acquired skin disease characterized by patches of unpigmented skin, which often is surrounded by a heavily pigmented border). Psoralens were also known and utilized by Egyptian for treating vitiligo. Psoralens are the photoactive components of these seeds. The chemically enhanced phototherapy, which consists of the administration of a photoactive agent and subsequent irradiation, is called photochemotherapy (PCT). Photochemotherapy in modern age was first reported in 1974, when treatment of psoriasis was performed by using a combination of psoralens and UVA (320-380 nm) radiation. This method, called PUVA therapy, is still used in dermatology, mainly for psoriasis treatment.

7.2.3 Photodynamic therapy

The type of photochemotherapy, which is dependent on the presence of oxygen, is called photodynamic therapy (PDT). The first systematic study of photodynamic action was carried out in Munich in 1897 by a medical student, Oscar Raab under supervision of Hermann von Tappeiner. Tappeiner together with his colleague Jodlbauer, performed a large amount of scientific work on photosensitization, and discovered that oxygen was required for the photodynamic action (1904). For the first time, he used the term of "photodynamic therapy" for this oxygen dependent photodynamic action, and together with a dermatologist (Jesoniek), he was the first who performed PDT on humans for treating skin cancer. They used eosin as a photosensitizer.

Hematoporphyrin and its derivative have been central to the development of PDT. Hausmann was the first to study the biological properties of hematoporphyrin, in 1908. In 1908-1913, a number of photobiological experiments were carried out with hematoporphyrin, demonstrating how it is sensitized by light; while the first studies on sensitization in humans were performed by Meyer-Betz in 1913, who injected himself with hematoporphyrin and remained photosensitized to light for two months. He was sensitized similarly to what is seen today during ALA-PDT. More investigations were performed by Meyer and Fischer on the importance of porphyrin structure for the efficacy of PDT. Fischer's studies on patients suffering from porphyrias, proved the photosensitization of skin due to the accumulation of various porphyrins and their precursors such as δ-aminolevulinic acid and porphyrinogens, in the skin.

The tumor selectivity of porphyrins was observed by Policard in 1924. It was also demonstrated that hematoporphyrin had tumor-localization ability in human malignancies, but later on it was realized that hematoporphyrin was difficult to purify and then the search for pure substances started. In 1948, Figge introduced hematoporphyrin derivative (HPD) as an important substance for cancer detection.

Many clinical and experimental studies regarding the porphyria diseases have been performed over many decades. A characteristic symptom of several of these diseases is skin photosensitivity. This hypersensitivity is related to the accumulation of photosensitizing intermediates produced in the haem synthesis, caused by enzyme disorders. The photosensitizer agent most active in pophyria is protoporphyrin IX (PpIX). The next major step within clinical PDT, was the introduction of δ-aminolevulenic acid (ALA) in the treatment of skin malignancies. Most photosensitizers are large with relatively complex molecular structure. An exception to this is ALA, which is precursor of the photosensitizing compound, PpIX.

The idea of using ALA for PDT was first reported by Malik *et al.* and Moan *et al.* First, Malik *et al.* studied the phototoxic effects of ALA for the killing of erythroleukemic cells *in vitro.* Then ALA-mediated PpIX production in normal skin of mice was reported. Furthurmore, Kennedy and Pottier successfully treated human skin tumors with topically ALA-based PDT[179]. Since then, ALA-PDT has been used in a large number of clinical specialties.

The history of PCT and PDT has been presented in review papers, where references to the above mentioned work can be found[174,177,180,181].

7.3 Principles and mechanisms of photodynamic therapy

The treatment of tumors with PDT includes three major parameters: administration of a photosensitizer that is selectively accumulated in the tumor, subsequent exposure of light, and presence of oxygen in the tumor tissue.

When the photosensitizer molecule absorbs a photon of light with specific wavelength, the molecule will be excited from its stable ground state to its first excited singlet state (S_1).

This absorption band is called the Q-band. The molecule in this state has a short lifetime. From here, the molecule has two possibilities to return to the ground state, either the molecule returns to the ground state by emitting a photon (fluorescence), or by internal conversion with excess energy lost as heat; or the molecule may take the inter-system crossing, and be transferred to the lowest triplet state (T_1) and then to the ground state (S_0); see Figure 2.3.

The triplet state photosensitizer has lower energy than the singlet state, but has a much longer lifetime (typically > 500 ns). This increases the probability of energy transfer to other molecules. The triplet state lifetime influences the probability for the interaction with surrounding molecules. The energy of the excited photosensitizer molecule can then be transferred to molecular oxygen or other molecules by the two reaction mechanisms described below. The photosensitizer is not destroyed in this process, but returns to its ground state without chemical alteration and is able to repeat the process of energy transfer to oxygen many times.

Type I reaction involves electron/hydrogen transfer directly from the excited photosensitizer to another molecule via electron/hydrogen abstraction. In this reaction free radicals are formed. These radicals then react rapidly, usually with oxygen, resulting in the production of highly reactive oxygen species. These react in turn with tissue and causes irreversible damages.

Type II reaction produces the electronically excited and highly reactive state of oxygen known as singlet oxygen. Direct interaction of the excited triplet state photosensitizer with molecular oxygen (which unusually has a triplet ground state) results in the photosensitizer returning to its singlet ground state and the formation of singlet oxygen.

In PDT, it is difficult to distinguish between the two reactions mechanisms. There is probably a contribution of both type I and II processes, indicating the mechanism of damage is dependent on oxygen tension and photosensitizer concentration. The oxygen radicals produced are very reactive, and attack cellular targets. The diffusion distance of singlet oxygen in biological tissue has been estimated in the order of 0.01 μm, corresponding to a lifetime of about 0.01-0.04 μs[50,182]. The PDT mechanism has been summarized in Figure 7.1.

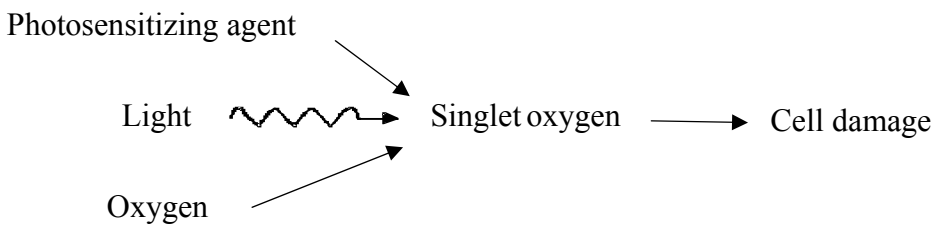

Figure 7.1 *Three essential constituents in photodynamic therapy.*

What is of interest for this thesis is ALA-induced PpIX as a photosensitizer. Accumulation of PpIX in tissues can be achieved by administration of its precursor 5-aminolevulinic acid (ALA), either systemically or topically[183,184]. ALA is a naturally occurring amino acid, which in normal biosynthesis of haem, is produced in mitochondria. After a few enzyme effective conversions, PpIX is formed, which finally is converted into haem by a special enzyme, called ferrochelatase (FeC), that inserts an iron atom into PpIX[184]. Exogenously administered ALA enters the haem biosynthesis pathway, and increases amounts of intermediate porphyrins, as FeC is not able to immediately convert all of the produced PpIX into haem. In this way, PpIX accumulates temporarily in the tissue.

It has been shown that just like haematopophyrin derivative[185,186], the ALA-induced PpIX is selectively accumulated in tumor tissue[187]. In case of systemically application of ALA, the selectivity is mostly explained by altered enzymatic activity in the tumor cells[188,189]. For topical application of ALA in the treatment of dermatological malignancies, the outer barrier of skin, called the stratum corneum (SC), seems to be the factor of major importance for the selectivity. This protective layer has a large impact on the penetration of ALA through the skin[188]. ALA rapidly penetrates through the damaged SC covering a tumor, while the surrounding normal skin tissue with intact SC is less permeable[190,191].

7.4 Light and PDT

Both coherent and incoherent light sources can be used in PDT[192]. Lasers as coherent, monochromatic light sources are widely used because of their advantages over other types of light sources. Using laser light, there is the possibility of obtaining a specific wavelength that can match the absorption band of the photosensitizer used. In this way, exposure to inactive light outside the absorption band of the photosensitizer can be avoided. This light only contributes to generation of heat in the tissue. Also, laser light can more efficiently be coupled into optical fibers, and guided to tissue, *e.g.* for interstitial illumination[24]. Filtered lamps, as incoherent light sources, are also employed in PDT, especially in ALA-PDT of skin lesions[179,191,193]. Small size, simple operation, and low costs, are the major advantages of these types of light sources. They are, however, all limited to superficial illumination, as the light generated is not efficiently coupled into optical fibers. To optimize the treatment response in PDT, it is very important to know the absorption peak of the used photosensitizing agent. Therefore, whatever the choice of light source is, two aims need to be achieved; firstly, the wavelength must match the absorption of the sensitizer to get the desired photochemical reaction, and secondly, the light must be able to penetrate the tissue to the full depth of the tumor extent.

One of the most important limiting factors in PDT, is the light penetration depth. For red light of about 630 nm wavelength, which often is used in PDT, the penetration depth is 2-5 mm, depending on the optical properties of the tissue. Shorter wavelengths have much shorter penetration in tissue. Moan *et al*. showed, however, that light at 410 nm could be used for inactivating cells to a depth of 2 mm in human skin and muscle tissues[194]. The clinical efficacy of PDT from the light delivery point of view, depends on a few parameters such as the fluence rate, total light dose, and the illumination geometry. In general the total light dose used for surface illumination is 60–250 J/cm^2 with an intensity

of 50–150 mW/cm^2 when a laser is used; whereas the dose is 30–540 J/cm^2 with dose rates ranging from 50 to 300 mW/cm^2 when a lamp is used[192]. In each case, one must consider that applying light with high fluence rate increases the risk of oxygen depletion, as oxygen under these conditions is consumed very fast. Such depletion will inhibit the photochemical reaction. In addition, it should also be mentioned, that, due to the high scattering in tissue, the fluence rate in the outermost cell layers, is usually higher than the applied light intensity.

One way for increasing the response to PDT, is to employ light fractionation[195]. This may improve the oxygenation of the illuminated tissue[196,197], and will lead to the generation of more singlet oxygen and enhance the response to the therapy[198]. Another option is the use of long-term fractionation where two light fractions are separated by an interval of 1 hour or longer[199]. After the first light fraction, PpIX may be partially or completely photobleached. New PpIX can then be metabolized during the period until the next irradiation, increasing the effectiveness of the treatment[195].

7.5 Interstitial photodynamic therapy

A major drawback of PDT is that it is limited to thin (<3mm) superficial lesions or lesions accessible through body cavities only. The tumor-eradication depth achievable in surface irradiation is limited to 3–5 mm because of tissue absorption[200]. An alternative for PDT to treat thick lesions or embedded tumors is to utilize optical fibers inserted into the tumor[201]. This method is called interstitial photodynamic therapy (IPDT)[202,203].

An instrument for IPDT has been developed by the company SpectraCure AB (Ideon Research Park, Lund, Sweden). This instrument was used during the studies presented in Paper III. A general schematic drawing of the instrument is shown in Figure 7.2. The instrument uses a maximum of six bare end optical fibres that are used to deliver the therapeutic light into the tumor mass. The same fibers can also be used in order to perform diagnostic measurements during the treatment session[201]. The therapeutic light unit consists of six diode lasers emitting at 635 nm with an individual maximum output power of 200 mW. While in treatment mode, light from the therapeutic light unit is guided into the light distribution module and further coupled into the six 400 μm diameter fibers, which deliver the light to the target tissue.

In the measurement mode, light from the diagnostic light unit is coupled into one of the “patient fibers” via the light distribution module. After interacting with the sample the fluorescence light is collected by the other fibers and coupled into an imaging spectrometer covering the spectral range between 620 and 810 nm. A cut-off filter (Schott RG665) is used to attenuate the intense laser light at 635 nm from the laser light source. Wavelength calibration of the spectrometer is carried out using an HgAr lamp to determine the relation between wavelength and pixel number in the horizontal direction of the CCD chip[201].

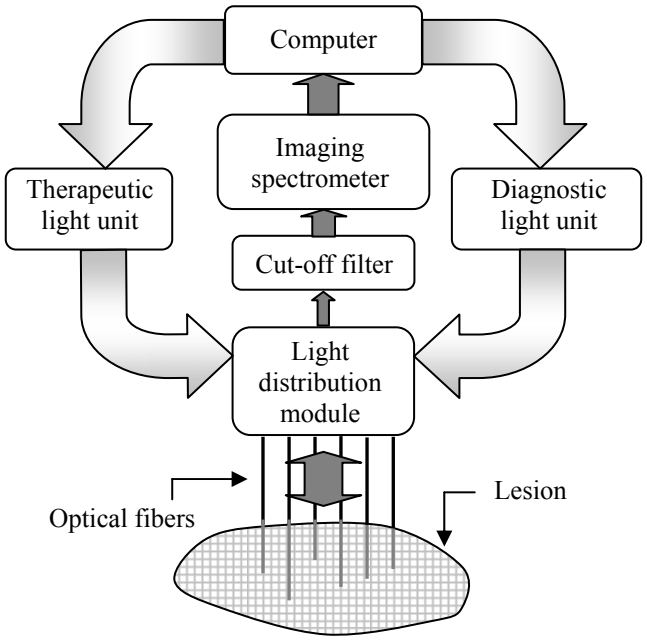

Figure 7.2. *A schematic description of the interstitial photodynamic therapy system. Modified from Ref*[201] .

7.6 Important parameters in PDT

The path of the drug administration, affects the distribution of the photosensitizer. Topical application results in a superficial and local distribution, and is thus suitable for local treatment, with minimal risk of phototoxic reactions in other organs[204]. Systemic drug administration, results in a wide drug distribution that is not limited by the diffusion of the drug, but allows treatment of thicker tumors. The price to pay is a more general photosensitization in other organs. Whatever choice of drug administration, there many be different factors influencing the distribution of the drug, such as skin permeability and drug diffusivity (for topically applications), pH, temperature, photobleaching, enzyme activity, anaesthesia effects, etc. This affects the efficacy of the treatment and must be taken under consideration in the treatment planning. Among all these factors, the diffusivity and temperature effects are the main subjects of investigation in the work described in this thesis, but other parameters of importance for PDT will also briefly be discussed.

7.6.1 Photobleaching

Studies of *in vivo* and *in vitro* laser-induced fluorescence show that the administrated drug is degraded during the PDT procedures, resulting in a decreased drug-related fluorescence. This phenomenon is called photobleaching[24,205,206]. Photobleaching plays an important role in PDT dosimetry. It has been shown that it is possible to take advantage of the bleaching to improve the tumor selectivity of PDT[207]. As the concentration of sensitizer often is larger in tumors than in most surrounding tissues, it is possible to choose sensitizer

concentrations that are so low that normal tissues remain almost undamaged, due to bleaching, while the therapeutic threshold is exceeded in the tumor[174,207].

The understanding is that photobleaching is caused by oxidation of the photosensitizer due to generation of singlet oxygen during the PDT procedures. It has been shown that blue light causes more rapid photobleaching than red light, and that, under illumination with red or blue light, delivery of a fixed light dose at a lower intensity results in more photobleaching[208]. The degree of bleaching depends on the energy absorbed by the photosensitizer[209].

7.6.2 Enzyme dependency of PDT

As already discussed, PpIX is one of the intermediate products in the haem-cycle synthesis, and that ALA is the first step, which initializes the cycle. All the chemical reactions in the cycle, from ALA to PpIX and haem, are enzyme dependent. This shows the importance of enzymatic reaction in ALA-PDT. Moreover, investigations on enzymatic reactions during PDT show that photodynamic inhibition of enzymatic cell detachment may be related to PDT-induced inhibition of tumor metastasis. Therefore, PDT may not only destroy tumor tissues but also reduce the risk for cancer metastases. This is one of the advantages of this cancer treatment method. One of the reasons for this phenomenon may be inhibition of detachment of cancerous cells from the primary tumor[210].

7.6.3 Oxygenation

The effectiveness of PDT is determined by many factors - one of the most important factor being the availability of molecular oxygen in the target tissue during light irradiations[211]. It can be summarized by stating that without oxygen, PDT will have literally no tumor cure effect[212,213]. Tissue oxygenation will change during the course of PDT because of oxygen consumption in the photochemical process, which is a photooxidation process. At high fluence rates of light, the supply rate of oxygen cannot compete with the consumption rate[214,215]. Thus, the oxygen tension will decrease and the haemoglobin/oxyhaemoglobin ratio will increase. At low fluence rates of light, long exposure times are needed, and vessel damage may occur during the light exposure[216,217]. This will also lead to oxygen depletion. Changing the oxygen tension in tissue will also lead to a change in the deoxyhaemoglobin/oxyhaemoglobin ratio and thus the absorption spectrum of tissue[218], altering the light penetration.

7.6.4 pH in PDT efficacy

One of the important factors that influence PpIX formation from ALA is the pH. Maximal PpIX formation is achieved by adjusting the pharmaceutical formulation of ALA or its derivatives to physiological conditions with pH = 7.5 ± 0.5[219]. The activity of enzymes involved in the biosynthetic pathway of haem, have optimal activity in pH between 7 and 7.5. It has been found that PpIX production is more drastically reduced under acidic than

under alkaline condition[219,220]. While the decrease of PpIX formation at higher pH values can be attributed to a reduction of cell viability, the decrease under acidic conditions can be attributed to either a pH-dependent drug uptake or a reduced enzymatic activity in the biosynthesis of haem[219]. It has been shown that tumor selectivity of some photosensitizers such as hematoporphyrin IX (HpIX), which will be more lipophilic at decreasing pH values, is related to the low pH of the extra-cellular fluid[221].

7.6.5 Temperature effects in PDT

Many laser applications in medicine produce heat-inducing alterations of the optical properties of the tissue[222], which is the result of changes in chemical and structural properties. For example, a reduction in the anisotropy factor caused by heat, will result variation in the redistribution of light within the tissue, and in particular, the penetration of the light within the tissue will be reduced[222]. Absorbed optical energy generates heat in the tissue. The heating may act synergistically with PDT[223]. It has been shown, that hyperthermic cell killing (temperature $\geq 44°C$) becomes important for surface irradiance. The role of temperature in IPDT is very important, as well. Presence of a high light fluence rate nearby the source fiber might increase the tissue temperature, and hence affect the treatment results[224]. The available laser power in clinical PDT using surface irradiation generally prevents inadvertent hyperthermia effects, while the power densities are much higher close to the delivering fibers in IPDT[223].

The synergistic cell killing is one reason why the tissue temperature can play an important role in PDT. The tissue temperature will also influence other PDT parameters of importance for the treatment outcome: it may affect on the light distribution in tissue as the optical properties are temperature dependent, and it is also considered as an important factor for drug distribution. It is shown the penetration of ALA into the skin is almost temperature independent, while the following production of PpIX has been found to be a strongly temperature-dependent process. Practically no PpIX is formed in the skin as long as skin temperature is kept low (12-18°C)[225]. Investigations show that the conversion of ALA and its esters into PpIX is temperature-dependent process[226]. PpIX fluorescence detected during the first hour of topical application of drug is 2-3 times higher at normal skin temperature (36-37°C) than at lowered skin temperature (28-32°C)[226]. Another investigation shows that, during topical application of ALA on human skin, the PpIX fluorescence increases about 50% by increasing the temperature from 31°C to 36°C[227]. It has also been shown that a short period of anaesthesia decreased the production of PpIX following topical application of ALA, as the anaesthesia lowers the metabolic activity and decreases the skin temperature[226]. It is often observed that tumors have higher temperature compared with surrounding normal tissues, and this can be one of the reasons that PpIX accumulation in tumors is higher that the surrounding area[188].

Interestingly, an increase in the absorption coefficient of tissue in the range of 60-100%, after PDT has been observed[228]. This might be due to the tissue microcirculation, local hyperthermia, bleeding at the fiber tips, and tissue deoxygenation (because of oxygen consumption during PDT)[201,229,230]; though, the main reasons seem to be the tissue deoxygenation and changes in blood volume during the photosensitizing action[231].

In Paper III, the temperature at the source fibers during IPDT has been monitored both interstitially and superficially. A technique was employed, where an Alexandrite crystal, with temperature dependent fluorescence properties was placed at the fiber tip. Measurements on the skin showed a temperature increased in the range of 2-4°C, which after a short time (3-4 min), became constant. Moreover, measurements on tissue phantoms, yielded similar results as those from superficial skin measurements, although a difference in the level of the temperature increase was observed in the measurements. The absence of blood flow in tissue phantom measurements as compared to the skin can explain this difference.

7.7 Drug distribution in PDT

The pharmacokinetics of fluorescent drugs depends on the type and formulation of the drug, the type of tissue, the method and period of the application and the drug dose. These parameters all determine the optimal time for treatment or diagnostics in PDT[232]. In topically drug administration, the rate of diffusion of the drug is determined by the concentration gradients and by a mainly tissue characterizing parameter, usually referred to as the diffusion constant or diffusivity. The diffusivity is dependent on the properties of the tissue as well as on the chemical properties of the drug molecule[233].

7.7.1 Skin and its permeability

The efficacy of topically applied drugs is often limited by their poor penetration into the skin[234]. The skin is the largest organ of the human body (15-20% of the total body weight), with an area in an adult male of about 2 m^2. The main layers of the skin are the epidermis, the dermis and the subcutis/hypodermis[116]. The dermis contains capillaries, sebaceous and sweat glands, hair follicles and nerves; the epidermis, on the other hand, is the outermost protective layer towards the environment and represents the different stages of cell differentiation. The hypodermis is composed mainly of loose connective tissue and fat cells, serving as an insulation layer and a connecting link to the underlying tissue. Moving outwards from the basal layer of the epidermis, the cells change in an ordered fashion from metabolically active and dividing cells to dense, functionally dead, keratinized cells. These latter cells are surrounded by lipid layers and constitute the outer 10–20 μm of the epidermis, called the stratum corneum (SC). The skin structure is shown in Figure 7.3. The barrier function of mammalian skin is principally attributed to the SC[235]. The barrier properties are based on the specific content and composition of the SC lipids, and in particular, the exceptional structural arrangement of the intercellular lipid matrix and the lipid envelope surrounding the cells[236], which make a ‘brick-and-mortar’ model, as is shown in Figure 7.4.

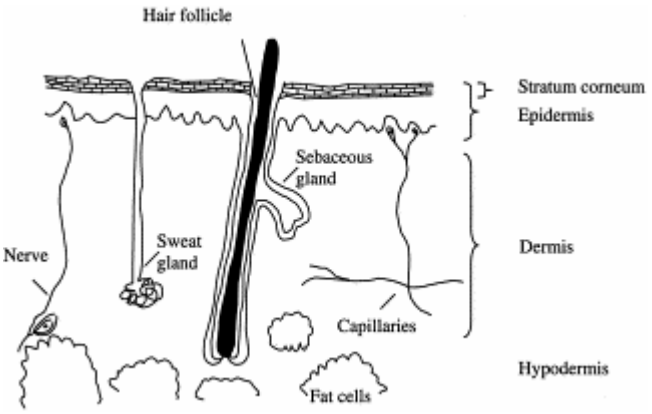

Figure 7.3 *Skin structure, adapted from Ref*[147].

As stated above, drug permeability through the skin is usually limited by the permeability of the SC and also to some extent by the diffusivity of the other skin layers. Two pathways through the intact barrier can be identified: the intercellular lipid and the transcellular routs; that is, in both cases the permeant must penetrate through some of the intercellular lipid matrix[237]. Figure 7.4 schematically illustrates these pathways.

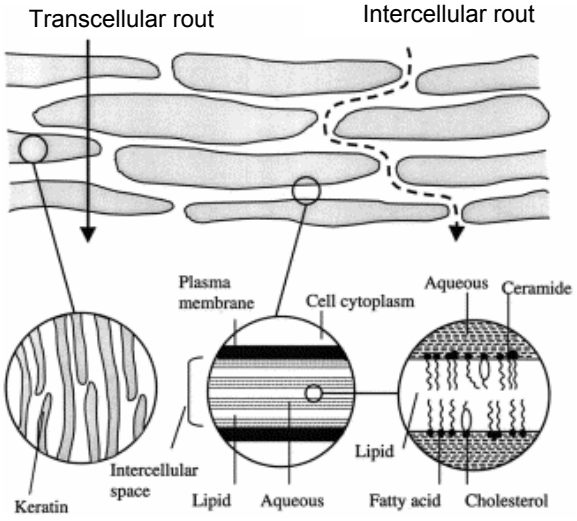

Figure 7.4 *Permeation routes through the stratum corneum, (i) transcellular rout, (ii) intercellular rout.*

The barrier formed by SC is characterized by its permeability. The effect of the barrier on the drug distribution is maximum immediately after application of the drug to the skin, and the relative importance of the barrier decreases with time[238]. Moreover, the permeability can be increased by disordering the SC lipids. Fatty acids are a class of compounds frequently used to increase uptake rates of topically applied drugs, and they are generally believed to increase the permeability across the SC. In topical application of drugs, the drug must not only enter the SC efficiently, but it must also be able to diffuse through the remaining skin layers. Thus, a successful drug has a balanced lipophilicity and possesses some aqueous solubility[239]. A solution to the problem of getting drugs to penetrate the skin might be the use of chemicals that alter the structure and permeation properties of SC in such a way that penetration of drugs through this major barrier is facilated[240]. Another

approach to facilitate the penetration of drugs is removing the SC by tape stripping the skin before drug application[241]. The barrier effect of SC is usually strongly reduced in regions of superficial tumors[238].

7.7.2 ALA and its esters

One limiting factor in PDT with topical drug application is the transport of the drug into the tumor. This can limit the treatment depth more than the penetration of the treatment light. The time required for ALA to diffuse to a depth of 2.5 – 3.0 mm may range from 3 to 15 h[233]. The molecular weight of ALA is 168, and it is a hydrophilic molecule. The hydrophilic nature of ALA restricts drug penetration through the keratinous layer of normal skin (SC); however, this problem may be alleviated by the use of more lipophilic ALA esters. In other words, since the skin penetration of molecules of similar size as ALA increases with increasing lipophilicity, ALA esters, which are more lipophilic than ALA itself, are introduced for PDT of skin tumors. However, SC may bind the esters temporarily, and thereby slow down their penetration into the living cells where PpIX is formed[242]. The pharmacokinetics of ALA and ALA-esters may therefore be relatively different.

It has also been reported that ALA esters need to be hydrolyzed to ALA before they can enter the haem biosynthesis cycle[226]. ALA esters seem to be more selectively producing PpIX in some tumor types than ALA[243]. As more PpIX is formed at higher temperatures, this could be one of the reasons for the tumor selectivity of ALA esters[244]. The PpIX formed from ALA-esters and ALA has been found to be equally efficient in photoinactivation of cells[245].

It is important to understand all the different components of the treatment in detail in order to be able to optimize the treatment result. In PDT the concentration and distribution of the drug is an important dosimetric parameter. Simple mathematical description of PDT components constitutes a dosimetry model. The permeability through SC and the diffusivity in the remaining skin layers of ALA are very important factors, because they determine the distribution and also the concentration of the drug. A dosimetry model, not only provides a mathematical model to describe light and drug distribution, but also opens for possibilities to optimize the treatment. Therefore, the diffusivity or diffusion coefficient is one of many important parameters for PDT. The diffusivity of ALA determines the drug concentration and distribution, and will strongly influence the efficacy of topical ALA-PDT. So far, no records of diffusivity measurements of ALA and/or its esters have been reported.

Considering the fact that at optimal conditions, ALA esters induce higher PpIX concentration at deeper tissue layers[246]; Methyl-ALA (M-ALA) was used for concentration measurements in Paper IV. M-ALA has a wide range of application in dermatology for treatment of cancers by PDT. For this purpose, M-ALA cream (METVIX® 20 %, PhotoCure, Oslo), was used for measuring the drug concentration as a function of time after topical application at a specific depth (500µm) of normal skin *in vivo*, by using a Microdialysis device (see Chapter 5) with 100 KD cut-off membrane. One of the aims of this study was to understand the diffusivity of the M-ALA, which would be

necessary for developing an improved dosimetry model for PDT. Samples were collected during a few hours with a 1 h interval, starting with the application time. The drug was traced in the samples with both High Performance Liquid Chromatography-Flourimetric detection, and Liquid Chromatography Mass Spectroscopy.

HPLC with a fluorimetric detector was not sufficiently sensitive to measure all different concentrations of M-ALA in the samples. The detection limit for M-ALA was in the region of 100 ng/ml and 300 ng/ml in buffer and sample, respectively. In MALDI-TOF MS, the detection limit for M-ALA was lowered to approximately 5 ng/ml.

These measurements show the very low drug concentration in the samples. The concentration of M-ALA was below the detection limit in the samples. Again, the barrier function of the SC was proved. In another attempt, the samples were collected in a purer form by utilizing 20 KD membrane in the microdialysis probe. In spite of a very good optimization, still the concentrations of the drug in the collected samples were below the sensitivity of the used detection techniques. It is planned to repeat these measurements following administration of the drug on tape-stripped skin, to increase the concentration of the drug in the depth beneath the SC, and measure the diffusivity in this condition.

Acknowledgments

"No man is an island".

John Donne

The present work was performed at the Medical Physics Division of the Department of Physics at Lund Institute of Technology, in collaboration with Lund Medical Laser Center, and Department of Physics and Technology at Bergen University, during the period 2002 to 2005.

First of all, I would like to thank my supervisors at Bergen University, Professor Ladislav Kocbach and Professor Jan-Peter Hansen, for motivation, and understanding throughout the years, and for letting me to do the major part of my PhD education in Sweden. Furthermore, my great gratitude is directed towards my supervisor at Lund, Professor Stefan Andersson-Engels, who has supported me constantly and generously shared his knowledge in many ways throughout the course of this work.

I am also very grateful to express my sincere gratitude towards Dr. Katarina Svanberg, and Professor Sune Svanberg, with such good spirits, whose company I have found most stimulating. Also many thanks to Emilie and Kristina Svanberg, for being so nice and kind to me.

I also wish to thank Dr. Chris Anderson, Professor Peter E. Andersen, Dr. Kostadinka Bizheva, and Dr. Lars Thrane, for their collaboration.

Thanks to the former and present fellow students, colleagues and friends in Norway and Sweden, who have made pleasant times and memories during the years of my education: Dr. Csaba and Andrea Anderlik, Dr. Imante Raskinyte, Dr. Giedre Podolyak, Dr. Agnes Nyiri, Dr. Imad Ladadwa, Fadia Jaber, Angela Lazar, Dr. Jeremie Caillat, Dr. Maxim Kartamyshev, Dr. Volodymyr Magas, Suhail Lubbard, Dr. Willy Okullo, Sølve Selstø, Ingrid Sundvor, Dr. Halvor Møll Nilsen, Dr. Morten Førre, Behnaz Saemi, Dr. Marcelo Soto-Thompson, Dr. Jan Sørensen Dam, Dr. Johannes Swartling, Dr. Marica Ericson, Khaled Terike, Daniel Bengtsson, Dr. Sara Pålsson, Dr. Christoffer Abrahamsson, Bastiaan Kruijt, Ilona Kuzmina, Jenny Svensson, and Ann Johansson. In addition, my

special thanks to Linda Persson, Tomas Svensson, and Johan Axelsson, for being such wonderful friends for me.

My special appreciation goes to Arvid Kleppe, the Senior Executive Consultant at the Division of Academic Affairs, University of Bergen, whose supports and kindness are never forgotten.

I would like to express my love and appreciation to my family, although no words can ever declare how much I adore them. My lovely parents, Banoudokht and Ali, who have taught me to rely on God, be strong in life, and never let the difficulties make me give up, and my brothers Babak and Omid, two lovely angels, whose sympathy always bring joy and happiness into my life. Thank you for your love and support, and thank you for what you are.

Finally, I would like to thank my beloved husband, Dr. Hamid Reza Mobini Far, with whom I had so many interesting and valuable discussions throughout the common project we did together. Also, many thanks for being so patient, understanding, and supportive. I do love you!

This work was financially supported by the Norwegian Ministry of Education and Research in cooperation with the Norwegian State Educational Loan Found, and a grant from NorFA. Also generous financial support was achieved from Lund University and the Knut and Alice Wallenberg's Foundation for attending summer schools, conferences, and scientific meetings.

Nazila Yavari
February2006

Summary of papers

In Paper I, a fast and accurate method for real-time determination of the optical properties of thin turbid samples by using simple continuous-wave non-coherent light sources is presented. The applied multivariate calibration and prediction techniques are based on multiple polynomial regressions in combination with a Newton–Raphson algorithm. The numerical test results are based on Monte Carlo simulations. For this purpose, a novel compact instrument, called the **C**ombined **A**ngular and **S**patially Resolved **H**ead sensor (CASH sensor), has been designed and developed, which together with some preliminary results is introduced in the paper.

In Paper II, measurements of the optical properties of porcine brain tissue are presented, using the CASH sensor. These results are compared with the obtained results from an integrating sphere system, and the published data on human brain tissue, as reference.

Paper III, considers that the tissue temperature may increase during the treatment by PDT/IPDT due to absorption of the treatment light. A system to measure the local tissue temperature at the source fibers during IPDT on tissue phantoms and on healthy volunteers is presented.

Paper IV, deals with a method to measure the distribution and rate with which a photosensitizer penetrates skin. This is very important for PDT of skin lesions following topical application of the drug. The diffusion coefficient is the factor used to determine the distribution and concentration of the drug in tissue. Results from measurements on microdialysis samples collected in healthy volunteers following topical application of 5-aminolaevulinic acid methyl ester are presented. These measurements are the first step towards our next goal, being the construction of a dosimetry model for the treatment in PDT.

In Paper V, the optical properties of pig brain tissue have been measured, employing different calibration method, comparing with what is presented in paper II.

References

1. J.S.Dam, Optical analysis of biological media - continuous wave diffuse spectroscopy, Dissertation thesis, Lund Institute of Technology, Lund, Sweden, (2000).

2. B.Williams, *A history of light and lighting*, (2005).

3. C.A.Nowson and C.Margerison, Vitamin D intake and vitamin D status of Australians, *Med. J. Aust.* **177**, 149-152 (2002).

4. A.Vander, J.Sherman and D.Luciano, *Human Physiology - The mechanisms of body functions*, (McGraw-Hill, New York, 1998).

5. R.R.Anderson, and J.A.Parrish, The optics of human skin, *J.Invest.Dermatol.* **77**, 13-19 (1981).

6. H.S.Black, F.R.deGruijl, P.D.Forbes, J.E.Cleaver and H.N.Ananthaswamy, Photocarcinogenesis: an overview, *Photochem. Photobiol.* **40**, 29-47 (1997).

7. R.L.McKenzie, L.O.Björn, A.Bais and M.Ilyasd, Changes in biologically active ultraviolet radiation reaching the Earth's surface, *Photochem. Photobiol.* **2**, 5-15 (2003).

8. S.Madronich, R.L.McKenzie, L.O.Björn and M.M.Caldwell, Changes in biologically active ultraviolet radiation reaching the Earth's surface, *Photochem. Photobiol.* **46**, 5-19 (1998).

9. M.B.Ericson, Spectroscopic measurements and fluorescence imaging for treatment and diagnosis of skin cancer, Dissertation thesis, Department of Experimental Physics, Chalmesr University of Technology and Physics and Engineering Physics, Göteborg University, (2004).

10. A.Vander, J.Sherman and D.Luciano, *Human physiology - The mechanisms of body functions*, (McGraw-Hill, New York, 1998).

11. W.M.Steen, *Laser material processing*, (Springer, 1998).

12. H.I.Pass, Photodynamic therapy in oncology: mechanisms and clinical use [review], *J. Natl. Cancer Inst.* **85**, 443-456 (1993).

13. K.Svanberg, T.Andersson, D.Killander, I.Wang, U.Stenram, S.Andersson-Engels, R.Berg, J.Johansson and S.Svanberg, Photodynamic therapy of non-melanoma malignant tumours of the skin using topical δ-aminolevulinic acid sensitization and laser irradiation, *Br. J. Dermatol.* **130**, 743-751 (1994).

14. I.Wang, N.Bendsoe, C.af Klinteberg, A.M.K.Enejder, S.Andersson-Engels, S.Svanberg and K.Svanberg, Photodynamic therapy versus cryosurgery of basal cell carcinomas; results of a phase III randomized clinical trial, *Br. J. Dermatol.* **144**, 832-840 (2001).

15. A.M.K.Enejder, Light scattering and absorption in tissue - models and measurements, Dissertation thesis, Lund Institute of Technology, Lund, Sweden (1997).

16. S.Brand, J.M.Poneros, B.E.Bouma, G.J.Tearney, C.C.Compton and N.S.Nishioka, Optical coherence tomography in the gastrointestinal tract, *Endoscopy* **32**, 796-803 (2000).

17. A.F.Fercher, W.Drexler, C.K.Hitzenberger and T.Lasser, Optical coherence tomography-principles and applications, *Rep. Progr. Phys.* **66**, 239-303 (2003).

18. C.F.Bohren and D.R.Huffman, *Absorption and scattering of light by small particles*, (John Wiley & Sons, New York, 1983).

19. A.Ishimaru, *Electromagnetic wave propagation, radiation, and scattering*, (Prentice-Hall, Inc., New Jersey, 1991).

20. E.Hecht, *Optics*, (Addison-Wesley, Massachusetts, 1987).

21. T.Johansson, Applications of laser spectroscopy to analytical chemistry, enviromental monitoring and medicine., Dissertation thesis, Lund Institute of Technology, Lund, Sweden, (2002).

22. S.Svanberg, *Atomic and molecular spectroscopy – Basic aspects and practical applications*, (Springer Verlag, Heidelberg, 2004).

23. P.W.Atkins, *Physical chemistry*, (Oxford University Press, Oxford, 1982).

24. I.Wang, Photodynamic therapy and laser-based diagnostic studies of malignant tumours, Dissertation thesis, Lund University, Lund, Sweden (1999).

25. G.Chasteen. The Chemiluminescence Home page, http://www.shsu.edu/~chm_tgc, Sam Houston State University. 1995.

26. S.L.Jacques, L.Wang and A.H.Hielscher, Time-resolved photon propagation in tissues, in *Optical-thermal response of laser-irradiated tissue,* eds. A.J.Welch and M.J.C.van Gemert, pp. 305-332 (Plenum Press, New York, 1995).

27. J.-L.Boulnois, Photophysical processes in recent medical laser developments: a review, *Lasers Med. Sci.* **1**, 47-66 (1986).

28. G.M.Hale and M.R.Querry, Optical constants of water in the 200-nm to 200-µm wavelength region, *Appl. Opt.* **12**, 555-563 (1973).

29. C.R.Nave, Instructional material in physics, http://hyperphysics.phy-astr.gsu.edu/hbase/hframe.html, (2005.

30. F.P.Bolin, L.E.Preuss, R.C.Taylor and R.J.Ference, Refractive index of some mammalian tissue using a fiber optic cladding method, *Appl. Opt.* **28**, 2297-2303 (1989).

31. G.J.Tearney, M.E.Brezinski, J.F.Southern, B.E.Bouma, M.R.Hee and J.G.Fujimoto, Determination of the refractive index of highly scattering human tissue by optical coherence tomography, *Opt. Lett.* **20**, 2258-2260 (1995).

32. B.H.Bransden and C.J.Joachain, *Physics of atoms and molecules*, (1983).

33. S.Pålsson, Methods, instrumentation and mechanisms for optical characterization of tissue and treatment of malignant tumours, Dissertation thesis, Lund Institute of Technology, Lund, Sweden, (2003).

34. J.C.Fisher, Photons, physiatrics, and physicians: a practical guide to understanding laser light interaction with living tissue, part I, *J. Clin. Laser Med. Surg.* **10**, 419-426 (1996).

35. S.L.Jacques, C.A.Alter and S.A.Prahl, Angular dependence of HeNe laser light scattering by human dermis, *Lasers Life Sci.* **1**, 309-333 (1987).

36. M.R.Arnfield, J.Tulip and M.S.McPhee, Optical propagation in tissue with anisotropic scattering, *IEEE Trans. Biomed. Eng.* **35**, 372-381 (1988).

37. M.H.Niemz, *Laser- tissue interactions*, (Springer, 1996).

38. A.J.Welch and M.J.C.van Gemert, *Optical-Thermal Response of Laser-Irradiated Tissue*, (Plenum Press, New York, 1995).

39. S.L.Jacques and S.A.Prahl. Optical properties, Http://omlc.ogi.edu, (1998).

40. L.G.Henyey and J.L.Greenstein, Diffuse radiation in the galaxy, *Astrophys. J.* **93**, 70-83 (1941).

41. W.-F.Cheong, S.A.Prahl and A.J.Welch, A review of the optical properties of biological tissues, *IEEE J. Quant. Electr.* **26**, 2166-2185 (1990).

42. Xiaoyuan D., Xiaosong G. and Min G., Effective Mie scattering of a spherical fractal aggregate and its application in turbid media, *Appl. Opt.* **43**, 2925-2929 (2004).

43. J.Mobley and T.Vo-Dinh, Optical properties of tissue, in *biomedical photonics handbook,* ed. T.Vo-Dinh, pp. 2-1-2-74 (CRC Press, Boca Raton, 2005).

44. S.L.Jacques, Reflectance spectroscopy with optical fiber devices, and transcutaneous bilirubinometers, in *biomedical optical instrumentation and laser-assisted biotechnology,* eds. A.M.Verga Scheggi, S.Martellucci, A.N.Chester and R.Pratesi, pp. 83-94 (Kluwer Academic Publishers, Dordrecht, 1996).

45. J.R.Mourant, J.P.Freyer, A.H.Hielscher, A.A.Eick, D.Shen and T.M.Johnson, Mechanisms of light scattering from biological cells relevant to noninvasive optical-tissue diagnotics, *Appl. Opt.* **37**, 3586-3593 (1998).

46. S.Jacques, Origins of tissue optical properties in the UVA, visible, and NIR Regions, *OSA TOPS on Advances in Optical Imaging and Photon Migration,* vol. **2**, 364-369 (1996).

47. K.M.Case and P.F.Zweifel, *Linear transport theory*, (Addison-Wesley Publishing Co., Reading, MA, 1967).

48. K.M.Case, Elementary solutions of the transport equation and their applications, *Ann. Phys.* **9**, 1-23 (1960).

49. L.V.Wang and S.L.Jacques, Source of error in calculation of optical diffuse reflectance from turbid media using diffusion theory, *Comp. Meth. Prog. Biomed.* **61**, 163-170 (2000).

50. C.Klintenberg, On the use of light for the characterization and treatment of malignant tumours, Dissertation thesis, Lund Institute of Technology, Lund, Sweden, (1999).

51. M.S.Patterson, B.Chance and B.C.Wilson, Time resolved reflectance and transmittance for the non-invasive measurement of optical properties, *Appl. Opt.* **28**, 2331-2336 (1989).

52. T.J.Farrell, M.S.Patterson and B.Wilson, A diffusion theory model of spatially resolved, steady-state diffuse reflectance for noninvasive determination of tissue optical properties *in vivo*, *Med. Phys.* **19**, 879-888 (1992).

53. R.C.Haskell, L.O.Svaasand, T.-T.Tsay, T.-C.Feng, M.S.McAdams and B.J.Tromberg, Boundary conditions for the diffusion equation in radiative transfer, *J. Opt. Soc. Am. A* **11**, 2727-2741 (1994).

54. B.J.Tromberg, L.O.Svaasand, T.-T.Tsay and R.C.Haskell, Properties of photon density waves in multiple-scattering media, *Appl. Opt.* **32**, 607-616 (1993).

55. J.Swartling, Biomedical and atmospheric applications of optical spectroscopy in scattering media, Dissertation thesis, Lund Institute of Technology, Lund, Sweden, (2002).

56. L.Wang and S.L.Jacques, Monte Carlo modeling of light transport in multi-layered tissues in standard C, (Laser Biology Research Laboratory, M. D. Anderson Cancer Center, University of Texas, Houston, Texas, 1992).

57. L.Wang, S.L.Jacques and L.Zheng, MCML - Monte Carlo modeling of light transport in multi-layered tissues, *Computer Methods and Programs in Biomedicine* **47**, 131-146 (1995).

58. X.Lu and P.F.Hus, Reverse Monte Carlo method for transient radiative transfer in participating media, Proc. IMECE, **41932** (2003).

59. S.A.Prahl, M.J.C.van Gemert and A.J.Welch, Determining the optical properties of turbid media by using the adding-doubling method, *Appl. Opt.* **32**, 559-568 (1993).

60. S.A.Prahl, The adding-doubling method, in *Optical-thermal response of laser-irradiated tissue,* eds. A.J.Welch and M.J.C.van Gemert, pp. 101-129 (Plenum Press, New York, 1995).

61. S.A.Prahl. The inverse adding-doubling method, Http://omlc.ogi.edu, 2001.

62. J.Reichmann, Determination of absorption and scattering coefficient for nonhomogeneous media. 1: Theory, *Appl. Opt.* **12**, 1811-1815 (1973).

63. J.S.Dam, T.Dalgaard, P.E.Fabricius and S.Andersson-Engels, Multiple polynomial regression method for determination of biomedical optical properties from integrating sphere measurements, *Appl. Opt.* **39**, 1202-1209 (2000).

64. M.Firbank and D.T.Delpy, A design for a stable and reproducible phantom for use in near infra-red imaging and spectroscopy, *Phys. Med. Biol.,* **38, 847-853** (1993).

65. M.D.Waterworth, B.J.Tarte, A.J.Joblin, T.van Doorn and H.E.Niesler, Optical transmission properties of homogenised milk used as a phantom material in visible wavelength imaging, *Australasian Phys. Eng. Sci. Med.* **18**, 39-44 (1995).

66. T.H.Pham, F.Bevilacqua, T.Spott, J.S.Dam, B.J.Tromberg and S.Andersson-Engels, Quantifying the absorption and reduced scattering coefficients of tissue-like turbid media over a broad spectral range using a non-contact Fourier interferometric, hyperspectral imaging system, *Appl. Opt.* **39**, 6487-6497 (2000).

67. D.D.Royston, R.S.Poston and S.A.Prahl, Optical properties of scattering and absorbing materials used in the development of optical phantoms at 1064 nm, *J. Biomed. Opt.* **1**, 110-116 (1997).

68. S.T.Flock, S.L.Jacques, B.C.Wilson, W.M.Star and M.J.C.van Gemert, Optical properties of Intralipid: A phantom medium for light propagation studies, *Lasers Surg. Med.* **12**, 510-519 (1992).

69. H.J.van Staveren, C.J.M.Moes, J.van Marle, S.A.Prahl and M.J.C.van Gemert, Light scattering in Intralipid-10 % in the wavelength range of 400-1100 nm, *Appl. Opt.* **30**, 4507-4514 (1991).

70. B.C.Wilson, Measurements of tissue optical properties: Methods and theories, in *Optical-thermal response of laser-irradiated tissue,* eds. A.J.Welch and M.J.C.van Gemert, pp. 233-274 (Plenum Press, New York, 1995).

71. M.S.Patterson, B.C.Wilson and D.R.Wyman, The propagation of optical radiation in tissue. II. Optical properties of tissue and resulting fluence distributions., *Lasers Med. Sci.* **6**, 379-390 (1991).

72. B.C.Wilson, M.S.Patterson and S.T.Flock, Indirect versus direct techniques for the measurement of the optical properties of tissues, *Photochem. Photobiol.* **46**, 601-608 (1987).

73. S.T.Flock, B.C.Wilson and M.S.Patterson, Total attenuation coefficients and scattering phase functions of tissues and phantom materials at 633 nm, *Med. Phys.* **14**, 835-841 (1987).

74. R.Marchesini, A.Bertoni, S.Andreola, E.Melloni and A.E.Sichirollo, Extinction and absorption coefficients and scattering phase functions of human tissues *in vitro*, *Appl. Opt.* **28**, 2318-2324 (1989).

75. L.Wang and S.L.Jacques, Error estimation of measuring total interaction coefficients of turbid media using collimated light transmission, *Phys. Med. Biol.* **39**, 2349-2354 (1994).

76. V.G.Peters, D.R.Wyman, M.S.Patterson and G.L.Frank, Optical properties of normal and diseased human breast tissues in the visible and near infrared, *Phys. Med. Biol.* **35**, 1317-1334 (1990).

77. J.Qu, C.MacAulay, S.Lam and B.Palcic, Optical properties of normal and carcinomatous bronchial tissue, *Appl. Opt.* **33**, 7397-7405 (1994).

78. M.G.Nichols, E.L.Hull and T.H.Foster, Design and testing of a white-light, steady-state diffuse reflectance spectrometer for determination of optical properties of highly scattering systems, *Appl. Opt.* **36**, 93-104 (1997).

79. R.L.P.van Veen, W.Verkruysse and H.J.C.M.Sterenborg, Diffuse-reflectance spectroscopy from 500 to 1060 nm by correction for inhomogeneously distributed absorbers, *Opt. Lett.* **27**, 246-248 (2002).

80. A.Kienle, L.Lilge, M.S.Patterson, R.Hibst, R.Steiner and B.C.Wilson, Spatially resolved absolute diffuse reflectance measurements for noninvasive determination of the optical scattering and absorption coefficients of biological tissue, *Appl. Opt.* **35**, 2304-2314 (1996).

81. T.H.Pham, T.Spott, L.O.Svaasand and B.J.Tromberg, Quantifying the properties of two-layer turbid media with frequency-domain diffuse reflectance, *Appl. Opt.* **39**, 4733-4745 (2000).

82. A.Pifferi, P.Taroni, G.Valentini and S.Andersson-Engels, Real-time method for fitting time-resolved reflectance and transmittance measurements with a Monte Carlo model, *Appl. Opt.* **37**, 2774-2780 (1998).

83. A.Kienle and M.S.Patterson, Determination of the optical properties of turbid media from a single Monte Carlo simulation, *Phys. Med. Biol.* **41**, 2221-2227 (1996).

84. S.J.Madsen, B.C.Wilson, M.S.Patterson, Y.D.Park, S.L.Jacques and Y.Hefetz, Experimental tests of a simple diffusion model for the estimation of scattering and absorption coefficients of turbid media from time-resolved diffuse reflectance measure, *Appl. Opt.* **31**, 3509-3517 (1992).

85. R.Cubeddu, M.Musolino, A.Pifferi, P.Taroni and G.Valentini, Time resolved reflectance: a systematic study for the application to the optical characterization of tissue, *IEEE J. Quant. Electr.* **30**, 2421-2430 (1994).

86. K.M.Yoo and R.R.Alfano, Determination of the scattering and absorption lengths from the temporal profile of a backscattered pulse, *Opt. Lett.* **15**, 276-278 (1990).

87. M.S.Patterson, J.D.Moulton, B.C.Wilson, K.W.Berndt and J.R.Lakowicz, Frequency-domain reflectance for the determination of the scattering and absorption properties of tissue, *Appl. Opt.* **30**, 4474-4476 (1991).

88. S.L.Jacques, Principles of phase-resolved optical instruments, in *Future trends in biomedical applications of lasers*, ed. L.O.Svaasand, Proc. SPIE vol. **1525**, 143-153 (1991).

89. J.W.Pickering, C.J.M.Moes, H.J.C.M.Sterenborg, S.A.Prahl and M.J.C.van Gemert, Two integrating sphere with an intervening scattering sample, *J. Opt. Soc. Am.* **9**, 621-631 (1992).

90. N.Yavari, J.S.Dam, J.Antonsson, K.Wårdell and S.Andersson-Engels, In vitro measurements of optical properties of porcine brain using a novel compact device, *Med. Biol. Eng. Comput.* **43**, 658-666 (2005).

91. M.Firbank, M.Hiraoka, M.Essenpreis and D.T.Delpy, Measurement of the optical properties of the skull in the wavelength range 650-950 nm, *Phys. Med. Biol.* **38**, 503-510 (1993).

92. E.Johansson, Measurements of tissue optical properties using an integrating sphere set up, Master's thesis, Lund Institute of Technology, Lund, Sweden (1997).

93. J.Swartling, S.Pålsson, P.Platonov, S.B.Olsson and S.Andersson-Engels, Changes in tissue optical properties due to radio frequency ablation of myocardium, *Med. Biol. Eng. Comput.* **41**, 403-409 (2003).

94. J.F.Beek, P.Blokland, P.Posthumus, M.Aalders, J.W.Pickering, H.J.C.M.Sterenborg and M.J.C.van Gemert, *In vitro* double-integrating-sphere optical properties of tissues between 630 and 1064 nm, *Phys. Med. Biol.* **42**, 2255-2261 (1997).

95. J.H.Torres, A.J.Welch, I.Cilesiz and M.Motamedi, Tissue optical property measurements: Overestimation of absorption coefficient with spectrophotometric techniques, *Lasers Surg. Med.* **14**, 249-257 (1994).

96. G.de Vries, J.F.Beek, G.W.Lucassen and M.J.C.van Gemert, The effect of light losses in double integrating spheres on optical properties estimation, *IEEE Journal of Selected Topics in Quantum Electronics* **5**, 944-947 (1999).

97. K.Grandin and A.Roos, Evaluation of correction factors for transmittance measurements in single-beam integrating sphere, *Appl. Opt.* **33**, 6098-6104 (1994).

98. A.M.K.Nilsson, C.Sturesson, D.L.Liu and S.Andersson-Engels, Changes in spectral shape of tissue optical properties in conjunction with laser-induced thermotherapy, *Appl. Opt.* **37**, 1256-1267 (1998).

99. J.W.Pickering, S.A.Prahl, N.van Wieringen, J.F.Beek, H.J.C.M.Sterenborg and M.J.C.van Gemert, Double-integrating-sphere system for measuring the optical properties of tissue, *Appl. Opt.* **32**, 399-410 (1993).

100. A.N.Yaroslavsky, I.V.Yaroslavsky, T.Goldbach and H.-J.Schwarzmaier, Influence of the scattering phase function approximation on the optical properties of blood determined from the integrating sphere measurements, *J. Biomed. Opt.* **4**, 47-53 (1999).

101. S.V.Chapra and R.P.Canale, *Numerical methods for engineers*, (McGraw-Hill, 1997).

102. J.Swartling, J.S.Dam and S.Andersson-Engels, Comparison of spatially and temporally resolved diffuse-reflectance measurement systems for determination of biomedical optical properties, *Appl. Opt.* **42**, 4612-4620 (2003).

103. D.A.Boas, T.Gaudette, G.Strangman, X.F.Cheng, J.J.A.Marota and J.B.Mandeville, The accuracy of near infrared spectroscopy and imaging during focal changes in cerebral hemodynamics, *Neuroimage* **13**, 76-90 (2001).

104. M.A.Franceschini, J.Thompson, J.P.Culver, G.Strangman and D.A.Boas, Looking for the fast signal: Neuronal and hemodynamic evoked responses of the sensory-motor cortex, in *OSA Biomedical Topical Meetings, OSA Technical Digest*, Proc. Optical Society of America, Washington DC 208-210 (2002).

105. M.Wolf, U.Wolf, J.H.Choi, V.Toronov, L.A.Paunescu, A.Michalos and E.Gratton, Fast cerebral functional signal in the 100-ms range detected in the visual cortex by frequency-domain near-infrared spectrophotometry, *Psychophysiology* **40**, 521-528 (2003).

106. M.L.Schroeter, M.M.Bucheler, K.Muller, K.Uludag, H.Obrig, G.Lohmann, M.Tittgemeyer, A.Villringer and D.Y.von Cramon, Towards a standard analysis for functional near-infrared imaging, *Neuroimage* **21**, 283-290 (2004).

107. K.Wårdell, J.Antonsson and O.Eriksson, Optical measurements during experimental stereotactic neurosurgery, Proc. IFMBE, Ischia, Naples, Italy, (2004).

108. E.H.Moriyama, S.K.Bisland, L.Lilge and B.C.Wilson, Bioluminescence imaging of the response of rat gliosarcoma to ALA-PpIX-mediated photodynamic therapy, *Photochem. Photobiol.* **80**, 242-249 (2004).

109. S.S.Stylli, M.Howes, L.MacGregor, P.Rajendra and A.H.Kaye, Photodynamic therapy of brain tumours: evaluation of porphyrin uptake versus clinical outcome, *J Clin Neurosci.* **11**, 584-596 (2004).

110. M.H.Schmidt, G.A.Meyer, K.W.Reichert, J.Cheng, H.G.Krouwer, K.Ozker and H.T.Whelan, Evaluation of photodynamic therapy near functional brain tissue in patients with recurrent brain tumors, *J. Neurooncol.* **67**, 201-207 (2004).

111. S.A.Friesen, G.O.Hjortland, S.J.Madsen, H.Hirschberg, O.Engebraten, J.M.Nesland and Q.Peng, 5-Aminolevulinic acid-based photodynamic detection and therapy of brain tumors, *In.t J. Oncol.* **21**, 577-582 (2002).

112. J.Antonsson, O.Eriksson and K.Wårdell, In-vivo reflection spectroscopy measurements in pig brain during stereotactic surgery, Proc. SPIE **4958**, 242-250 (2003).

113. A.N.Yaroslavsky, P.C.Schulze, I.V.Yaroslavsky, R.Schober, F.Ulrich and H.J.Schwarzmaier, Optical properties of selected native and coagulated human brain tissues in vitro in the visible and near infrared spectral range, *Phys. Med. Biol.* **47**, 2059-2073 (2002).

114. B.C.Wilson, W.P.Jeeves and D.M.Lowe, In vivo and post mortem measurements of the attenuation spectra of light in mammalian tissues, *Photochem. Photobiol.* **42**, 153-162 (1985).

115. W.-F.Cheong, Summary of optical properties, in *Optical-thermal response of laser-irradiated tissue,* eds. A.J.Welch and M.J.C.van Gemert, pp. 275-303 (Plenum Press, New York, 1995).

116. T.Andersson, Cutaneos microdialysis: A technique for human *in vivo* sampling, Dissertation thesis, Department of Dermatology and Venereology, Linköping University, Linköping, Sweden, (1995).

117. D.Mauzerall and S.Granick, The occurrence and determination of ä-aminolevulinic acid and porphobilinogen in urine, *J. Biol. Chem.* **219**, 435-446 (1956).

118. E.I.Minder, Measurement of 5-aminolaevulinic acid by reversed phase HPLC and fluorescence detection, *Clin. Chim. Acta* **161**, 11-18 (1986).

119. A.Okayama, S.Fujii and R.Miura, Optimized fluorometric determination of urinary delta-aminolevulinic acid by using pre-column derivatization, and identification of the derivative, *Clin. Chem.* **36**, 1494-1497 (1990).

120. Y.Endo, A.Okayama, G.Endo, T.Ueda, N.Nakazono and S.Horiguchi, Improvement of urinary delta-aminolevulinic acid determination by HPLC and fluorescence detection using condensing reaction with acetylacetone and formaldehyde, *J. Ind. Health* **36**, 49-56 (1994).

121. H.Oishi, H.Nomiyama, K.Nomiyama and K.Tomokuni, HPLC determination of δ-aminolevulinic acid (ALA) in the plasma and urine of lead workers: biological indicators of lead exposure, J. Anal. Toxicol. 20, 106-110 (1996).

122. Y.Morita, S.Araki, T.Sakai and Y.Masuyama, Determination of delta-aminolevulinic acid in plasma using high-performance liquid chromatography: a sensitive indicator of lead effects, *J. Ind. Health* **32**, 85-96 (1994).

123. K.Tomokuni, M.Ichiba, Y.Hirai, K.Sugimoto, T.Yoshida and M.Hirata, Comparison between the fluorimetric HPLC method and the conventional method for determining urinary delta-aminolevulinic acid and coporphyrin as indices of lead exposure, *Int. Arch. Occup. Environ. Health* **61**, 153-156 (1988).

124. C.A.Cosata, G.C.Trivelato, M.Demasi and E.J.Bechara, Determination of 5-aminolevulinic acid in blood plasma, tissues and cell cultures by high performance liquid chromatography with electrochemical detection, *J. Chromatogr. B: Biomed. Aci. Appl.* **695**, 245-250 (1997).

125. A.Gorchein, Determination of delta-aminolaevulinic acid in biological fluids by gas–liquid chromatography with electron-capture detection, *Biochem. J.* **219**, 883-889 (1984).

126. A.Bunke, H.Schmid, G.Burmeister, H.P.Merkle and B.Gander, Validation of a capillary electrophoresis method for determination of 5-aminolevulinic acid and degradation products, *J. Chromatogra. A.* **883**, 285-290 (2000).

127. G.A.Lord, J.L.Luo and C.K.Lim, Capillary zone electrophoresis/mass spectrometry of 5-aminolaevulinic acid and porphobilinogen, *Rapid Commun. Mass Spectrom.* **14**, 314-316 (2000).

128. N.M.Felitsyn, G.N.Henderson, M.O.James and P.W.Stacpoole, Liquid chromatography-tandem mass spectrometry method for the simultaneous determination of delta-ALA, tyrosine and creatinine in biological fluids, *Clin. Chim. Acta.* **350**, 219-230 (2004).

129. J.H.Knox and B.Kauer, High Performance Liquid Chromatography, eds. P.R.Brown and R.A.Hartwick, (Wiley Interscience: New York, 1989).

130. K.Benedek, Analytical high-performance liquid chromatography, *Methods Mol. Biol.* **251**, 183-190 (2004).

131. E.Katz, R.Eksteen, P.Schoenmakers and N.Miller, *Handbook of HPLC*, (1998).

132. W.S.Hancock, R.C.Chloupek, J.J.Kirkland and L.R.Snyder, Temperature as a variable in reversed-phase high-performance liquid chromatographic separations of peptide and protein samples. I. Optimizing the separation of a growth hormone tryptic digest., *J. Chromatogr.* **686**, 31-43 (1994).

133. W.W.Christie, *High-Performance Liquid Chromatography and Lipids*, (Pergamon Press, Oxford, 1987).

134. A.L.Yergey, C.G.Edmonds, I.A.S.Lewis and M.L.Vestal, *Liquid chromatography/mass spectrometry: Techniques and applications*, (1990).

135. W.M.A.Niessen and J.Van Der Greef, *Liquid chromatography-mass spectrometry: Principles and applications*, (Marcel Dekker , 1992).

136. A.Okayama, Fluorimetric determination of urinary delta-aminolevulinic acid by high-performance liquid chromatography and post-column derivatization, *J. Chromatogr.* **426**, 365-369 (1988).

137. H.Oishi, H.Nomiyama and K.Nomiyama, Fluorometric HPLC determination of delta-aminolevulinic acid (ALA) in the plasma and urine of lead workers: biological indicators of lead exposure, *J. Antal. Toxicol.* **20**, 106-110 (1996).

138. J.Lu, C.Lau, M.Morizono, K.Ohta and M.Kai, A chemiluminescence reaction between hydrogen peroxid and acetonitrile and its applications, *Anal. Chem.* **73**, 5979-5983 (2001).

139. O.Imakyure, A fluorogenic reagent for amino acid in liquid chromatography,4-(2 -cyanoisoindonyl)phenylisothiocyanate, *Anal. Chim. Acta* **291**, 197-204 (1994).

140. G.A.Wagnières, W.M.Star and B.C.Wilson, *In vivo* fluorescence spectroscopy and imaging for oncological applications, *Photochem. Photobiol.* **68**, 603-632 (1998). Invited review.

141. C.af Klinteberg, A.M.K.Nilsson, I.Wang, S.Andersson-Engels, S.Svanberg and K.Svanberg, Laser-induced fluorescence diagnostics of basal cell carcinomas of the skin following topical ALA application, *Biomed. Opt. Newsletter* **5**, 1-6 (1996).

142. L.I.Deckelbaum, J.K.Lam, H.S.Cabin, K.S.Clubb and M.B.Long, Discrimination of normal and atherosclerotic aorta by laser-induced fluorescence, *Lasers Surg. Med.* **7**, 330-335 (1987).

143. M.Keijzer, R.R.Richards-Kortum, S.L.Jacques and M.S.Feld, Fluorescence spectroscopy of turbid media: Autofluorescence of the human aorta, *Appl. Opt.* **28**, 4286-4292 (1989).

144. S.Andersson-Engels, J.Johansson, K.Svanberg and S.Svanberg, Fluorescence imaging and point measurements of tissue: Applications to the demarcation of malignant tumors and atherosclerotic lesions from normal tissue, *Photochem. Photobiol.* **53**, 807-814 (1991).

145. R.Na, I.M.Stender and H.C.Wulf, Can autofluorescence demarcate basal cell carcinoma from normal skin? A comparison with protoporphyrin IX fluorescence, *Acta Derm. Venereol.* **81**, 246-249 (2001).

146. S.Andersson-Engels, J.Johansson, K.Svanberg and S.Svanberg, Fluorescence diagnosis and photochemical treatment of diseased tissue using lasers: Part I, *Anal. Chem.* **61**, 1367-1373 (1989).

147. S.Andersson-Engels, J.Johansson, U.Stenram, K.Svanberg and S.Svanberg, Diagnosis by means of fluorescent light emission from tissue, Swedish Patent No. 5, 115, 137 (1989).

148. S.Andersson-Engels, J.Johansson, K.Svanberg and S.Svanberg, Fluorescence diagnosis and photochemical treatment of diseased tissue using lasers: Part II, *Anal. Chem.* **62**, 19-27 (1990).

149. R.Richards-Kortum and E.Sevick-Muraca, Quantitative optical spectroscopy for tissue diagnosis, *Annu. Rev. Phys. Chem.* **47**, 555-606 (1996).

150. S.Andersson-Engels, J.Johansson, U.Stenram, K.Svanberg and S.Svanberg, Malignant tumor and atherosclerotic plaque diagnosis using laser-induced fluorescence, *IEEE J. Quant. Electr.* **26**, 2207-2217 (1990).

151. S.Andersson-Engels, L.Baert, R.Berg, M.A.D'Hallewin, J.Johansson, U.Stenram, K.Svanberg and S.Svanberg, Fluorescence characteristics of human atherosclerotic plaque and malignant tumors, in *Optical methods for tumor treatment and early diagnosis: Mechanisms and Techniques*, ed. T.J.Dougherty, Proc. SPIE vol. **1426**, 31-43 (1991).

152. B.Chance, P.Cohen, F.Jöbsis and B.Schoener, Intracellular oxidation-reduction states in vivo, *Science* **137**, 499-508 (1962).

153. R.Rydell, C.Eker, S.Andersson-Engels, P.Wahlberg and K.Svanberg, Fluorescence investigations to identify laryngeal lesions in vivo, Manuscript in preparation for Head and Neck (2002).

154. N.Kollias, G.Zonios and G.N.Stamatas, Fluorescence spectroscopy of skin, *Vibrational Spectroscopy* **28**, 17-23 (2002).

155. A.Mahadevan, M.F.Mitchell, E.Silva, S.Thomsen and R.Richards-Kortum, Study of the fluorescence properties of normal and neoplastic human cervical tissue, *Lasers Surg. Med.* **13**, 647-655 (1993).

156. M.Soto Thompson, T.Johansson, S.Pålsson, S.Andersson-Engels, S.Svanberg, N.Bendsoe, U.Stenram, K.Svanberg, J.Spigulis, A.Derjabo and J.Kapostins, Photodynamic therapy of basal cell carcinoma with multi-fibre contact light delivery, *J. Env. Path. Tox. Onc.* **25**, (2005).

157. J.Regula, A.J.MacRobert, A.Gorchein, G.A.Buonaccorsi, S.M.Thorpe, G.M.Spencer, A.R.Hatfield and S.G.Bown, Photosensitisation and photodynamic therapy of oesophageal, duodenal and colorectal tumours using 5 aminolaevulinic acid induced protoporphyrin IX - a pilot study, *Gut* **36**, 67-75 (1995).

158. H.Heyerdahl, I.Wang, D.L.Liu, R.Berg, S.Andersson-Engels, Q.Peng, J.Moan, S.Svanberg and K.Svanberg, Pharmacokinetic studies on 5-aminolevulinic acid-induced protoporphyrin IX accumulation in tumours and normal tissues, *Cancer Lett.* **112**, 225-231 (1997).

159. S.Andersson-Engels, R.Berg, K.Svanberg and S.Svanberg, Multi-colour fluorescence imaging in combination with photodynamic therapy of δ-amino levulinic acid (ALA) sensitised skin malignancies, *Bioimaging* **3**, 134-143 (1995).

160. I.Wang, K.Svanberg, L.Pais Clemente, R.M.G.Pratas, E.Cardoso, M.Pais Clemente, S.Montán and S.Svanberg, Fluorescence diagnostics and kinetic studies in malignant and premalignant lesions and in normal tissue in the head and neck area utilising δ-amino levulinic acid sensitisation, *BIOS Europe'97, The European Biomedical Optics Week*, San Remo, Italy, (1997).

161. C.Eker, Optical characterization of tissue for medical diagnostics, Dissertation thesis, Lund Institute of Technology, Lund, Sweden (1999).

162. M.G.Muller, I.Georgakoudi, Q.Zhang, J.Wu and M.S.Feld, Intrinsic fluorescence spectroscopy in turbid media: disentangling effects of scattering and absorption, *Appl. Opt.* **40**, 4633-4646 (2001).

163. M.Soto Thompson, Photodynamic therapy utilizing interstitial light delivery combined with spectroscopic methods, Dissertation thesis, Lund Institute of Technology, Lund, Sweden, (2004).

164. T.J.Pfefer, K.T.Schomacker, M.N.Ediger and N.S.Nishioka, Multiple-fiber probe design for fluorescence spectroscopy in tissue, *Appl. Opt.* **41**, 4712-4721 (2002).

165. T.J.Pfefer, L.S.Matchette, A.M.Ross and M.N.Ediger, Selective detection of fluorophore layers in turbid media: the role of fiber-optic probe design, *Opt.Lett. 2***8**, 120-122 (2003).

166. T.J.Pfefer, K.T.Schomacker, M.N.Ediger and N.S.Nishioka, Light propagation in tissue during fluorescence spectroscopy with single-fiber probes, *IEEE Journal of Selected Topics in Quantum Electronics* **7**, 1004-1012 (2001).

167. N.Ramanujam, Fluorescence spectroscopy of neoplastic and non-neoplastic tissues, *Neoplasia* **2**, 89-117 (2000).

168. J.R.Mourant, I.J.Bigio, D.A.Jack, T.M.Johnson and H.D.Miller, Measuring absorption coefficients in small volumes of highly scattering media: source-detector separations for which path lengths do not depend on scattering properties, *Appl. Opt.* **36**, 5655-5661 (1997).

169. J.Svensson, Fluorescence spectroscopy in tissue for identification and temperature control of embedded lesions, Licentiate thesis, Lund Institute of Technology, (2005).

170. D.Y.Paithankar, A.U.Chen, B.W.Pogue, M.S.Patterson and E.M.Sevick-Muraca, Imaging of fluorescent yield and lifetime from multiply scattered light reemitted from random media, *Appl. Opt.* **36**, 2260-2272 (1997).

171. C.af Klinteberg, On the use of light for the characterization and treatment of malignant tumours, Dissertation thesis, Lund Institute of Technology, Lund, Sweden (1999).

172. H.Inaba, Coherent detection imaging for medical laser tomography, in *Medical optical tomography: functional imaging and monitoring,* ed. R.F.Potter, pp. 317-347 (SPIE institutes for advanced optical technologies, 1993).

173. A.W.Sainter, T.A.King and M.R.Dickinson, Effect of target biological tissue and choice of light source on penetration depth and resolution in optical coherence tomography, *J. Biomed. Opt.* **9**, 193-199 (2004).

174. J.Moan and Q.Peng, An outline of the hundred-year history of PDT, *Anticancer Res.* **23**, 3591-3600 (2003).

175. R.Ackroyd, C.Kelty, N.Brown and M.Reed, The history of photodetection and photodynamic therapy, *Photochem. Photobiol.* **74**, 656-669 (2001).

176. N.R.Finsen, *Phototherapy*, (Edward Arnold, London, 1901).

177. F.Urbach, P.D.Forbes, R.E.Davies and D.Berger, Cutaneous photobiology: past, present and future, *J. Invest. Dermatol.* **67**, 209-224 (1976).

178. O.Lingjærde, T.Reichborn-Kjennerud, A.Haggag, I.Gärtner, E.M.Berg and K.Narud, Treatment of winter depression in Norway. I. Short- and long-term effects of 1500-lux white light for 6 days, *Acta Psychiatr. Scand.* **88**, 292-299 (1993).

179. J.C.Kennedy, R.H.Pottier and D.C.Pross, Photodynamic therapy with endogenous protoporphyrin IX: Basic principles and present clinical experience, *J. Photochem. Photobiol. B.* **6**, 143-148 (1990).

180. T.J.Dougherty, B.W.Henderson, S.Schwartz, J.W.Winkelman and R.L.Lipson, Historical perspective, in *photodynamic therapy*, eds., pp. 1-15 (Marcel Dekker, New York, 1992).

181. M.D.Daniell and J.S.Hill, A history of photodynamic therapy, *Aust. N. Z. J. Surg.* **61**, 340-348 (1991).

182. J.Moan and K.Berg, The photodegradation of porphyrins in cells can be used to estimate the lifetime of singlet oxygen, *Photochem. Photobiol.* **53**, 549-553 (1991).

183. Q.Peng, K.Berg, J.Moan, M.Kongshaug and J.M.Nesland, 5-aminolevulinic acid-based photodynamic therapy: Principles and experimental research, *Photochem. Photobiol.* **65**, 235-251 (1997).

184. P.Juzenas, V.Iani, S.Bagdonas, R.Rotomskis and J.Moan, Fluorescence spectroscopy of normal mouse skin exposed to 5-aminolaevulinic acid and red light, *J. Photochem. Photobiol. B-Biology* **61**, 78-86 (2001).

185. R.L.Lipson, E.J.Baldes and A.M.Olsen, The use of a derivative of haematoporphyrin in tumour detection, *J. Natl. Cancer Inst.* **26**, 1-11 (1961).

186. R.L.Lipson, E.J.Baldes and M.J.Gray, Hematoporphyrin derivative for detection and management of cancer, *Cancer* **20**, 2255-2257 (1967).

187. M.El-Far, M.Ghoneim and E.Ibraheim, Biodistribution and selective *in vivo* tumor localization of endogenous porphyrins induced and stimulated by 5-amino-levulinic acid: A newly developed technique, *J. Tumor Mark. Onc.* **5**, 27-34 (1990).

188. J.Moan, J.T.H.M.van den Akker and P.Juzenas, On the basis for tumor selectivity in the 5-aminolevulinic acid-induced synthesis of protoporphyrin IX, *J. Porphyrins Phthalocyanines* **5**, 170-176 (2001).

189. P.Hinnen, F.W.M.de Rooij, M.L.F.van Velthuysen, A.Edixhoven, R.van Hillegersberg, H.W.Tilanus, J.H.P.Wilson and P.D.Siersema, Biochemical basis of 5-aminolaevulinic acid-induced protoporphyrin IX accumulation: a study in patients with (pre)malignant lesions of the oesophagus, *Br. J. Cancer* **78**, 679-682 (1998).

190. A.M.Wennberg, O.Larkö, P.Lönnroth, G.Larson and A.L.krogstad, Delta-aminolevulinic acid in superficial basal cell carcinomas and normal skin-a microdialysis and perfusion study, *Clin. Exp. Dermatol.* **25**, 317-322 (2000).

191. J.C.Kennedy and R.H.Pottier, Endogenous protoporphyrin IX, a clinically useful photosensitizer for photodynamic therapy, *J. Photochem. Photobiol. B.* **14**, 275-292 (1992).

192. Q.Peng, T.Warloe, K.Berg, J.Moan, M.Kongshaug, K.-E.Giercksky and J.M.Nesland, 5-aminolevulinic acid-based photodynamic therapy: Clinical research and future challenges, *Cancer* **79**, 2282-2308 (1997).

193. A.M.Wennberg, L.E.Lindholm, M.lpsten and O.Larkö, Treatment of superficial basal cell carcinomas using topically applied delta-aminolaevulinic acid and a filtered xenon lamp, *Arch. Dermatol. Res.* **288**, 561-564 (1996).

194. J.Moan, V.Iani and L.W.Ma, Choice of the proper wavelength for photochemotherapy, in Photochemotherapy: Photodynamic Therapy and Other Modalities, eds. B.Ehrenberg, G.Jori and J.Moan, Proc. SPIE vol. 2625, 544-549 (1996).

195. M.R.Thissen, M.W.de Blois, D.J.Robinson, H.S.de Bruijn, R.P.Dutrieux and W.M.Star, PpIX fluorescence kinetics and increased skin damage after intracutaneous injection of 5-aminolevulinic acid and repeated illumination, *J. Invest. Dermatol.* **118**, 239-245 (2002).

196. Z.Hua, S.L.Gibson, T.H.Foster and R.Hilf, Effectiveness of δ-aminolevulinic acid-induced protoporphyrin as a photosensitizer for photodynamic therapy in vivo, *Cancer Res.* **55**, 1723-1731 (1995).

197. D.J.Robinson, H.S.de Bruijn, N.van der Veen, M.R.Stringer, S.B.Brown and W.M.Star, Fluorescence photobleaching of ALA-induced protoporphyrin IX during photodynamic therapy of normal hairless mouse skin: The effect of light dose and irradiance and the resulting biological effect, *Photochem. Photobiol.* **67**, 140-149 (1998).

198. B.W.Pogue and T.Hasan, A theoretical study of light fractionation and dose-rate effects in photodynamic therapy, *Radiat. Res.* **147**, 551-559 (1997).

199. D.J.Robinson, H.S.de Bruijn, W.M.Star and H.J.C.M.Sterenborg, Dose and timing of the first light fraction in two-fold illumination schemes for topical ALA-mediated photodynamic therapy of hairless mouse skin, *Photochem. Photobiol.* **77**, 319-323 (2003).

200. T.Johansson, M.Soto Thompson, M.Stenberg, C.af Klinteberg, S.Andersson-Engels, S.Svanberg and K.Svanberg, Feasibility study of a novel system for combined light dosimetry and interstitial photodynamic treatment of massive tumors, *Appl. Opt.* **41**, 1462-1468 (2002).

201. M.Soto Thompson, A.Johansson, T.Johansson, S.Andersson-Engels, N.Bendsoe, K.Svanberg and S.Svanberg, Clinical system for interstitial photodynamic therapy with combined on-line dosimetry measurements, *Appl. Opt.* **44**, 4023-4031 (2005).

202. J.P.A.Marijnissen, J.A.C.Versteeg, W.M.Star and W.L.J.van Putten, Tumor and normal response to interstitial photodynamic therapy of the rat R-1 rhabdomyosarcoma, *Int. J. Radiat. Oncol. Biol. Phys.* **22**, 963-972 (1992).

203. S.F.Purkiss, R.Dean, J.T.Allardice, M.Grahn and N.S.Williams, An interstitial light delivery system for photodynamic therapy within the liver, *Lasers Med. Sci.* **8**, 253-257 (1993).

204. Q.Peng, T.Warloe, J.Moan, H.Heyerdahl, H.B.Steen, J.M.Nesland and K.-E.Giercksky, Distribution of 5-aminolevulinic acid-induced porphyrins in noduloulcerative basal cell carcinoma, *Photochem. Photobiol.* **62**, 906-913 (1995).

205. N.van der Veen, H.S.DeBruijn and W.M.Star, Photobleaching during and re-appearance after photodynamic therapy of topical ALA-induced fluorescence in UVB-treated mouse skin, *Int. J. Cancer* **72**, 110-118 (1997).

206. R.Rotomskis, S.Bagdonas and G.Streckyte, Spectroscopic studies of photobleaching and photoproproduct formation of porphyrins used in tumour therapy, *J. Photochem. Photobiol. B.* **33**, 61-67 (1996).

207. J.Moan, Effect of bleaching of porphyrin sensitizer during photodynamic therapy, *Cancer Lett.* **33**, 43-53 (1986).

208. V.Nadeau, M.O'Dwyer, Kh.HAmdan, I.Tait and M.Padgett, In vivo measurement of 5-aminolevulenic acid-induced protoporphyrin IX photobleaching: a comparision of red and blue light of various intensities, *Photodermatol. Photoimmunol. Photomed.* **20**, 170-174 (2004).

209. L.Kunz and A.J.MacRobert, Intracellular photobleaching of 5,10,15,20-tetrakis(m-hydroxyphenyl) chlorin (Foscan((R))) exhibits a complex dependence on oxygen level and fluence rate, *Photochem. Photobiol.* **75**, 28-35 (2002).

210. A.Uzdensky, A.Juzeniene, L.W.Ma and J.Moan, Photodynamic inhibition of enzymatic detachment of human cancer cells from a substratum, *Biochim. Biophys. Acta.* **1670**, 1-11 (2004).

211. Q.Chen, Z.Huang, H.Chen and H.Shapiro, Improvement of tumour response by manipulation of tumour oxygenation during PDT, *Photochem. Photobiol.* **76**, 197-203 (2002).

212. B.W.Henderson and V.H.Fingar, Oxygen limitation of direct tumor cell kill during photodynamic treatment of a murine tumor model, *Photochem. Photobiol.* **49**, 299-304 (1989).

213. T.M.Busch, S.M.Hahn, S.M.Evans and C.J.Koch, Depletion of tumor oxygenation during photodynamic therapy: Detection by the hypoxia marker EF3 [2-(2-Nitroimidazol-1[*H*]-yl)-*N*-(3,3,3-trifluoropropyl)acetamide], *Cancer Res.* **60**, 2636-2642 (2000).

214. B.J.Tromberg, A.Orenstein, S.Kimel, S.J.Barker, J.Hyatt, J.S.Nelson and M.W.Berns, In vivo tumor oxygen tension measurements for the evaluation of the efficiency of photodynamic therapy, *Photochem. Photobiol.* **52**, 375-385 (1990).

215. T.H.Foster, R.S.Murant, R.G.Bryant, R.S.Knox, S.L.Gibson and R.Hilf, Oxygen consumption and diffusion effects in photodynamic therapy, *Radiat. Res.* **126**, 296-303 (1991).

216. S.Coutier, L.N.Bezdetnaya, T.H.Foster, R.M.Parache and F.Guillemin, Effect of irradiation fluence rate on the efficacy of photodynamic therapy and tumor oxygenation in meta-tetra (hydroxyphenyl) chlorin (mTHPC)-sensitized HT29 Xenografts in nude mice, *Radiat. Res.* **158**, 339-345 (2002).

217. B.W.Henderson, S.O.Gollnick, J.W.Snyder, T.M.Busch, P.C.Kousis, R.T.Cheney and J.Morgan, Choice of oxygen-conserving treatment regimen determines the inflammatory response and outcome of hotodynamic therapy of tumors, *Cancer Res.* **64**, 2120-2126 (2004).

218. K.P.Nielsen, A.Juzeniene, P.Juzenas, K.Stamnes, J.J.Stamnes and J.Moan, Choice of optimal wavelength for PDT: The significance of oxygen depletion, *Photobiochem. Photobiophys.* (2005).

219. P.Uehlinger, M.Zellweger, G.Wagnieres, L.Juillerat-Jeanneret, H.van den Bergh and N.Lange, 5-Aminolevulinic acid and its derivatives: physical chemical properties and protoporphyrin IX formation in cultured cells, *J. Photochem. Photobiol. B.* **54**, 72-80 (2000).

220. C.Fuchs, R.Riesenberg, J.Siegert and R.Baumgartner, pH-Dependent formation of 5-aminolaevulinic acid-induced protoporphyrin IX in fibrosarcoma cells, *Photochem. Photobiol.* **40**, 49-54 (1997).

221. E.G.Friberg, B.Cunderlikova, E.O.Pettersen and J.Moan, pH effects on the cellular uptake of four photosensitizing drugs evaluated for use in photodynamic therapy of cancer, *Cancer Lett.* **195**, 73-80 (2003).

222. J.W.Pickering, S.Bosman, P.Posthumus, P.Blokland, J.F.Beek and M.J.C.van Gemert, Changes in the optical properties (at 632.8 nm) of slowly heated myocardium, *Appl. Opt.* **32**, 367-371 (1993).

223. W.M.Star, B.C.Wilson and M.S.Patterson, Light delivery and optical dosimetry in photodynamic therapy of solid tumors, in *photodynamic therapy,* ed. B.W.Henderson, pp. 335-367 (New York; Basel; Hong Kong, 1992).

224. L.O.Svaasand, Photodynamic and photohyperthermic response of malignant tumors, *Med. Phys.* **12**, 455-461 (1985).

225. P.Juzenas, R.Sorensen, V.Iani and J.Moan, Uptake of topically applied 5-aminolevulinic acid and production of protoporphyrin IX in normal mouse skin: Dependence on skin temperature, *Photobiochem. Photobiol.* **69**, 478-481 (1999).

226. A.Juzeniene, P.Juzenas, O.Kaalhus, V.Iani and J.Moan, Temperature effect on accumulation of protoporphyrin IX after topical application of 5-aminolevulinic acid and its methylester and hexylester derivatives in normal mouse skin, *Photochem. Photobiol.* **76**, 452-456 (2002).

227. J.Moan, K.Berg, Ö.B.Gadmar, V.Iani, L.Ma and P.Juzenas, The temperature dependence of protoporphyrin ix production in cells and tissues, *Photochem. Photobiol.* **70**, 669-673 (1999).

228. A.M.K.Nilsson, R.Berg and S.Andersson-Engels, Measurements of the optical properties of tissue in conjunction with photodynamic therapy, *Appl. Opt.* **34**, 4609-4619 (1995).

229. J.P.A.Marijnissen and W.M.Star, Quantitative light dosimetry in vitro and in vivo, *Lasers Med. Sci.* **2**, 235-242 (1987).

230. M.Soumaya and T.H.Foster, Carbogen breathing significantly enhances the penetration of red light in murine tumours *in vivo*, *Phys. Med. Biol.* **49**, 1891-1904 (2004).

231. A.Johansson, T.Johansson, M.Soto Thompson, N.Bendsoe, K.Svanberg, S.Svanberg and S.Andersson-Engels, In vivo measurement of parameters of dosimetric importance during photodynamic therapy of thick skin tumors, *J. Biomed. Opt*, In Press, (2006).

232. M.C.G.Aalders, N.van der Vange, W.M.Star and H.J.C.M.Sterenborg, A mathematical evaluation of dose-dependent PpIX fluorescence kinetics in vivo, *Photochem. Photobiol.* **74**, 311-317 (2001).

233. L.O.Svaasand, B.J.Tromberg, P.Wyss, M.-T.Wyss-Desserich, Y.Tadir and M.W.Berns, Light and drug distribution with topically administered photosensitizers, *Lasers Med. Sci.* **11**, 261-265 (1996).

234. K.Moser, K.Kriwet, A.Naik, Y.N.Kalia and R.H.Guy, Passive skin penetration enhancement and its quantification in vitro, *European Journal of Pharmaceutics and Biopharmaceutics* **52**, 103-112 (2001).

235. R.J.Scheuplein and I.H.Blank, Permeability of the skin, *Physiological Reviews* **51**, 702-747 (1971).

236. R.O.Potts and M.L.Fragncoeur, The influence of stratum corneum morphology on water permeability, *J. Invest. Dermatol.* **96**, 495-499 (1991).

237. R.O.Potts and R.H.Guy, Predicting skin permeability, *Pharm. Res.* **9**, 663-669 (1992).

238. L.O.Svaasand, P.Wyss, M.T.Wyss, Y.Tadir, B.J.Tromberg and M.W.Berns, Dosimetry model for photodynamic therapy with topically administered photosensitizers, *Lasers Surg. Med.* **18**, 139-149 (1996).

239. R.Fonseca, V.Lopez, N.Lange, R.Guy, M.V.Lopes and B.Bentley, Photodynamic therapy of skin cancer: controlled drug delivery of 5-ALA and its esters, *Advanced Drug Delivery Reviews.* **56**, 77-94 (2004).

240. J.T.H.M.van den Akker, V.Iani, W.M.Star, H.J.C.M.Sterenborg and J.Moan, Topical application of 5-aminolevulinic acid hexyl ester and 5-aminolevulinic acid to normal nude mouse skin: Differences in protoporphyrin IX fluorescence kinetics and the role of the stratum corneum, *Photochem. Photobiol.* **72**, 681-689 (2000).

241. B.A.Goff, R.Bachor, N.Kollias and T.Hasan, Effects of photodynamic therapy with topical application of 5-aminolevulinic acid on normal skin of hairless guinea pigs, *J. Photochem. Photobiol. B.* **15**, 239-251 (1992).

242. A.Juzeniene, L.W.Ma, P.Juzenas, V.Iani, N.Lange and J.Moan, Production of protoporphyrin IX from 5-aminolevulenic acid and two of its esters in cells in vitro and tissues invivo, *Cell Mol. Biol.* **48**, 911-916 (2002).

243. J.Moan, L.W.Ma and V.Iani, On the pharmacokinetics of topically applied 5-aminolevulinic acid and two of its esters, *Int. J. Cancer* **92**, 139-143 (2001).

244. Q.Peng, T.Warloe, J.Moan, H.Heyerdahl, H.Steen, K.-E.Giercksky and J.M.Nesland, ALA derivative-induced protoporphyrin IX build-up and distribution in human nodular basal cell carcinoma, *Photochem. Photobiol.* **61**, 82S (1995).

245. J.-M.Gaullier, K.Berg, Q.Peng, H.Anholt, P.K.Selbo, L.W.Ma and J.Moan, Use of 5-aminolevulinic acid esters to improve photodynamic therapy on cells in culture, *Cancer Res.* **57**, 1481-1486 (1997).

246. De Rosa FS, Lopez RF, Thomazine JA, Tedesco AC, Lange N and Bentley MV., In vitro metabolism of 5-ALA esters derivatives in hairless mice skin homogenate and in vivo PpIX accumulation studies., *Pharm. Res.* **21**, 2247-2252 (2004).